A Label-Free Biosensor for Heat Shock Protein 70 Using Localized Surface Plasmon Resonance

by

Ryan Denomme

A thesis
presented to the University of Waterloo
in fulfillment of the
thesis requirement for the degree of
Master of Applied Science
in
Mechanical Engineering

Waterloo, Ontario, Canada, 2012

©Ryan Denomme 2012

AUTHOR'S DECLARATION

I hereby declare that I am the sole author of this thesis. This is a true copy of the thesis, including any required final revisions, as accepted by my examiners.

I understand that my thesis may be made electronically available to the public.

Abstract

Heat shock protein 70 (HSP70) is an important health related biomarker. For example, HSP70 has been implicated as a potential early stage cancer marker and as an indicator of cardiac health. It also has important implications in wildlife environmental monitoring, as its levels can be affected by food deprivation, elevated temperatures, and pollution. Although the use of HSP70 as a biomarker in these applications is highly desirable, the current methods of quantifying HSP70 are time consuming, expensive, and require dedicated labs and trained personnel. In order to facilitate widespread use of HSP70 as a health/environmental marker, a quantification tool that can be used at the point-of-care is needed. This implies the development of an easy to use and inexpensive biosensing technique that is highly sensitive and selective to enable detection of HSP70 in the low ng/ml range from serum samples. Therefore, in this work a label-free HSP70 biosensor has been designed that is based on the optical properties of metal nanoparticles (NPs). Metal NPs exhibit a large absorbance peak in the visible spectrum due to a phenomenon known as localized surface plasmon resonance (LSPR). The position of this peak is highly dependent on the local refractive index, which can be employed as a biosensor by selectively capturing the target analyte to the surface of the nanoparticle through a target-specific antibody. To design an LSPR HSP70 sensor, optical and fluidic simulations were developed to determine optimal nanoparticle geometries and optimal microfluidic channel dimensions. The results showed optimal response when using 100nmx5nm gold nanotriangles in a 100μmx100μm sensor array inside of a 100μmx100μm microchannel. Simulations of the sensor performance showed that HSP70 could be detected from 0.92ng/ml to 4000ng/ml with a low end sensitivity of 0.014nm/ng/ml and a resolution of 1.1ng/ml, all of which satisfied the design requirements. An LSPR sensor was experimentally tested at the benchtop scale to prove the concept. Gold nanoparticles were fabricated by electron beam lithography on glass substrates and enclosed in a polymer flow cell. For initial testing of the LSPR sensor, the NPs were functionalized with biotin for selective capture of the model protein streptavidin. Streptavidin was detected in real time using a transmission UV-Vis spectroscopy system over the range 55-500,000ng/ml, resulting in peak shifts from 0.07-5.53nm and an equilibrium binding constant of $9.22*10^{6}$ M^{-1}. The use of bovine serum albumin (BSA) was shown to be necessary to block non-specific binding sites to ensure a streptavidin-specific response. The LSPR sensor was then demonstrated to detect salmon HSP70 using its synthetic antibody. Exposing the sensor to purified HSP70 at a concentration of 4.6μg/ml resulted in an LSPR peak shift of 0.39nm +/-0.12nm.

Acknowledgements

Firstly, I would like to acknowledge my supervisor, Professor Patricia Nieva, for giving me the opportunity to work on this project. Thank you for all of the support you have given me.

I would also like to thank Professor Matt Vijayan, a collaborator on this project from the Biology Department, for providing much needed guidance and assistance in this field. Thank you for continuing to support my efforts in this research area. Also from Professor Vijayan's lab I would like to thank Erin Faught and Nita Modi for all of their help throughout this project.

Thanks to the previous lab managers of the SIMSLab, Jeff McIsaac, Sooky Winkler, and Gabriel Krausz, who have supported me in many different ways over the time they spent with our lab. I especially would like to thank all of the co-op undergraduate students who have worked on this project with me over the last two years: Nathan Dyck, Jacky Chan, Krishna Iyer, Brendan Smith, Michael Kreder, Zachary Young, Urvashi Pal, Chelsea Marr, Lindsay Brock, Matthew Mulvale, Matthew Dozois, and Laura Edmonds. Your hard work and exceptional talent helped make this research possible. I would also like to thank Sasan Asiaei for helpful discussions and input.

I would like to thank my parents, Steve and Tanis, and my partner, Katie Schafer, who have always encouraged me to work hard and to achieve my dreams. Your continuous support has been invaluable to my success.

Table of Contents

List of Figures

List of Tables

Chapter 1
Introduction: Motivation and Scope

Heat shock protein 70 (HSP70) is an important stress related biomarker that is gaining a large amount of attention in both human and wildlife diagnostic monitoring applications. In general, HSP70 is a protein that is produced at much higher levels in response to external stress stimuli. In human health diagnostics, there has been much attention around using the HSP family as biomarkers to help the diagnosis and treatment of various diseases and conditions. Specifically, elevated levels of HSPs have been found to be associated with over 200 different types of cancer, including breast, endometrial, ovarian, oral, gastric, liver, pancreatic, lung, and many more [**1**]. This indicates the potential for HSPs to be used as early cancer markers for improved diagnosis and prognosis. In fact, this has already been suggested for a variety of cancers, such as prostate cancer diagnosis using HSP70 serum levels [**2**]. HSP70 over-expression has also been implicated in metastasis and resistance to chemotherapy or radiation in brain [**3**] and breast [**4**] cancer. This means HSP70 could be used to personalize medicine by predicting treatment outcomes on a patient by patient basis and making the necessary adjustments to maximize the effectiveness of the treatment. In addition, HSP70 has been heavily implicated as an indicator of cardiac health, with elevated levels discovered in the hearts of patients with unstable angina [**5**], a known risk factor for myocardial infarction (heart attack) [**6**], and dilated cardiomyopathy [**7**], which is linked to congestive heart failure.

HSP70 has also been implicated as an important wildlife biomarker for environmental health monitoring. HSP70 levels have shown to be elevated due to increased environmental temperatures [**8**], dehydration [**9**], food deprivation [**10**], osmotic stress [**11**], oxygen starvation [**12**], and pollution [**13**], such as heavy metals [**14**], [**15**]. Therefore, monitoring HSP70 levels in wildlife can be used as an early warning signal of deleterious effects, and as a means for estimating biological effects caused by adverse environmental conditions such as pollution or habitat destruction [**16**]. Examples include monitoring HSP70 levels in marine organisms in the Antarctic [**17**] and in grizzly bears in Alberta [**18**].

Although HSP70 has gained much attention as an important new biomarker, methods used to quantify and detect HSP70 are not adept for widespread diagnostic applications. The only available methods to quantify HSP70, which include enzyme-linked immunosorbent assay (ELISA) and western blot, require samples to be transported back to labs in which dedicated equipment, reagents, and personnel are needed. This is extremely time consuming, costly, and laborious. Therefore, the development of a portable diagnostic device that is capable of rapidly quantifying HSP70 levels outside of the laboratory is proposed

and is the focus of this research. Such a device would facilitate the widespread and routine use of HSP70 in many monitoring applications in humans and wildlife. This field of study is typically known as point-of-care (POC) diagnostics, as the diagnostic tests are brought outside of centralized labs to the point where they are needed. POC diagnostics provide essential information faster, with more convenience, and with less cost than centralized labs. Such improvements are required in healthcare due to growing costs and long wait times, and in wild life monitoring as the environment is rapidly changing.

Many biosensing techniques exist with the potential for being used in a field portable HSP70 diagnostic device, including mechanical, electrical, and optical techniques. Among these, optical techniques are well suited for POC use as they are very robust yet low cost. Additionally, label-free techniques are the most simple and cost effective, making label-free optical sensing methods the most attractive for this device. Therefore, in this research an HSP70 sensor has been developed using a label-free optical technique known as localized surface plasmon resonance (LSPR). LSPR is similar to the well-established technique of SPR, except it uses an array of metal nanoparticles rather than a continuous film of metal. This makes LSPR more amiable to integration into a portable format due to simpler optical hardware requirements.

In this thesis, a label-free LSPR sensor for HSP70 is designed and experimentally tested. The focus of the research is on designing an HSP70 sensor for environmental wildlife monitoring, although the results are widely applicable to the medical diagnostics field. In Chapter 2, an introduction to biosensors is given, followed by a review of current HSP70 detection techniques. The requirements of the label-free HSP70 sensor are outlined, and an analysis of LSPR sensing is given to justify its choice. The theoretical background and sensing mechanism of LSPR is discussed and a brief literature review of previous research on LSPR biosensors is given. In Chapter 3, an overview of the sensor design is given, followed by comprehensive optical and fluidic simulations. These simulations are used to design optimal nanoparticle geometries and microfluidic structures to ensure the sensor can meet the stated requirements. In Chapter 4, a benchtop prototype sensor is developed in order to prove the concept and develop the sensing protocols. Gold nanoparticles are fabricated and characterized, and a surface functionalization protocol developed based on alkanethiol self-assembled monolayers to allow specific capture of target proteins to the sensor surface. The LSPR sensor is characterized using biotin as an antibody to detect the protein streptavidin, a model biological system used often for such characterization purposes. The dynamic range, limit of detection, and specificity of the sensor are evaluated using this model system. Finally, HSP70 detection using the LSPR system is demonstrated using a synthetic salmon HSP70 antibody as the capture probe.

Chapter 2
Technical Background

In this chapter, an overview of the main principles, implementations, and design aspects of biosensors is given. Then, a review of the current methods of sensing HSP70 is presented, followed by an outline of the specifications required for a label-free HSP70 biosensor. Next, an overview of the theory behind LSPR sensors is given along with a review of recent literature on the topic. This review is compared to the required specifications of the HSP70 sensor, and justification for the choice of LSPR is given.

2.1 Biosensor Principles: Label vs. Label-Free

A biosensor is a device that is used to detect and/or quantify a biochemical molecule, such as a protein or strand of DNA. Every biosensor is made of three basic components, illustrated in Figure 1 below: the biointerface, the transducing mechanism, and the output system [**19**]. The biointerface is the manner in which the target analyte (the molecule being detected) is selectively bound to the surface of the sensor, usually using an intermediate molecule known as a capture probe or receptor ligand. The biointerface determines the selectivity of the sensor. The transducing mechanism is the way in which a binding event is translated into a readable change in signal, and plays a critical role in the sensitivity. Typically, transducer mechanisms are categorized as electrical, mechanical, or optical. The output system comprises all post-processing that must be done to the raw data provided by the transducer, including amplifying, filtering, reading, and transmitting. All three aspects of the biosensor together have significant effects on the performance of the sensor [**20**], [**21**].

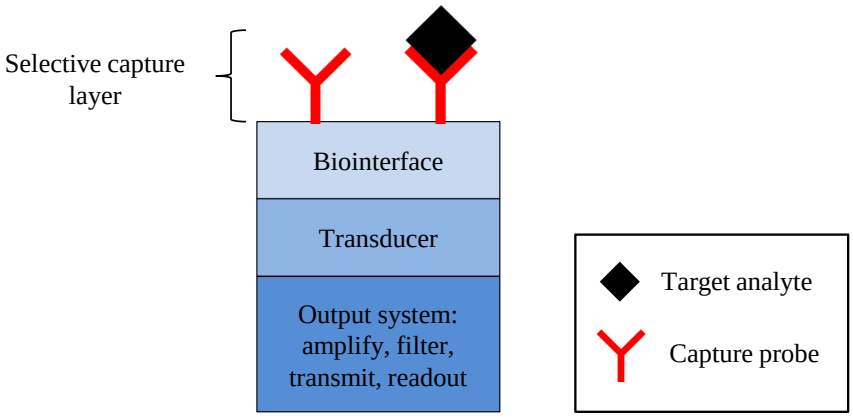

Figure 1. Illustration showing the three main components of a biosensor. These components include the biointerface, used for selectively capturing the target analyte, the transducer, which translates the binding event in a readable signal, and the output system.

Biosensors can be divided into two broad categories: labeled and label-free. Both techniques are illustrated below in Figure 2. In labeled techniques, after the analyte binds to the capture probe, a label molecule is selectively bound to the analyte [**21**]. The transducing mechanism measures the amount of label bound, which is assumed to be the same as the amount of analyte. The label can be a fluorescent dye, a magnetic bead, a metal nanoparticle, or a radioactive molecule, and is often done using a sandwich assay. The label offers a way to easily measure the analyte through simple transducing mechanisms such as a fluorescence reading. This is needed because detecting biological analytes directly through their physical properties, such as mass, has traditionally been difficult [**22**]. Thus, labeled techniques are the most common and are used in standard biological detection processes such as western blot and ELISA.

The main drawbacks of labeled techniques include unstable, dangerous and costly label molecules, a large number of processing steps, equipment, and reagents, modification of the analyte upon labeling, and large variation in the yield of the labeling reaction [**21**]. In fluorescent techniques, only end point detection can be used due to photobleaching, so kinetic information is unavailable [**22**]. Labeled assays typically require significant process development to assure the label has minimal effect on the analyte [**22**]. Due to the numerous issues associated with labeled technique, label-free techniques have been developed. In label-free techniques, the binding of the analyte to the probe is measured directly by the transducing mechanism. The transducer converts a physical property of the analyte, such as mass, into a quantifiable signal. Label-free biosensors, along with being lower cost and less complex, have the further advantage of measuring binding in real time, which allows determination of binding kinetics. However, achieving the same levels of specificity and sensitivity as with labeled techniques is often challenging [**21**].

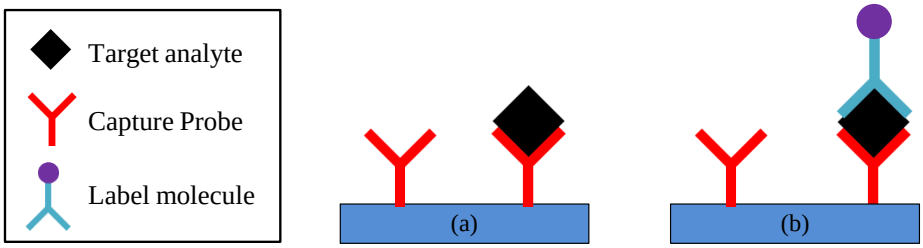

Figure 2. Illustration showing (a) label-free and (b) labeled biosensor implementations.

For the development of portable sensors, the most important characteristics are typically cost, speed, and instrument size, while extreme sensitivity and accuracy are not as critical [**21**]. Therefore, the simplicity and lower cost of the label-free techniques make them the better choice for the development of portable sensing technology, which is why a label-free sensing technology was investigated for this application.

2.2 Biosensor Transducer Mechanisms

The transducer mechanism is the way in which the binding of a target biomolecule is transformed into a readable output response. There are a number of methods that have been used to detect binding events of biomolecules, and this will not be reviewed in detail here. Detailed reviews of recent biosensing transduction technologies can be found in [**23**], [**24**], [**25**], [**26**], [**27**], [**28**], [**29**], [**30**]. Briefly, these different methods can be categorized broadly as mechanical, electrical, and optical. Mechanical methods include devices such as micromachined cantilevers, in which bound biomolecules cause a change in surface stress or mass, both of which alter the deflection or resonance position of the cantilever. Electrical methods use microfabricated electrodes to detect biomolecule binding via changes in the electrical response (impedance, potential, conduction). In optical techniques, protein binding causes a change in the optical properties of an interface, such as the refractive index, which is measured using surface plasmon resonance, ring resonators, interferometry, and other methods.

Although all types of transducing mechanisms have potential, optical techniques are one of the most popular [**19**], [**30**], [**31**], [**32**] for biosensing, especially in label-free applications. For instance, electrical techniques usually require electroactive enzyme labels, and background interference is often an issue [**30**], [**33**]. They are also heavily influenced by temperature, pH and ionic concentrations, tend to degrade more rapidly, and are not inherently compatible with aqueous solutions [**33**]. Mechanical/acoustic techniques are prone to vibrational noise and often require exotic materials that are difficult or expensive to work with [**30**]. They are also less sensitive compared to optical techniques, in part due to liquid damping effects [**30**]. Optical techniques have a per-test cost advantage over electrical techniques, and optical detection is easier to realize in a multiplexed format [**33**]. Also, optical components and hardware are rapidly reducing in cost and size, making them more practical for portable diagnostics [**33**]. They are also more compatible with aqueous solutions, are non-destructive, robust against noise, can be used for real-time analysis, and have less interference from bulk solutions [**30**]. Due to the numerous advantages of optical techniques, they are an attractive method for portable biosensing applications.

2.3 Biointerfaces

The biointerface is the manner in which the target biomolecule is selectively bound to the surface of the transducer, typically through a capture probe. It determines the selectivity of the sensor. The requirements for the biointerface are [**34**]:

1) High surface density of functional molecules

2) Absence of non-specific binding
3) Stability and durability

For label-free detection, the capture probe is usually an antibody that binds to the target biomolecule with high specificity. The antibody can be attached to the surface through numerous coupling chemistries, such as amine and thiol, and using various surface coatings, such as carboxylic thiol self-assembled monolayers, dendrimers, and polymers. Excellent resources detailing such techniques can be found in [**22**], [**35**], and [**36**].

2.4 Biosensor Performance Considerations

In this section, the main aspects of biosensor design will be reviewed, with specific focus on how they influence the performance of the device.

2.4.1 Analyte-Probe Binding

The binding of an analyte (A) to a capture probe (B) to form a complex (AB) can be described by the Langmuir adsorption isotherm (assuming a 1:1 interaction), which is the basic transfer function for many biosensors [**21**], [**22**]:

$$\theta = \frac{R}{R_{max}} = \frac{[AB]}{[B] + [AB]} = \frac{[A]}{K_D + [A]} \quad (1)$$

In which θ is the fraction of analyte bound to the probe, R is the response of the sensor after formation of the complex AB, R_{max} is the response when all of the capture probe sites are occupied, and K_d is the equilibrium dissociation constant. K_d is the concentration of [A] which gives $0.5R_{max}$, and is given by [**22**]:

$$K_d = \frac{[A][B]}{[AB]} = \frac{k_d}{k_a} = \frac{1}{K_a} \quad (2)$$

The association rate constant, k_a, is the rate at which the complex forms and the dissociation rate constant, k_d, is the rate at which the complex falls apart. These are known as kinetic constants while K_d is an affinity constant. K_a is known as the association constant and is simply the reciprocal of K_d. By generating a plot of R (at equilibrium) versus [A] and fitting to an isotherm, R_{max} and K_d can be found. k_a and k_d can be found through fitting models to real time data for the association and dissociation steps of the reaction. The affinity of the probe for the analyte significantly affects sensor performance: higher affinities will result in lower detection limits and faster detection times, with less background interference.

2.4.2 Sensitivity and Resolution

The sensitivity of a biosensor is defined as the output response of the sensor resulting from a unit change in the mass density on the sensor surface [**22**]. The mass density is proportional to the property being measured, such as refractive index or permittivity, and is usually reported in mass/area. The sensitivity depends fundamentally on the efficiency of the transducing technique and not on the affinity between the analyte and the capture probe. Therefore, it is also independent of the analyte being measured. Devices with higher sensitivities result in lower detection limits and better resolution.

The assay sensitivity is defined as the output response of the sensor per unit of analyte exposed to the sensor [**22**]. It is usually defined in terms of analyte concentration in the sample, such as moles/volume or mass/volume of the analyte. Assay sensitivity depends on other factors besides the efficiency of the transducer, including the affinity of the analyte-probe system, buffer conditions, temperature, and molecular weight of the analyte. The transfer function of the sensor defines the output of the sensor for a unit input. Resolution is the smallest change that can be measured given the noise level in the system and the sensitivity.

2.4.3 Limit of Detection, Reproducibility, and Accuracy

The limit of detection (LOD) is the minimum change in mass density or analyte concentration that can be measured [**22**]. The LOD depends on the noise associated with the entire sensor system and the sensitivity. The noise is typically quantified by allowing the sensor to reach a steady state and measuring the standard deviation, σ, of the signal over a period of time. Typically, the minimal detectable signal is defined as 3σ, which means LOD = 3σ/sensitivity. A smaller LOD is usually preferred in order to detect analytes at the low concentrations typically found in the blood.

Reproducibility refers to the variation between tests on a sensor, or the precision of the test. It is often a problem because running a calibration step for each sensor or each time the sensor is used is not practical. A lack of reproducibility often affects the practical detection limits achievable [**21**]. Accuracy typically refers to how well the results of the biosensor compare to a standard laboratory test.

2.4.4 Selectivity

Selectivity refers to the degree to which the sensor responds only to the target analyte and not to other similar analytes that may be present in the sample. This is often an issue in protein sensors because of the high concentration of background protein in the blood compared to the low concentration of the target protein. Blood serum can contain up to 70mg/ml of total protein content, while many biomarkers of

interest are in the ng/ml range [**21**]. Therefore, the capture probe needs to be extremely selective, or additional sample preparation steps to filter out background protein are needed.

Nonspecific binding is another issue related to selectivity, and it occurs when non-target molecules bind to the sensor surface and cause a signal change. To prevent this, blocking of the empty sites on the sensor surface is done with a molecule which does not interact with the capture probe or analyte. Typically, bovine serum albumin (BSA) is used. A differential sensor setup can be also used to subtract out this effect [**21**].

A final related issue is binding of the target analyte to the area surrounding the sensor, such as flows cells and microchannels [**21**]. This causes the bulk analyte concentration to decrease, causing the sensor to give erroneous results. This can be avoided through the use of antifouling agents or selection of low protein binding materials.

2.4.5 Dynamic Range

Dynamic range refers to the range of analyte concentrations over which the sensor can detect, which is bounded on the lower limit by the LOD and on the upper limit by the saturation concentration of the analyte to the probe. It is important to consider when sensors are used for quantitative determination of the analyte rather than just detecting its presence [**21**].

2.4.6 Cost, Size, Time, and Ease of Use

Cost, size, and ease of use are all important aspects impacting the commercial success of biosensors. The cost depends on the cost of the consumables and the detection instrumentation. The cost of consumables, such as the sensor chip, can be reduced through regeneration and reuse, and through mass production [**22**]. The cost of the instrumentation depends on the complexity required, such as a laser vs. light emitted diode for a light source. The size of the instrument is also dependent on the complexity – for most field applications, it needs to be portable, which would limit its size and weight and hence complexity.

Ease of use means that the test should be simple to perform, which ultimately means the user needs no technical or specialized training [**37**]. It also means that the sensor should be able to operate in a variety of conditions, such as fluctuating temperatures/humidity, unreliable power and water supplies, vibrational and electromagnetic noise, and others [**37**].

The time that is required for a test is usually defined as the time from which the sample is taken to the time at which the results are produced, the “bleed to read” time. This defines the number of samples that

can be processed per hour [**22**]. Ideally this time is as small as possible, but the requirements are highly dependent on the application. For example, for detection of myocardial infarction, the ideal bleed to read time is less than 30 minutes [**38**].

2.5 Current Label-Free HSP70 Biosensing Technology

The main method of HSP70 detection and quantification is ELISA and western blot [**39**], both of which are labeled techniques. Referring to the discussion in Section 2.1, labeled techniques are generally not suitable for portable biosensors. The following will review current HSP70 sensing techniques that have been demonstrated as label-free platforms, of which there have only been two examples.

2.5.1 Quartz Crystal Microbalance

A quartz crystal microbalance (QCM) sensor for HSP70 detection from mussels was one of the first label-free HSP70 sensors reported [**39**]. Two different surface functionalization protocols were used for capturing HSP70: one which used monoclonal HSP70 and one which used heptapeptides. Detection of HSP70 was shown from 10-100µg/ml. The sensor was able to be regenerated up to 10 times using a glycine-HCl buffer solution, with 20%-28% repeatability. Non-specific binding was tested with BSA and rabbit immunoglobulin G (IgG) and shown to be low. HSP70 detection from a crude extract from stressed Mussels was also demonstrated, demonstrating the high specify of the sensor.

2.5.2 Surface Plasmon Resonance

A surface plasmon resonance (SPR) HSP70 sensor was demonstrated using wavelength modulation [**40**]. Rabbit anti-HSP70 was used as the capture probe and immobilized on a gold surface using 3-mercaptopropionic acid (MPA) and carbodiimide hydrochloride (EDC)/N-hydroxysuccinimide (NHS) coupling. Detection of HSP70 was shown from 0.1-10µg/ml. The sensor was regenerated using citrate buffer. The equilibrium association binding constant of the system was determined to be 1.50×10^{7}-7.71×10^{7} M^{-1}. The sensor was blocked with BSA to lower nonspecific binding.

SPR was also used to investigate the binding kinetics between HSP70 and cytoplasmic proteins [**41**]. An amine coupling method was used to immobilize HSP70 on dextran coated gold surfaces of CM5 Biacore SPR chips using EDC/NHS chemistry. However, this system was not used to detect HSP70; it was used to investigate the kinetic relationship between HSP70 and different peptides.

2.6 HSP70 Biosensor Requirements and Analysis of Current Technology

In order to evaluate whether the current label-free HSP70 sensors are adequate for label-free sensing of HSP70 in a portable environment, a list of performance specifications was developed and is presented in Table 1. Some of these specifications are estimates from previous studies done on HSP70 levels in grizzly bears, as that is one application being investigated. However, others have been taken from applications in POC diagnostics in health care, in which the requirements are similar.

Table 1. Specification list for label-free HSP70 biosensor for point-of-care.

Specification	Value
Limit of detection	1ng/ml [**18**]
Resolution	1ng/ml [**18**]
Accuracy	90% [**37**]
Dynamic range	1ng/ml – 50ng/ml [**18**]
Reproducibility	+/- 10% [**18**]
Selectivity	Very high (for detection directly in serum) [**18**]
Sample volume	<100µl [**31**]
Detection time	30-60 minutes [**37**]
Cost	<$10,000/instrument (estimate), <$5/test [**37**]
Size	Portable (laptop size) [**37**]
Ease of use	No technical training needed (self-contained) [**42**]
Environmental conditions	4 to 25+°C, rough handling [**42**]
Multiplexing	Not required at this stage [**18**]
Shelf life	1 year [**37**]

Comparing the current label-free technologies demonstrated for HSP70 to this list of requirements reveals several significant problems. For the QCM device, the LOD is extremely far off from the levels required. QCM is also very sensitive to environmental effects, such as temperature changes, electrical noise, pressure changes, and mechanical disturbances [**43**], and so it is in general not a technique that is applicable in a field device. The SPR device demonstrates a detection limit (100ng/ml) approaching the LOD requirement, and could likely be optimized to reach it. SPR is an optical technique, so it is robust against most sources of noise, but it is extremely temperature sensitive [**44**]. Although this can be compensated for, it leads to increased cost and complexity. Also, the optical requirements of SPR devices are fairly complicated, and so making a portable device is challenging and costly [**19**], [**45**], [**46**]. From

this analysis, it is clear that there is currently no biosensing technology that is capable satisfying these requirements for HSP70 measurement in the field. Therefore, in this work a new biosensing technology for HSP70 is proposed to meet these requirements, which is based on LSPR.

2.7 Localized Surface Plasmon Resonance Sensing

LSPR is a new biosensing technique with the potential to be a highly sensitive, robust, field portable protein sensing device. LSPR is a nanoscale optical phenomenon that is exhibited by noble metal nanoparticles, such as gold, silver, aluminum, and copper [**47**]. LSPR results in sharp optical absorbance peaks, usually in or near the visible spectrum. To exhibit LSPR, the nanoparticles must have a negative real and small positive imaginary dielectric constant, and be geometrically smaller than the wavelength of light used to probe them (typically $R/\lambda<0.1$ [**45**]) [**48**]. The position of the LSPR peak is highly dependent on the nanoparticles size, shape, composition, orientation, and local dielectric environment [**48**]. It is this sensitivity to the local dielectric environment that allows the LSPR phenomenon to be used for a variety of sensing purposes. It is typically used as a local refractive index sensor by monitoring changes in the position of the resonance peak. LSPR has been used in label-free biological sensors for antibody-antigen immunoassays [**49**], [**50**], [**51**], [**52**], [**53**], [**54**], [**55**], [**56**], [**57**] and DNA analysis [**58**], [**59**], [**60**], [**61**], and chemical sensors for vapors [**62**], [**63**], [**64**], small molecules [**65**], and elements [**66**]. It has also been used for humidity [**67**], temperature [**68**], and pH sensing [**69**].

For biosensing, LSPR is similar to conventional SPR, but has some significant advantages specifically for portable devices [**46**], [**70**] which will be discussed subsequently. It has been gaining more attention recently with the improvements made in the field of nanofabrication.

2.7.1 Theoretical Background of LSPR

A surface plasmon, also known as a surface plasmon polariton, is a collective oscillation of the free surface electrons of noble metals which occupy the conduction bands [**46**]. It is created by the presence of an external oscillating electromagnetic (EM) field. When the surface plasmon is confined to a nanoparticle, a localized surface plasmon (LSP) is produced, as shown in Figure 3. The LSP exhibits electric field enhancement near the particles surface, which rapidly decays with distance from the particle. The LSP also exhibits an extinction (scattering plus absorbance) maximum at the resonance frequency, which is in the visible for most noble metals, and is termed the LSPR. This resonance peak is not seen in the bulk metal.

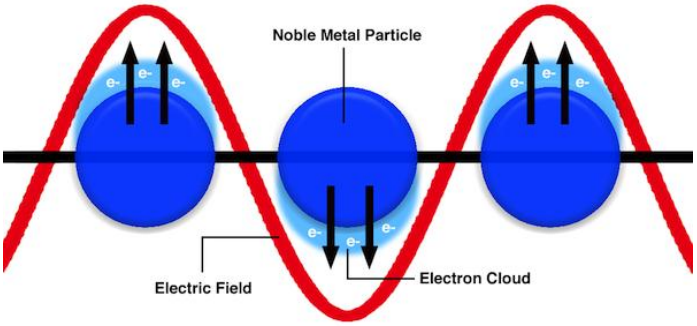

Figure 3. Illustration showing the formation of a surface plasmon on metal nanoparticles. Incoming electromagnetic waves cause a local oscillation of the nanoparticle's free surface electrons, resulting in a large absorbance peak at the resonance frequency.

The extinction of metal nanoparticles can be studied using Mie theory, which is an analytical solution to Maxwell's equations that describes the scattering and absorption (extinction) of light by spherical particles [**71**]. The resulting equation calculates the extinction spectrum of well-separated metal spheres [**48**]:

$$E(\lambda) = \frac{24\pi^2 N R^3 \varepsilon_{out}^{3/2}}{\lambda ln(10)} \left[\frac{\varepsilon_i(\lambda)}{(\varepsilon_r + 2\varepsilon_{out})^2 + \varepsilon_i(\lambda)^2} \right] \quad (3)$$

More detail on the derivation of equation (3) can be found in [**48**]. In this equation, N is the electron density, R is the nanoparticle radius, ε_{out} is the dielectric constant of the external environment surrounding the nanoparticle, and λ is the wavelength of light. Finally, ε_r and ε_i are the real and imaginary components of the metal dielectric function, which is given by [**45**]:

$$\varepsilon(\omega) = \varepsilon_r(\omega) + i\varepsilon_i(\omega) \quad (4)$$

In which ω is the angular frequency of the incoming EM field ($\omega = 2\pi c/\lambda$). The LSPR condition is met for spherical particles when $\varepsilon_r = -2\varepsilon_{out}$. This condition, known as the Fröhlich frequency, causes the denominator of the extinction equation to go to zero and produces the resonance condition and enhanced EM fields. For gold and silver, this condition is met at frequencies that lie within the visible range, which makes them suitable for many applications. This condition also explains the dependence of the LSPR position on the dielectric properties of the external medium.

This simplified Mie theory is only applicable for spherical particles that are small in size (<10nm), and does not take into account coupling between particles [**48**]. Gans theory generalizes Mie theory to spheroidal particles of any aspect ratio, which is given in [**48**] but will not be discussed here. For particles

of other shapes, numerical methods must be employed to determine the LSPR spectrum. Such methods include finite difference time domain (FDTD) [**72**], discrete dipole approximation (DDA) [**73**], finite integration technique (FIT) [**74**], and finite element method (FEM) [**75**]. An excellent review of these techniques is available in [**76**]. In all types of numerical simulations, Maxwell's equations are approximated for given particle geometries and physical properties.

2.7.2 LSPR for Biosensing

LSPR has been used in a variety of implementations to realize biomolecular sensors, which include [**70**]:

- Local refractive index changes [**48**]
- Nanoparticle aggregation [**77**]
- Resonant Rayleigh scattering from nanoparticle labels [**78**]

By far the most common implementation is as a refractive index sensor, which is the sensor design that is proposed here and hence will be the focus of this thesis. As was discussed in Section 2.7.1, the LSPR peak position depends on the local refractive index (RI). LSPR can be used as a biomolecular sensor because binding of biomolecules to the surface of the nanoparticles results in a change in the local refractive index. The binding events can therefore be monitored by monitoring the change in peak position.

This concept is illustrated in Figure 4, which shows the general design and operation of an LSPR biosensor. Metal nanoparticles are typically fabricated onto transparent substrates such as glass. A variety of nanoparticle fabrication techniques have been used, from lithographic techniques to wet chemistry synthesis. The surface of the nanoparticles is typically modified to allow specific capture of certain target biomolecules through surface functionalization techniques. For example, specific antibodies can be attached to the surface of the nanoparticles and used to capture specific proteins from a solution that contains a large amount of background protein. This allows the LSPR sensor to be specific. After an appropriate capture layer has been implemented, the target analyte is introduced to the sensor. It binds to the surface of the nanoparticles via the capture layer, resulting in a change in the local refractive index and a shift in LSPR peak position. The peak shift is monitored by illuminating the sensor with a white light source and measuring the intensity vs. wavelength using an ultraviolet-visible (UV-Vis) spectrometer. The peak amplitude can also been used to monitor the binding process, but this is less common than monitoring the peak position. The optical system can be either a reflection setup, as shown in Figure 4, or a transmission setup in which the light source and spectrometer are located on opposite

sides of the sensor chip [**48**]. The chip is typically housed inside of a flow cell made of glass or polymer to provide a small sensing volume that can be connected to external fluidic systems for sample injection.

Two implementations are typically employed for LSPR sensors: end point monitoring and continuous monitoring. In end point monitoring, the LSPR peak is measured before and after binding of the target analyte. The measurements are done while the sensor is in air; one prior to injection of the sample solution and the other after the sample has been bound to the surface and the sample has been rinsed and dried. Continuous monitoring involves monitoring the LSPR peak position in real time throughout the course of the binding event. The monitoring is done while the sensor is in a solution, typically buffer. Continuous monitoring provides more information than end point monitoring, such as on and off binding kinetics. It also allows for continuous signal filtering and averaging and as such is the method employed in the design of this sensor.

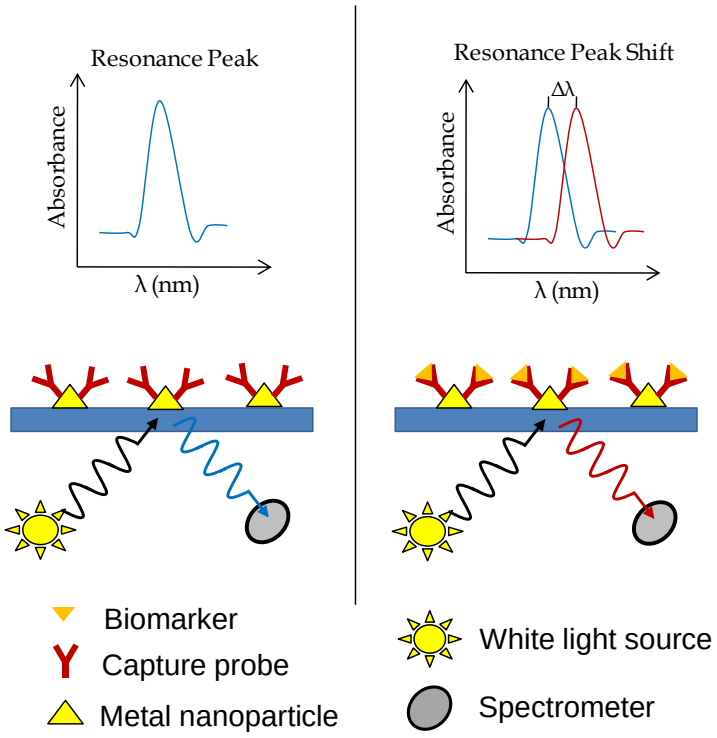

Figure 4. Illustration showing the design and operation of a typical LSPR biosensor. In the left panel, an array of metal nanoparticles on a glass substrate is functionalized with a capture layer that binds specifically to a biomolecule of interest. In the right panel, the target biomolecule binds to the surface, causing the LSPR peak to shift. This shift is measured through the use of a white light source and spectrometer.

The magnitude of the LSPR peak position shift (R), which is directly related to sensor performance, can be described as [**79**], [**80**], [**81**]:

$$R = m\Delta n[e^{\left(\frac{d_1}{l_d}\right)}][1 - e^{\left(\frac{d_2}{l_d}\right)}] \quad (5)$$

in which m is the bulk refractive index sensitivity (RIS) of the nanoparticles in nm/refractive index unit (nm/RIU), Δn is the refractive index difference between the analyte and the buffer solution (or air, if used in an end point configuration), d_1 is the thickness of the capture layer, d_2 is the thickness of the target analyte, and l_d is the effective electromagnetic (EM) field decay length, which takes into account the finite distance over which the EM field decays outside of the particle. The nanoparticle shape, size, and material determine the values of m and l_d, while the capture layer and target biomarker determine d_1, d_2, and Δn. This equation is the basic transfer function used to predict the output of an LSPR sensor.

The RIS of the nanoparticles is an important parameter that helps define the performance of the sensor. It is defined as [**46**]:

$$RIS = \frac{d\lambda_p}{dn} \quad (6)$$

In which λ_p is the peak position and n is the bulk refractive index. The RIS has been shown for a wide range of values, from 90nm/RIU to 801nm/RIU, depending on the NP material, size, and shape [**46**]. Larger RIS values result in better sensor performance as larger peak shifts are induced by analyte binding. Another important parameter that helps define LSPR sensor performance is the LSPR figure of merit (FOM), which is defined as [**46**]:

$$FOM = \frac{RIS}{\Delta\lambda} \quad (7)$$

In which $\Delta\lambda$ is the spectral linewidth, or full width half maximum (FWHM), of the LSPR peak. Sharper peaks have smaller $\Delta\lambda$ values, which increases the certainty with which the peak position can be determined, decreasing noise and increasing the LOD. FOM values from 0.8-5.4 have been demonstrated, which is dependent on the material, size, and shape as well as size distribution of the NPs [**46**].

The decay length of the nanoparticle also has a critical role in determining sensor performance. The l_d essentially determines the size of the sensing volume surrounding the nanoparticle. The electric field intensity exponentially drops with distance from the surface of the nanoparticle, so the peak position is only sensitive to changes in RI that occur within this distance. As illustrated in Figure 5, the decay length

in LSPR systems is typically 15-30nm, which is on the order of the size of many biomolecules of interest [**79**]. The binding of the analyte occurs at a distance d_1 from the NP surface, and if l_d is comparable to d_1, the binding of the analyte will result in a weak response because it is outside the range of the EM field (Figure 5a). If l_d is much larger than the analyte (d_2), the response will again be weak as the analyte takes up only a small fraction of the EM field (Figure 5c). Therefore, there is an optimal decay length for each individual capture-analyte system, which is close to the value of d_1+d_2 (Figure 5b). However, designing optimal LSPR sensors is made more complicated because the RIS and decay length are not independent, so both parameters must be optimized simultaneously [**81**]. Selection of nanoparticles with optimal decay length and sensitivity allows for improved device performance.

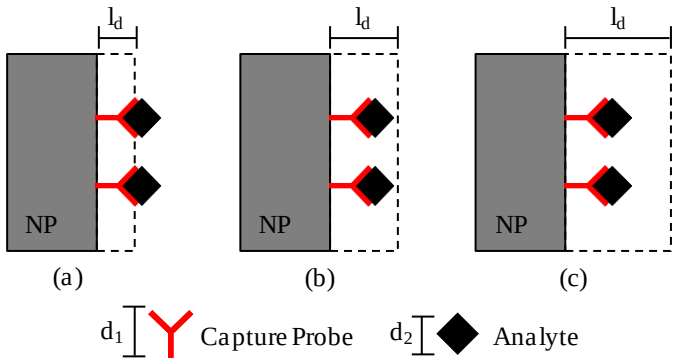

Figure 5. Illustration of an LSPR immunosensor, showing (a) a decay length which is too small, (b) an optimal decay length, and (c) a decay length which is too large. The optimal decay length results in the largest sensor response. Reprinted with permission from [82**].**

LSPR sensor performance also depends on the hardware, optics, and signal processing algorithms. Optimizing all of these aspects to reduce the noise associated with the peak position determination will lead to improved sensor performance. More information on this can be found in [**83**] and [**84**]. Also, fluidic considerations are also important to ensure rapid sensor response times are achievable [**85**]. The level of non-specific binding also affects device performance, as a large amount of non-specific binding will degrade operation at low target concentrations.

2.7.3 Literature Review of LSPR Biosensors

Recent, comprehensive literature reviews on LSPR biosensors can be found in [**45**] and [**46**]. There has been a variety of LSPR implementations in recent years and a complete review of them all here would be outside of the scope of this introduction. Instead, a summary of a selection of different implementations has been given in order to provide an overview of the LSPR biosensor field (Table 2).

Table 2. Literature summary of LSPR biosensors.

No.	Ref	Device Structure	Fabrication	Capture Layer	Format	Signal	Protein(s) Detected	Sensitivity	LOD	Range	Specificity	Time
1	[86]	Ag triangles, 93nm PB, 50nm height	NSL, 390nm PS spheres	Maleimide disulfide and 11-MUA EG3 SAM, mannose thiol capture	CF	λ	Con A	191nm/RIU	2000μg/ml	N/A	High, tested with Ery/BSA	20min
2	[49]	Ag triangles, 93nm PB, 50nm height	NSL, 390nm PS spheres	11-MUA/1-OT SAM with EDC, biotin capture	EP	λ	SA	191nm/RIU	60ng/mL	60pg/mL - 60μg/mL	High, tested with BSA	N/A
3	[50]	Ag triangles, 93nm PB, 25nm height, 0.4nm Cr adhesion	NSL, 390nm PS spheres	11-MUA/1-OT SAM with EDC, ADDL capture	EP	λ	Anti-ADDL	191nm/RIU	1500ng/mL	1.5-150μg/mL	Low, due to Cr layer	30min
4	[51]	Ag triangles, 93nm PB, 25nm height	NSL, 390nm PS spheres	11-MUA/1-OT SAM with EDC, anti-ADDL capture	EP	λ	ADDL	200nm/RIU	10pM, 100fM in sandwich	100fM-10nM	High	30-60min
5	[52]	Ag rhombic particles, 140nm width, 47nm height	NSL, 500nm PS and 200nm silica spheres	11 MUA/1-OT SAM with EDC, biotin capture	EP	λ	SA	330nm/RIU	6000ng/mL	N/A	N/A	N/A
6	[87]	Nanopyramids, 300nm length, 200nm height, 420nm spacing	NSL, 320nm silica spheres	Protein A, rabbit IgG antibody capture	EP	λ	ADH	239nm/RIU	40ng/mL	N/A	High, tested with casein	60min
7	[53]	Au nanorods, 50nm length, 15nm diameter	Solution coated	MHDA and MUD SAM with EDC/NHS, rabbit IgG capture	CF	λ	Goat anti-IgG	170nm/RIU	1nM	1-30nM	High, tested with goat antimouse-IgG	N/A
8	[88]	43nm Au spheres	Solution coated	16-MHDA SAM, biotin capture	EP	Abs and λ	Anti-biotin	62nm/RIU	5000ng/mL	5-40μg/mL	High	20min
9	[54]	100nm silica spheres, capped with 30nm Au	Solution coated	DDA SAM with EDC/NHS, protein A, various capture antibodies	EP	Abs	IgA, IgD, IgG, IgM, CRP	N/A	0.1ng/mL	100pg/mL-1μg/mL	High	30min
10	[55]	100nm silica spheres, capped with 30nm Au	Solution coated	DDA SAM with NHS/EDC, protein A, and insulin capture	CF	Abs	Anti-insulin	N/A	100ng/mL	0.1-10μg/mL	N/A	30min
11	[56]	100nm Au cylinders, 50nm height, 200nm spacing	EBL	11-MUA modified with EDC, biotin capture	EP	λ	SA	N/A	0.42ng/mL	420pg/mL-6.0μg/mL	N/A	N/A
12	[89]	160nm Au nanodisks, 500nm periodicity, 30nm height	NIL with Si mold	Biotinylation in tri-thiolated polypeptides, biotin capture	EP	λ	Anti-biotin	200nm/RIU	10μM	N/A	N/A	40-180min
13	[90]	5nm Au nanoshell	Solution coated	Cystamine monolayer with biotin-NHS capture	CF	Abs	SA	0.31au/RIU	3000ng/mL	3-50μg/mL	High, tested with BSA, whole blood	30min
14	[57]	Au bipyramids, diameter 50nm-185nm, length 442.5nm-583.2nm	Solution coated	MHDA and MUD SAM with EDC/NHS, rabbit IgG capture	CF	λ	Goat anti-IgG	289nm/RIU	1nM	1-10nM	N/A	N/A
15	[91]	50nm Au spheres	Porous alumina	11-amino-1-undecanethiol HCl, biotin capture	EP	Ref	Avidin	225nm/RIU	100ng/mL	100ng/mL-10000ng/mL	High, tested with BSA and FBS	30min
16	[92]	50nm Au spheres	Solution coated	None	EP	Abs	BSA	N/A	100μg/mL	N/A	N/A	13min

PB = perpendicular bisector, NSL = nanosphere lithography, PS = polystyrene, EBL = electron beam lithography, NIL = nanoimprint lithography, MUA = mercaptoundecanoic acid, EG = ethylene glycol, SAM = self-assembled monolayer, Ig = immunoglobulin, OT = octanethiol, EDC = carbodiimide, hydrochloride, NHS= N-hydroxysuccinimide, ADDL = amyloid beta-derived diffusible ligand, MHDA = mercaptohexadecanoic acid, MUD = mercaptoundecanol, DDA = dithiodibutyric acid, CF = continuous flow, EP = end point, Con A = concanavalin A, SA = streptavidin, CRP = C-reactive protein, ADH = alcohol dehydrogenase, BSA = bovine serum albumin, Ery = erythrina crysta galli, LOD = limit of detection

2.7.4 Motivation for Using LSPR for HSP70 Sensing

The LSPR sensing technique has been selected in this work for the development of the HSP70 sensor because it offers numerous critical advantages. As was discussed, optical sensing techniques in general have many advantages over electrical or mechanical techniques, especially in the development of low cost and portable devices. Here, the justification for using LSPR as the optical technique of choice for HSP70 sensing will be made, with reference to the design specifications laid out in the Section 2.6.

Comparing LSPR to traditional SPR, the most popular optical label-free sensing technique, reveals its numerous advantages that make it suitable for field portable monitoring of HSP70. The main advantage LSPR has over other optical label-free techniques, especially traditional SPR, is that the optical requirements and hardware are much simpler [**46**]. For example, SPR requires total internal reflection and precise monitoring and control of the SPR angle [**45**]. Neither of these requirements applies to LSPR. Consequently, the cost of an LSPR device is much less than an SPR device. Typically, SPR systems cost $150,000-$300,000, while the cost of an LSPR system can be less than $5,000 [**70**]. With the cost requirement for the HSP70 device to be less than $10,000, LSPR is the clear choice. In terms of the per test cost, the use of large scale lithographic techniques to produce the nanoparticle arrays should allow the cost per test to meet the requirement of <$5/test. All of these advantages come without any adverse effects on sensitivity, as it has been demonstrated experimentally that LSPR and SPR have very similar sensitivity to biomolecular binding events [**86**].

Another important advantage of LSPR is that it is less sensitive to temperature fluctuations [**46**], [**56**], [**70**], [**83**], [**93**]. Compared to SPR, which requires temperature control to 0.01-0.1°C [**44**], LSPR requires temperature control to only 1°C [**94**]. Since the device is required to operate over a large range of temperatures (4-25+°C), LSPR requires significantly simpler packaging and temperature compensation mechanisms. It also has a very small sensing distance (~10nm compared to ~1000nm for SPR) [**46**], which reduces interference from other bulk effects. Having a less complex device also implies less maintenance, reduced probability of failure, and easier repair, making LSPR more suitable for rugged field use. It also means that the device size can be reduced to allow for easy transportation in a portable format [**70**], which has already been demonstrated to be possible for LSPR devices [**88**], [**95**], [**96**], [**97**], [**98**].

Being a label free optical technique, it does not require expensive, complex fluorescent labels like many traditional optical biosensing techniques [**46**]. Once the sensors have been functionalized, the sensing protocol is very simple and only involves a few steps. This allows a non-technical user to operate the

device without needing a dedicated, trained technician. Another advantage is the ability to detect multiple biomarkers simultaneously [**54**]. SPR is inherently difficult to multiplex [**24**], especially compared to LSPR.

The detection time of LSPR sensors is adequate for rapid HSP70 detection, as it is typically less than 30 minutes. The limit of detection and dynamic range required for the HSP70 sensor (1ng/ml, 1-50ng/ml) also appear to be achievable with LSPR technology. Examining previous literature shows detection limits as low as 0.1ng/ml with a dynamic range from 0.1ng/ml-1μg/ml. It has shown to have reproducibility of better than 5% across 20 measurements [**99**], which satisfies the reproducibility requirement. Sample volumes of less than 60μL have been demonstrated [**99**], fitting within the <100μL requirement. Non-specific binding can be limited by appropriate surface treatment protocols, allowing highly specific detection [**70**], [**100**]. Detection of proteins from complex samples has indeed been demonstrated [**51**], [**90**]. Since LSPR uses the same material as SPR sensors, i.e. gold, many of the same surface functionalization and blocking protocols can be adopted, significantly reducing the development work required [**86**].

Since LSPR biosensors satisfy many of the design requirements and offer the most complete package, it has been selected as the technique to use to develop the HSP70 sensor. The remainder of this thesis will focus on the design of the LSPR device for optimal HSP70 detection, followed by experimental implementation and preliminary results.

Chapter 3
Sensor Design and Modeling

In this chapter, an overview of the LSPR HSP70 sensor is given, followed by the simulations used to design an optimal HSP70 sensor. The final simulation (the sensor response model) allows input of a bulk protein concentration and output of the shift in LSPR peak position that would occur. The final simulation is made up of two different sub-simulations. Optical simulations in Computer Simulation Technology Microwave Studios (CST MWS) are used to design optimal nanostructures for HSP70 detection by finding the optimal sensitivity and decay length. COMSOL is used to simulate the kinetics of the binding reaction and the fluidic transport in the flow cell in order to optimize the sensor size and channel dimensions. The results from both CST MWS and COMSOL simulations are combined to predict the performance of the HSP70 sensor, including dynamic range, limit of detection, sensitivity, and resolution.

3.1 Overview of Sensor Design

In this section, the general design of the LSPR HSP70 sensor is presented. This includes the nanoparticle sensor chip, the fabrication method, the capture layer and biomolecules employed, and the flow cell used to house the sensor.

3.1.1 Nanoparticle Sensor Chip

The specific design of the nanoparticles is dictated by the capabilities of the fabrication method employed. Electron beam lithography (EBL) was selected as the most flexible and precise technique for nanoparticle fabrication. The Nanofabrication Facility at the University of Western Ontario was selected for fabrication services as it had a pre-developed process. Using their process, gold and silver nanoparticles could be made in almost any shape or size (~10nm to several hundred nm) on top of transparent glass wafers. However, it was found early on that silver was unstable and oxidized quickly. Therefore, gold was the material of choice.

3.1.2 Capture Layer

Alkanethiol SAMs were chosen as the biointerface because of their ease of use, customizable head groups, ability to reduce non-specific binding [**101**], biocompatibility [**102**], nanoscale thickness [**103**], and selective adsorption onto gold surfaces. The alkanethiols used here were 1-octanethiol (1-OT), an eight carbon long alkanethiol with a methyl head group, which was used as a spacer for the longer 11-mercaptoundecanoic acid (11-MUA), an eleven carbon alkanethiol with a carboxyl head group. The head

groups of the 11-MUA were conjugated to bind to the capture probe (antibodies) through the use of the zero-length EDC/NHS conjugation chemistry [**36**]. This allowed efficient antibody coupling to the carboxyl groups of the thiolated sensor surface via binding to the antibodies' amino groups [**36**], [**104**], [**105**], allowing highly specific capture of the target analyte.

Two different biological systems were used in this study: the biotin-streptavidin system and HSP70 and its antibody. Both of these systems will be described below.

The well-studied biotin and streptavidin (SA) system was used in this study to experimentally investigate and characterize the performance of the LSPR sensor. Biotin is a 244 dalton (Da) water-soluble B-complex vitamin commonly found in cosmetic and health products. It is necessary for cell growth, production of fatty acids, and metabolism of fats and amino acids [**106**]. SA is a 60 kDa tetrameric protein, which can bind up to four biotin molecules with minimal impact on its biological activity [**100**]. The biotin-SA system has an extremely high binding affinity ($K_a=10^{13}$ - 10^{15} M^{-1} when in solution [**56**], [**100**], [**107**]). Its binding has been long regarded as the strongest, noncovalent biological interaction known [**108**]. This high binding affinity and stability of the biotin-streptavidin complex make it an excellent model system for studying biosensor performance. It is also lower cost compared to many other available protein-antibody systems, and it is easier to prepare and handle without compromising its activity. Here, biotin (modified with an amine group) is attached to the NP surface through the 11-MUA SAM, allowing specific capture of streptavidin to the sensor surface.

Figure 6(a) illustrates the structure of a biotin molecule, and Figure 6(b) shows how it binds within a hydrophobic pocket on the SA protein. It is held in place by an extensive hydrogen-bonding network among a number of other intermolecular interactions that make the biotin-SA bound so strong. Figure 6(c) represents the entire biotin-SA complex, which is very robust due to its resistance to organic solvents, denaturants and wide ranges of pH and temperature [**108**]. The high affinity, specificity, and reliability of this system underlie its importance in the biological and biomedical fields [**107**], and its use in diverse applications in immunology, histochemistry, in situ hybridization, affinity chromatography and many other areas [**106**], [**108**].

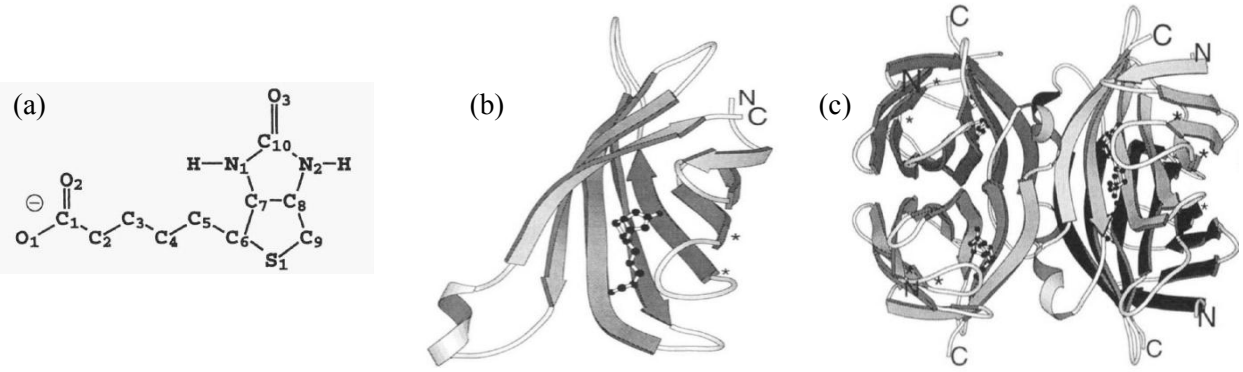

Figure 6. (a) Biotin molecule structure and (b) illustration of biotin bound to one of the four binding sites within SA, in a hydrophobic pocket with an extensive hydrogen-bonding network. (c) Biotin - streptavidin complex, showing all four binding sites on the large, 60 kDa SA filled by the 244 Da biotin molecules. Adapted and reprinted with permission from [109**].**

Heat shock protein 70 (HSP70) is part of a large family of heat shock proteins, each named for their size in kilodaltons [**110**]. HSPs are highly conserved proteins, meaning they exist in a similar structure in essentially all living organisms. HSPs are abundant proteins in cells, with up to 5% of proteins being HSPs [**110**]. As a molecular chaperone inside of the cell, it performs multiple functions, including protein translocation [**111**], [**112**], stabilization [**113**], [**114**] and refolding [**111**], [**114**], [**115**], higher order protein assembly [**111**], and degradation of irreversibly denatured proteins [**116**]. HSP70 recognizes and binds to nascent polypeptide chains or partially folded intermediates of proteins, preventing their aggregation and misfolding [**117**]. The binding of adenosine triphosphate (ATP) triggers a critical conformational change leading to the release of the bound substrate protein [**117**]. HSP70 is produced at much higher levels in response to external stress stimuli, as has been discussed previously. Intracellular HSP70 up-regulation due to increased environmental temperature, typically 5-10°C [**118**], is the most commonly researched and best understood of these stimuli, occurring in nearly all organisms studied. However, HSP70 levels are also affected by a variety of environmental factors, such as pollution [**13**] or food deprivation [**10**], making them an excellent wildlife biomarker. In humans HSP70 levels have been associated with inflammation, ischemic diseases, infection, and cancer [**110**], making it an interesting biomarker for a variety of diseases and conditions. Because of its wide applicability, a label-free HSP70 sensor would be extremely useful in a variety of areas.

As its name implies, HSP70 is a 70 kDa protein. The structure of HSP70, shown below in Figure 7 [**110**], consists of two major domains: a highly conserved N-terminal ATPase domain and a less conserved C-terminal peptide binding domain. The HSP70 used in this study is commercially available synthetic

Chinook salmon HSP70 recombinant protein expressed in E. coli. Polyclonal rabbit anti-HSP70 with specificity to salmonid HSP70, also commercially available, is used as the capture probe. It is bound to the NP surface via the 11-MUA SAM.

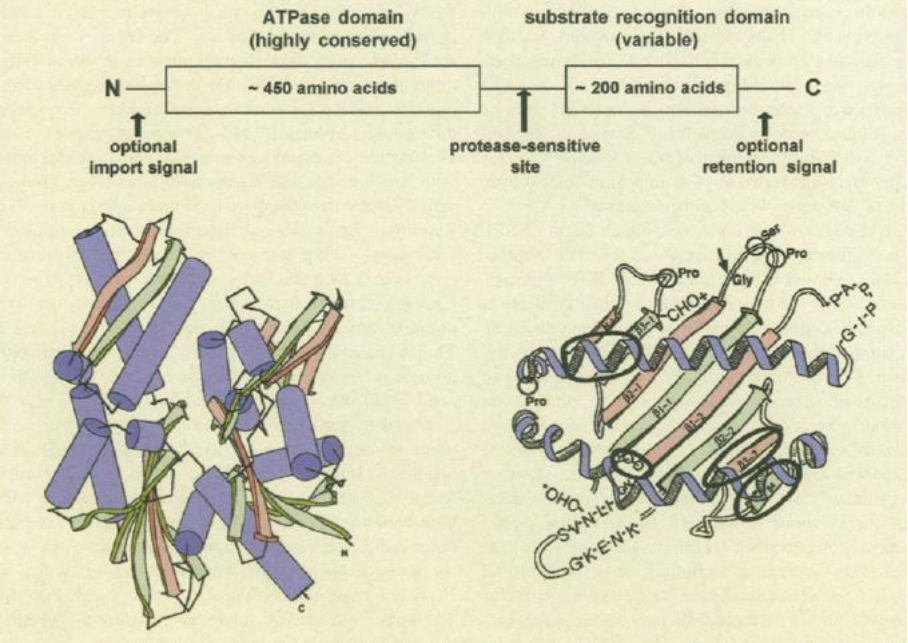

Figure 7. The structure of HSP70, showing its two major domains: a highly conserved N-terminal ATPase domain (left), and a less conserved C-terminal peptide binding domain (right). Reprinted with permission from [110**].**

3.1.3 Flow Cell

The flow cell is designed to provide a channel in which the nanoparticle sensor array is positioned, along with an inlet and outlet for sample injection. The flow cell is transparent to allow light to pass through it. The channel is made in polydimethylsiloxane (PDMS) and is sealed with glass, both of which exhibit low protein adsorption and are highly stable in a variety of solvents. The PDMS channel is made from a molding process using a CNC machined aluminum mold. The dimensions of the microchannels that can be produced using this process range in width from ~100μm to several mm, and in height from ~50μm to several mm. Other processes, such as glass etching, can be utilized to produce microchannels with smaller dimensions, but are not utilized here.

3.2 Optical Simulations

As discussed in previous sections, designing NPs with optimal sensitivity and decay length for the specific biomarker of interest allows for improved sensor performance. 3D numerical modeling using the

software CST MWS was performed to examine the optical properties of various NP geometries. The decay length and sensitivity were determined for various geometries of gold NPs, and the optimal geometry selected based on the maximum peak shift attainable for HSP70 binding.

3.2.1 Model Construction

The optical properties of the NPs under study were determined using CST MWS, a commercial software package which solves Maxwell's equations in 3D using the finite integration technique (FIT). CST MWS allows for modeling of NPs of any shape, size, or material through the use of a 3D computer-aided design (CAD) environment. CST MWS is used to determine the reflection and transmission coefficients, or scattering parameters (S-parameters), of the NP structure over the frequency range of interest. An extraction technique is then used to calculate the effective refractive index and impedance of the NP structure from the simulated S-parameters, the details of which can be found in [**119**]. The simulation geometry, shown in Figure 8, consists of a single metal NP within a homogenous background medium of air, the size of which defines the bounding box of the simulation. The bounding box is referred to as the unit cell, as it is repeated infinitely in the xy-plane using periodic boundary conditions. The top and bottom boundaries of the bounding box are defined as waveports, so that the EM wave propagates in the z-direction. This effectively models a symmetric, infinite array of metal NPs in the xy-plane with EM excitation in the z-direction. The waveports are placed at a distance of 100nm (h_{bg}) from the top and bottom of the NP structure, to ensure that the EM field outside the NP is captured. The periodicity of the NPs is defined by the width (w_{bg}) of the bounding box, which changes depending on the size of the particle investigated (w_{np}), in order to keep a constant areal density (typically 2.8%). The height of the NP layer is given by h_{np}.

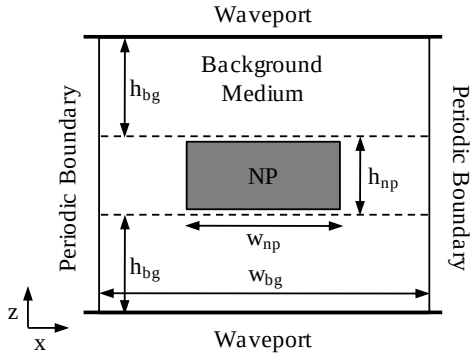

Figure 8. Side-view illustration of the model constructed for this study. The NP is surrounded on all sides by a uniform background of air, and repeated infinitely in the xy-plane. Waveports are placed in the z-plane for EM excitation. Reprinted with permission from [82**].**

In all simulations, CST MWS's frequency domain solver is used, with a typical range of $3x10^5$ GHz (999nm) to $7x10^5$ GHz (428nm). A broadband frequency sweep determines the S-parameters to within an error threshold of 0.01. A tetrahedral mesh is used with the number of elements ranging from 25,000 to over 100,000. Automatic mesh refinement is used to increase mesh density in critical areas, such as at the corners and edges of the NP. The calculated S-parameters are exported and post-processed using MATLAB code to extract the effective optical properties. The effective NP layer is assumed to be on a substrate of glass (RI = 1.52) in air, and Fresnel equations [**120**] are used to generate the reflection, transmission, and absorbance spectra over the frequency range investigated. The LSPR peak position and characteristics are then calculated from the absorbance spectra.

Although a substrate is used in the Fresnel equation, it is not considered in the numerical simulation. The substrate is known to affect the LSPR properties [**119**], but it was not included here in order to simplify the model. The addition of a substrate creates an inhomogeneous structure and adds significant time to the simulation. Therefore, the results presented here can be expected to overestimate the actual sensitivity, but will likely have only a minimal effect on the decay length [**121**].

3.2.2 Determining Sensitivity and Decay Length: the Shell Method

The calculation of the decay length and sensitivity from the CST MWS simulations can be done through the use of a shell model technique. In this technique, a shell of water is added to the model presented above. The water shell completely encloses the NP uniformly on all sides. The shell thickness starts at 5nm and extends in steps of 5nm to a distance of 50nm. For example, for a NP of 75nm width and 75nm height, the water shell would be centered over the NP with dimensions starting from 80nmx80nm and growing in steps of 5nm to 125nmx125nm. This closely resembles the case of a real LSPR sensor in which biomolecule layers form a conformal coating over the NP surface. The decay length and sensitivity are found by calculating the LSPR peak shift for each shell thickness and performing non-linear least squares regression with MATLAB using the following LSPR response equation:

$$R_i = x(1)\left[1 - e^{\frac{-d_i}{x(2)}}\right] \qquad (8)$$

In which R_i is the peak shift from air ($R_i = \lambda_i - \lambda_{AIR}$) for a shell of thickness d_i, for i=5-50nm. The variables *x(1)* and *x(2)* are optimized until the error in the regression is below the threshold value. The decay length is given by *x(2)*, while *x(1)* is approximately equal to $m\Delta n$, which allows estimation of the sensitivity since the refractive index increment is known (Δn=0.33 for the difference between water and air).

The shell method was chosen to find the NP properties because the decay length is a parameter that is geometrically variant. The simplest method to find the decay length would be to fit an exponential curve to the EM field magnitude along a reference line outside of the NP. However, examination of the 3D distribution of the EM field surrounding the NP reveals that the decay length is not constant over the NP [**122**], [**123**]. Therefore, the decay length would depend on the location of the chosen reference line, and would not be representative of the average NP decay length. Using the shell method, the average decay length can be found, which is a more useful value and more representative of the typical sensor operation.

3.2.3 Nanoparticle Material and Geometry

The NP material chosen in this study was gold. The bulk permittivity dispersion of gold is given by Johnson and Christie [**124**], which is fit by CST MWS using a 6^{th} order polynomial. Various NP shapes and sizes were used in this study, including square prisms, triangular prisms, and cylinders, which are summarized in Table 3. The shapes chosen were those that could be easily fabricated through electron beam lithography, to enable future validation of the model with experiments. The effect of the NP size on the sensitivity and decay length was investigated using square prisms, with nine different sizes. Three different sets of widths were tested with three different heights, keeping the same aspect ratios (w/h) of 1, 2, and 10. The periodicity was set to give a constant areal density of 2.8% for each of the widths tested. To find the decay length and sensitivity, a water shell starting from 5nm from the surface was extended in steps of 5nm to a final distance of 50nm.

The effect of the NP shape on the decay length and sensitivity was investigated using square prisms, triangular prisms, and cylinders (see Table 3 for a summary of the NP geometries investigated). The critical dimension (w_{np}) for each shape was fixed at 50nm, which for the square prism was the width, for the triangular prism was the perpendicular bisector, and for the cylinder was the diameter. Three different heights, 50, 25, and 5nm, were tested for each shape to investigate the effect of aspect ratio. For simplicity, the size of the bounding box was kept constant at 300nm, which resulted in slight differences in the areal density between shapes. The sensitivity and decay length were found as described previously.

Table 3. Summary of the geometrical parameters of the NPs used to investigate the effect of size and shape on the sensitivity and decay length.

Shape	w_{np} (nm)	h_{np} (nm)	Aspect Ratio (w/h)	w_{bg} *(nm)*	Areal Density (%)	Interparticle Distance (nm)
Square Prism	75	75	1	450	2.8	375
Square Prism	75	37.5	2	450	2.8	375
Square Prism	75	7.5	10	450	2.8	375
Square Prism	50	50	1	300	2.8	250
Square Prism	50	25	2	300	2.8	250
Square Prism	50	5	10	300	2.8	250
Square Prism	25	25	1	150	2.8	125
Square Prism	25	12.5	2	150	2.8	125
Square Prism	25	2.5	10	150	2.8	125
Triangular Prism	50	50	1	300	1.6	246
Triangular Prism	50	25	2	300	1.6	246
Triangular Prism	50	5	10	300	1.6	246
Cylinder	50	50	1	300	2.2	250
Cylinder	50	25	2	300	2.2	250
Cylinder	50	5	10	300	2.2	250

3.2.4 Results and Discussion

A representative 2D cross sectional surface plot of the electric field generated by 75nmx75nmx37.5nm square gold nanoparticles in air at their resonance frequency is shown below in Figure 9. The result was produced in CST MWS using air as the background with no water shell with EM excitation from the bottom waveport. Strong field enhancement can be seen at the corners and surface of the nanoparticles.

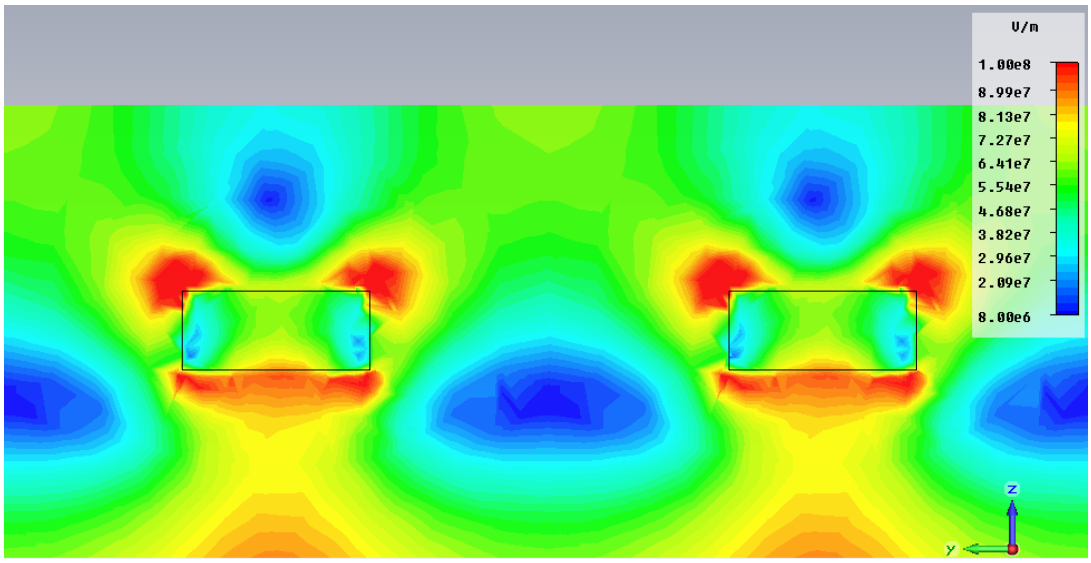

Figure 9. 2D cross section surface plot of the electric field surrounding 75nmx75nmx37.5nm square gold nanoparticles in air, simulated in CST MWS at their resonant frequency.

Examples of the simulation output for the absorbance spectrum of different NP shapes are shown in Figure 10 below, for shell thicknesses from 5nm to 50nm. The results for a square NP of 75nm width and 75nm height are shown in Figure 10a, the results for a triangular NP with perpendicular bisector of 50nm and height of 50nm is shown in Figure 10b, and the results for a cylindrical NP with diameter of 50nm and height of 50nm is shown in Figure 10c. The LSPR peak is clearly visible for all shapes, and red shifts as the shell thickness increases. This is the expected trend since the surrounding RI increases as the shell thickness increases. The incremental peak shift decreases as the shell thicknesses increases as the decay length is reached. Also, the peak height increases and the full width at half maximum (FWHM) decreases as the shell thickness increases. Similar results were seen for all of the other sizes tested.

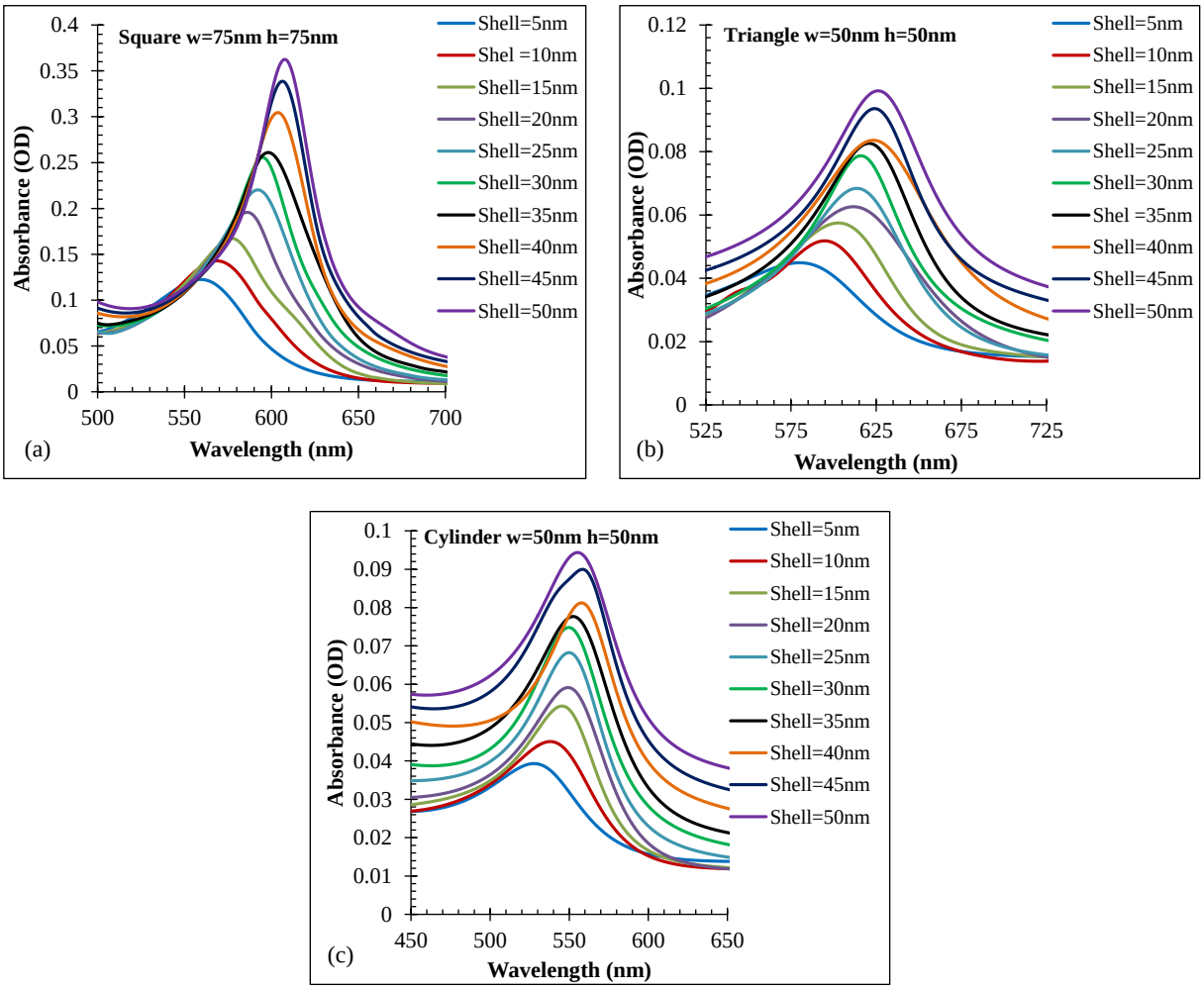

Figure 10. Simulation results of the absorbance spectrum for shell thicknesses from 5 to 50nm for (a) square NPs of width 75nm and height 75nm, triangular NPs with perpendicular bisector of 50nm and height of 50nm, and (c) cylindrical NPs with diameter of 50nm and height of 50nm. The LSPR peak is clearly visible in all cases and shifts to the red as the shell thickness increases. Reprinted with permission from [82**].**

The shift in peak position for each shell size with respect to the case of having no shell, in a complete air environment, was calc1ulated for each of the 15 NP geometries. As the shell thickness increases, the incremental peak shift reduces as the shell thickness approaches the decay length. The data was fit with equation (8) to determine the decay length and sensitivity. In Figure 11 below the simulation data is plotted along with the curve fit for all 15 NP geometries investigated. Although there are a few peak positions that are off the fitted curve, in general the data fits the equation very well. The erroneous points are likely due to meshing problems in the simulations that produce peaks that are slightly misshapen, resulting in inaccurate peak positions. From the results of the fit, the decay length and sensitivity are extracted, and are summarized in Table 4. Many interesting trends between decay length, sensitivity, size,

and shape can be observed from this data. However, its discussion is outside of the focus of thesis, but can be found in detail in [**82**].

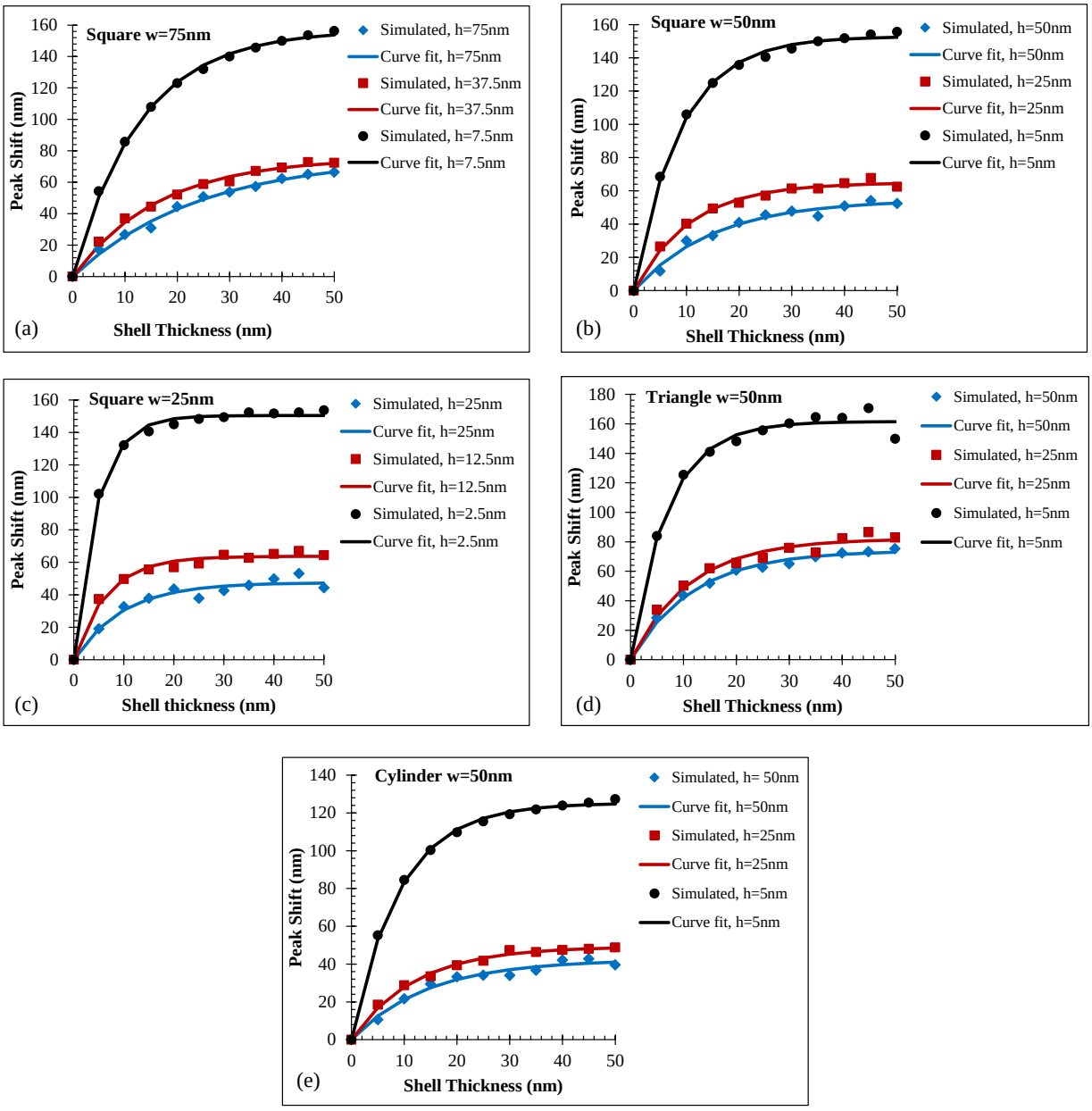

Figure 11. Summary of the simulated LSPR peak position shift for shell thicknesses from 0-50nm for all 15 different NP geometries investigated. Square NPs with widths of 75nm, 50nm, and 25nm and three different heights are shown in (a)-(c). Triangular NPs with a perpendicular bisector of 50nm and three different heights are shown in (d). Cylindrical NPs with a diameter of 50nm and three different heights are shown in (e). Reprinted with permission from [82**].**

The decay length and sensitivity determined here can be used to optimize the design of the LSPR sensor. In order to do that for HSP70, it is important to know the size of the protein and the size of capture layer. As discussed, this determines the optimal decay length, which can be optimized together with the sensitivity to yield the maximum LSPR peak shift. Here, a capture layer of 11-MUA, estimated to be 1.57nm thick [**100**], is assumed for immobilization of the capture antibody, anti-HSP70, via a zero length EDC-NHS coupling chemistry [**36**]. The anti-HSP70 is assumed to be similar in size and structure to an immunoglobulin G (IgG) protein. Although the effective thickness of this layer would greatly depend on the density and orientation of the antibody, a value of 4nm is chosen, which has been reported previously for human IgG on alkanethiol monolayers [**79**], [**125**]. This gives a capture layer thickness, d_1, of approximately 5.57nm. The sensor surface is assumed to be saturated with HSP70, with a thickness of 4nm (d_2) and a refractive index of 1.4, common values for other similar proteins [**79**], but both of which would vary depending on the density of bound protein. It should be noted that these parameters need to be determined experimentally for the specific protein system under study in order to obtain the most accurate optimization. Finally, we assume that the sensor is being operated in a real time configuration, so the sensing is being performed in a surrounding medium of buffer with a refractive index close to water (RI = 1.33).

Inserting these constants into equation (5) gives the function to be maximized, which is the change in LSPR peak position, through adjusting m and l_d. Here the values of m and l_d are restricted to those determined in the previous simulations. The shift in LSPR peak position for each set of m and l_d is given in Table 4. As indicated in Table 4, the optimal NP geometry is found to be the triangle with a width of 50nm and a height of 5nm. In this case, an l_d of 6.952nm and a sensitivity of 489.8nm/RIU results in an LSPR shift of 6.731nm, which is a 354% improvement over the most non-ideal case (1.482nm peak shift). Hence, the improvement seen in the LSPR peak shift by choosing the optimal NP is dramatic and results in significant improvements in the performance of the sensor.

Table 4. Summary of the sensitivity and decay length for each NP simulated. The maximum shift in LSPR peak position upon binding of a monolayer of HSP70 to an anti-HSP70 capture layer was calculated for each NP. The optimal NP geometry is highlighted.

Shape	w_{np} (nm)	h_{np} (nm)	l_d (nm)	m (nm/RIU)	R (nm)
Square	75	75	24.13	230.8	1.959
	75	37.5	16.35	229.3	2.478
	75	7.5	12.85	475.6	5.773
	50	50	15.07	165.4	1.866
	50	25	10.58	196.7	2.560
	50	5	8.745	463.2	6.295
	25	25	9.679	143.9	1.917
	25	12.5	6.524	193.0	2.637
	25	2.5	4.613	455.7	5.529
Triangle	50	50	11.80	224.0	2.812
	50	25	11.13	248.8	3.188
	50	5	6.952	489.8	6.731
Cylinder	50	50	14.28	128.0	1.482
	50	25	11.99	149.3	1.864
	50	5	9.088	379.4	5.123

3.3 COMSOL Model

A COMSOL model was constructed to model the transport and binding of HSP70 to the nanoparticle sensor located inside of a microchannel. The main parameters investigated to determine the optimal sensor design were the size of the sensor array and the microchannel height.

3.3.1 Model Construction

A 2D model was constructed of a rectangular microchannel and square sensor array in COMSOL 4.2a. The model is based on similar work reported in literature [**126**], [**127**], [**128**], [**129**]. The model uses three physics modules: laminar flow, transport of dilute species, and surface reactions. The laminar flow module solves for the fluid flow in the channel, the transport of dilute species module solves for the diffusion of analyte (HSP70) in the microchannel, and the surface reactions module solves for the binding of analyte to the surface of the reaction boundary (the sensor).

The channel geometry is shown below in Figure 12. The channel is defined by the length (l), which was always kept constant, the height of the channel, h, which was variable, and the length of the sensor array, l_S, which was also variable. The left boundary was taken to be the channel inlet and the right boundary the outlet. The sensor array was assumed to be a square, so that the width would be equal to the length. The channel width was assumed to always be equal to the width of the sensor array. Therefore, compared to using a 3D model, a simplified 2D model will have a small degree of error as the binding rate of analyte to the sensor near the walls will be reduced due to wall effects that are not considered in this 2D model.

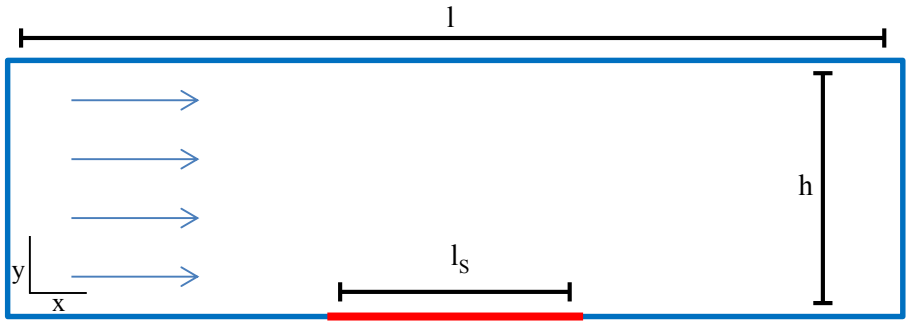

Figure 12. Diagram of geometry used to model the transport and binding of HSP70 to the LSPR sensor in COMSOL.

The laminar flow module uses the incompressible Navier-Stokes equation to solve for the velocity vector, **u** (m/s), in the x and y directions throughout the subdomain with the following governing equations:

$$\rho \boldsymbol{u} \cdot \nabla \boldsymbol{u} = \nabla \cdot (-p\boldsymbol{I} + \eta(\nabla \boldsymbol{u}) + (\nabla \boldsymbol{u})^T) \quad (9)$$

$$\nabla \cdot u = 0 \quad (10)$$

In which **I** is the identity matrix, η is the dynamic viscosity (Pa*s), ρ is the density (kg/m^3), and p is the pressure inside the channel (Pa). The left boundary is set to an inlet velocity boundary condition in which the velocity along the boundary is equal to v_0, which is the inlet velocity of the fluid (m/s). The right boundary is set to a pressure outlet, in which the pressure along the boundary is set equal to p_0. This outlet pressure is set to 0 Pa here to model an open system in which there are no applied forces at the outlet. All other boundaries are set to no slip boundary conditions in which the velocity along the wall is set to 0.

The diffusion of the analyte through the bulk is solved for in the transport of dilute species module. The transport of the analyte throughout the channel is governed by the traditional convection-diffusion equation:

$$\frac{\partial c_a}{\partial t} + \nabla \cdot (-D_a \nabla c_a) + \boldsymbol{u} \cdot c_a = 0 \quad (11)$$

In which c_a is the concentration of the analyte in the bulk, D_a is the diffusion constant of the analyte (m^2/s), and **u** is the velocity vector found from the solution of the laminar flow module. The left boundary is defined as an inflow boundary in which the concentration along the boundary is set equal to c_0, which is the initial bulk concentration of the analyte. The right boundary is set to an outflow boundary condition:

$$\boldsymbol{n} \cdot (-D_a \nabla c_a) = 0 \quad (12)$$

In which **n** is the normal vector. All other boundaries, except the reaction boundary, are set to no flux boundary conditions. The initial concentration of analyte in the channel is set to 0. At the reaction boundary, the adsorption of analyte gives rise to a net flux outwards:

$$N_a = -r_{ads} + r_{des} \quad (13)$$

In which N_a is the flux of analyte, r_{ads} is the adsorption rate of analyte to the surface and r_{des} is the desorption rate of analyte from the surface of the sensor.

The reaction rate of the analyte depends on the local concentration of analyte, which is solved for using the surface reactions module. It solves for the tangential flux inwards along the reaction surface, known as the surface molar flux, $N_{t,a}$ (mol/m*s), using the following equations:

$$N_{t,a} = -D_{s,a} \nabla_t c_{s,a} \quad (14)$$

$$\frac{\partial c_{s,a}}{\partial t} + \nabla_{\mathrm{t}} \cdot \left(-D_{s,a} \nabla c_{s,a}\right) = R_{s,a} \quad (15)$$

In which $c_{s,a}$ is the surface concentration of the analyte, $D_{s,a}$ is the surface diffusion constant of the analyte, and $R_{s,a}$ (mol/m^2*s) is the sum of all of the sources due to adsorption/desorption and surface reaction processes. In this case, surface diffusion of the analyte is ignored, and so the rate of the reaction is given by:

$$\frac{\partial c_{s,a}}{\partial t} = r_{ads} - r_{des} \quad (16)$$

The reaction rates are given by simple first order reaction kinetics for an analyte binding to an immobilized capture probe:

$$r_{ads} = k_{ads} * c_a * (B_0 - c_{s,a}) \quad (17)$$

$$r_{des} = k_{des} * c_{s,a} \quad (18)$$

In which k_{ads} is the adsorption rate constant (m^3/mol*s), k_{des} is the desorption rate constant (1/s), and B_0 is the density of binding sites of the capture probe (mol/m^2). Since the reaction rate is dependent on the concentration of the bulk analyte, it is coupled back to the equations in the transport of dilute species module.

The mesh used was a triangular mesh with a rectangular boundary layer along the walls of the microchannel. The mesh density of the triangular mesh in the bulk of the channel was set to coarse. Along the reaction boundary, the mesh was set to extremely fine, in order to accurately model the reaction and diffusion processes occurring there. A stationary solver was used to solve for the fluid dynamics module, while a time dependent solver was used for the other two physics modules. The time dependent solver was typically set to run for a total of 30 minutes (1800 seconds) and output the results every 100 seconds.

The surface concentration of the analyte (HSP70) is the parameter used to compare the results from the different microchannel and sensor geometries. From the results of the simulation, the surface concentration of the analyte was determined by calculating the average value of the surface concentration over the reaction boundary for each time step. This represents the amount of protein bound to the sensor surface, which therefore determines the response of the LSPR sensor.

3.3.2 Model Parameters

The different microchannel geometries, sensor geometries, and inlet velocities used in the simulations are summarized in Table 5 below. The length of the channel was always kept constant at 2.5mm. Three different channel heights were used: 10µm, 100µm, and 1000µm. Three different sensor array lengths were tested: 10µm, 100µm, and 1000µm. Each height was tested with each sensor size, giving a total of 9 different combinations. As was stated earlier, the width of the sensor was assumed to be the same of the length of the sensor, which was also assumed to be the same as the width of the channel. This resulted in different cross sectional areas for each microchannel tested. If the same inlet velocity was used for each geometry, each geometry would have a different volumetric flow rate. To keep comparisons between geometries meaningful, the volumetric flow rate was held constant and the inlet velocity adjusted to give the same volumetric flow rate for each geometry. The volumetric flow rate was chosen to be the rate required to pump 100µL of sample through the sensor in 30 minutes, which is the same as the requirements for the HSP70 sensor outlined in section 2.6. This resulted in a volumetric flow rate of

3.33µl/min. Using this value and the cross section of each geometry, the inlet velocities in Table 5 were calculated.

Table 5. Different microchannel and sensor geometries and the associated inlet flow rates used in the simulations.

h (µm)	l_s (µm)	Cross Section (μm^2)	v_0 (m/s)
10	10	100	$5.56e^{-1}$
100	10	1000	$5.56e^{-2}$
1000	10	10000	$5.56e^{-3}$
10	100	1000	$5.56e^{-2}$
100	100	10000	$5.56e^{-3}$
1000	100	100000	$5.56e^{-4}$
10	1000	10000	$5.56e^{-3}$
100	1000	100000	$5.56e^{-4}$
1000	1000	1000000	$5.56e^{-5}$

The rest of the simulation parameters, which were kept constant, are summarized in Table 6. Fluid properties (density and viscosity) were assumed to be that of water [**128**], [**130**]. The properties of HSP70 and its antibody were more difficult to define accurately as they have not been reported in literature. To estimate these parameters, literature values from similar protein-antibody systems were used. The kinetic constants were estimated from LSPR studies of IgG binding to anti-IgG on gold nanorods [**53**]. From this study, k_{ads} was experimentally determined to be $1.30x10^2$ $m^3/mol*s$ and k_{des} was determined to be $6.5x10^{-5}$ 1/s. The diffusion constant for HSP70 was assumed to $1x10^{-11}$ m^2/s, which is a common value for many proteins [**129**]. The density of anti-HSP70 sites is highly dependent on the size and orientation of the antibody, neither of which is well known for the antibody used here. Examining a similar biomolecule, IgG, literature often reports a flat-on orientation for a full monolayer, which corresponds to a density of approximately $200ng/cm^2$ [**79**], [**125**]. Assuming a similar mass density for anti-HSP70, a molar density of $1.33x10^{-8}$ mol/m^2 can be calculated.

Table 6. Simulation parameters used to model the HSP70 sensor in COMSOL.

Parameter	Description	Value
ρ	Fluid density	1000 kg/m^3
η	Fluid dynamic viscosity	1.00x10^{-3} Pa*s
D_a	Diffusion coefficient HSP70	1.00x10^{-11} m^2/s
B_0	Anti-HSP70 surface density	1.33x10^{-8} mol/m^2
k_{ads}	Adsorption rate constant	1.30x10^2 m^3/mol*s
k_{des}	Desorption rate constant	6.50x10^{-5} 1/s
Q	Volumetric flow rate	3.33µl/min
L	Length of channel	2.5mm

The bulk inlet concentrations tested for HSP70 were chosen so that the entire range of the sensor's response, from below the detection limit to above saturation, could be investigated. The 10 values of the inlet concentrations used have been summarized in Table 7 below, showing the concentrations in three different units: ng/ml, nM, and mol/m^3.

Table 7. Summary of bulk HSP70 concentrations tested in the simulations.

c_0 (ng/ml)	c_0 (nM)	c_0 (mol/m^3)
0.10	0.0014	1.40x10^{-9}
1.0	0.014	1.40x10^{-8}
10	0.14	1.40x10^{-7}
50	0.71	7.10x10^{-7}
100	1.43	1.43x10^{-6}
500	7.14	7.14x10^{-6}
1000	14.3	1.43x10^{-5}
2000	28.6	2.86x10^{-5}
4000	57.1	5.71x10^{-5}
44800	640	6.40x10^{-4}

3.3.3 Results and Discussion

Each of the geometries was simulated with its associated inlet velocity over the range of HSP70 concentrations outlined previously. Each simulation was solved for 30 minutes (1800 seconds) and the average surface concentration of HSP70 determined for each time and concentration. An example of the

average surface concentration (c_s) for each inlet concentration for the 100µmx100µm case is shown below in Figure 13. The surface concentration increases over time for all of the concentrations, with the higher concentrations resulting in a more rapid rate of increase. The three highest concentrations result in the majority of the antibody sites being saturated by the end of the 1800 seconds, as the protein surface concentration is approximately equal to the density of binding sites for these cases.

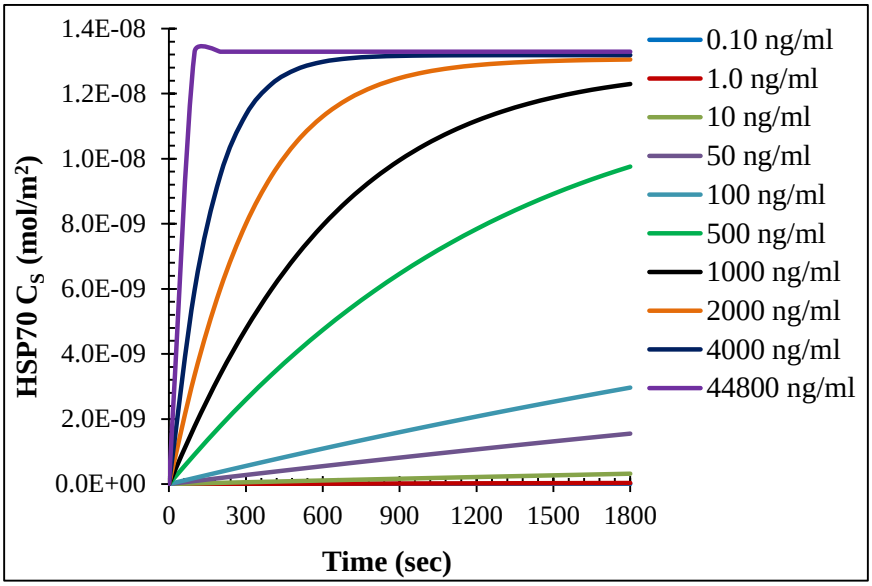

Figure 13. Simulated binding of HSP70 to a sensor of 100µmx100µm in a microchannel with a height of 100µm and a width of 100µm, for a range of concentrations.

The results from all of the simulations are summarized in Figure 14 below, which shows the surface concentration for each inlet concentration after 30 minutes. For comparison, two sets of plots were made. The first set has three plots, one for each set of lengths. The second set also has three plots, one for each set of heights. For all of the results, a similar Langmuir isotherm trend can be seen. Examining the effect of the microchannel height on the surface concentration, it was found that the higher the channel the lower the density of bound protein. This was found to be true for each of the different sensor lengths tested. This is especially evident for the 1000µm height. This is likely because a lower inlet flow rate is used for larger heights in order to keep the volumetric flow rate consistent, which results in the kinetics moving from reaction limited to diffusion limited. This is similar to what has been reported in [**129**]. Therefore, it is recommended that a channel height between 10µm and 100µm be used in order to use a higher flow rate and remain in the reaction limited regime to produce higher protein binding densities. A channel height of 100µm is potentially more beneficial than 10µm because it reduces the chances of the

channel becoming clogged and has only slightly lower protein binding densities. Therefore, 100µm is the recommended optimal channel height.

Examining the effect of the sensor array length, it was found that the smaller the array size the higher the protein binding density. This again may be in part due to the lower inlet velocity associated with larger sensor array sizes (since the width of the channel is the same as the sensor length). However, having a smaller sensor area means fewer sites to fill in the same amount of reaction time, so higher protein binding densities could be expected because of this. In other simulations (results not shown), the inlet velocity was kept the same and different sensor sizes were tested, and it was found that smaller areas did still result in higher binding densities, even with constant inlet velocities. Therefore, it would appear that the optimal sensor size would be 10µm. However, the smaller the sensor size, the weaker the LSPR signal and the higher the noise. To maintain a sufficiently strong signal, the spot size of the light would need to be comparable to 10µm, which is not simple to do in a low cost, compact device. Therefore, a sensor size of 100µm is recommended as a compromise between signal strength and protein binding density.

Overall, from the COMSOL simulations the optimal microchannel geometry was determined to be 100µmx100µm with a sensor array of 100µmx100µm. Compared to the worst design case (1000µmx1000µm microchannel with 1000µmx1000µm sensor array), the optimal design represents an increase in protein surface concentration of approximately 500% for low concentrations (0.10-100ng/ml). This concentration range covers the typical biological concentration of HSP70, so increasing the protein density in this range will significantly improve biosensor performance.

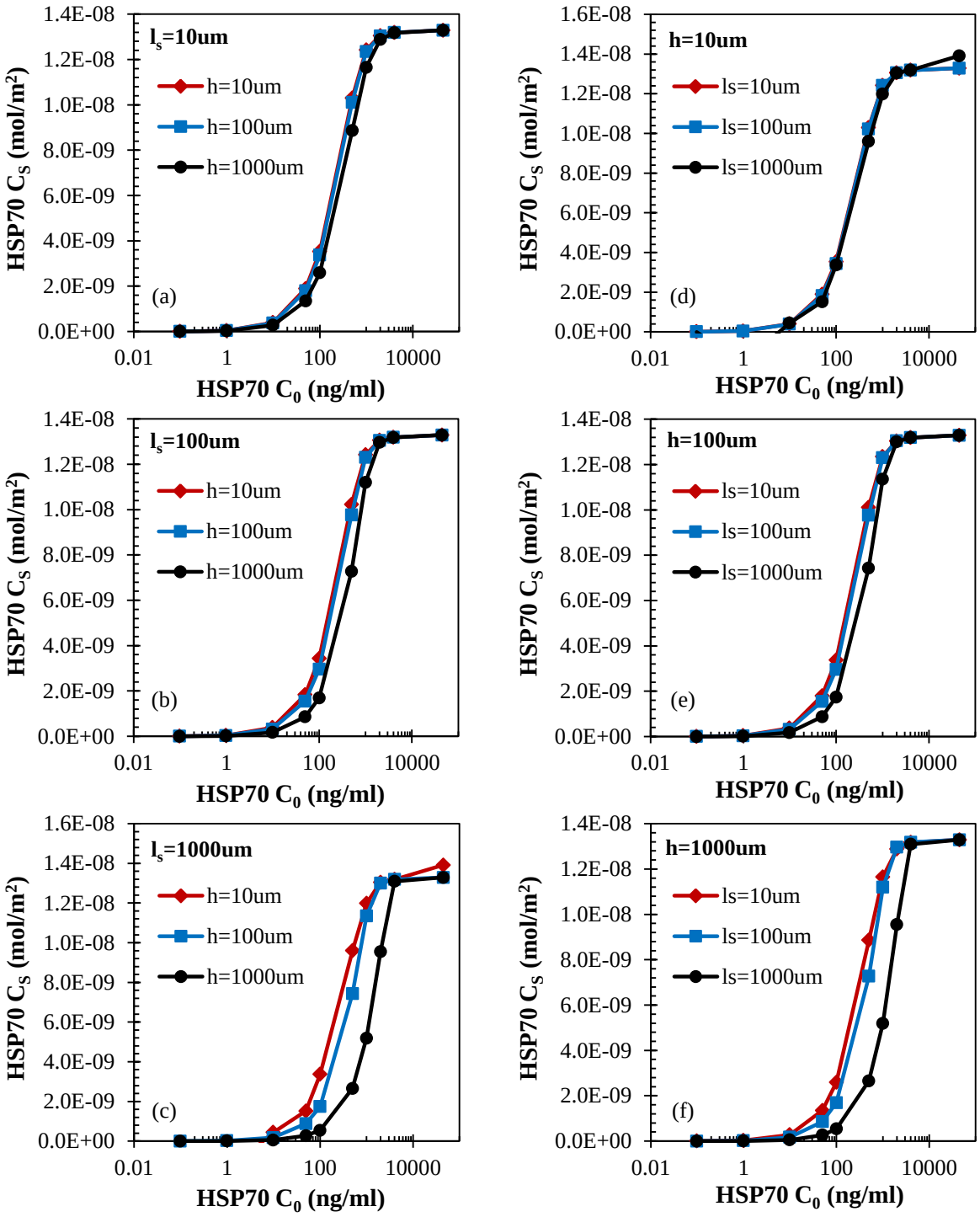

Figure 14. Summary of HSP70 surface density results from COMSOL simulations. Results are shown over a range of bulk inlet concentrations for 30 minutes at a constant volumetric flow rate of 3.33µl/min. Results in (a), (b), and (c) show the effect of the channel height (10, 100 and 1000µm) for three sensor array length (10, 100 and 1000µm). Results in (d), (e), and (f) show the effect of the sensor array length (10, 100, and 1000µm) for three heights (10, 100 and 1000µm).

3.4 Sensor Response Model

The sensor response model takes the protein surface density results from COMSOL and combines them with the nanoparticle properties determined by CST to give a complete model of the LSPR biosensor.

3.4.1 Model Construction

This model uses a MATLAB code to calculate the shift in LSPR peak position for a given protein surface concentration as determined by the COMSOL models. Also input to the model are the nanoparticle properties, including the sensitivity and decay length (determined by CST MWS), as well as the thickness of the protein and capture layers, which are estimated from literature.

The integration of the COMSOL and CST MWS results is accomplished through the use of de Feijter's equation [**131**]. This equation converts the surface concentration of the protein layer into a layer of the same thickness with an effective refractive index:

$$n_{protein} = n_{bg} + \frac{\alpha c_{s,a} M_{protein}}{d_{protein}} \tag{19}$$

The equation assumes a linear relationship between the refractive index of a protein layer and the concentration of bound proteins within that layer. Here, α is the refractive index increment of the protein, which has previously been found to be $1.8 \times 10^{-7} m^3/g$ for a number of proteins [**131**]; $M_{protein}$ is the molecular mass of the protein; $d_{protein}$ is the thickness of the protein layer; $c_{s,a}$ is the surface density of the bound protein, determined from COMSOL; and n_{bg} is the refractive index of the surrounding fluid (1.33 in this case). Ideally, the refractive index increment and the protein layer thickness would be determined for this specific protein system; however, time did not permit. For HSP70, $M_{protein}$ is equal to 70,000g/mol, and the protein thickness is estimated to be 4nm based on similar IgG proteins adsorbed on alkanethiol gold surface [**79**], [**125**].

The refractive index of the protein layer, as well as its thickness, is used in equation (5) to estimate the shift in peak position. The sensitivity and decay length are input from the CST MWS results. The capture layer thickness is estimated at 5.57nm, based on the thickness of the SAM layer and the anti-HSP70. Using these values in equation (5), the peak shift can be easily calculated for each surface concentration, which is related to the bulk concentration through the COMSOL models. Therefore, the output of the simulation is a plot of peak shift vs. bulk protein concentration.

The model also fits the Langmuir isotherm (equation (1)) to the resulting peak shift vs. bulk concentration data. Using a MATLAB least squares curve fitting function (lsqcurvefit) the dissociation constant (K_d) and the maximum peak shift (R_{max}) are determined. Using these constants in the Langmuir isotherm equation gives the complete transfer function for the sensor and thus allows prediction of the sensor performance. In particular, the LOD and sensitivity can be determined based on a given noise level, which we have found experimentally to be around 0.005-0.015nm over a 30 minute period.

3.4.2 Optimal Sensor Results and Discussion

The protein surface density found from the optimal microchannel geometry of 100μmx100μm and sensor array of 100μmx100μm was used. The values of the protein surface density for each bulk HSP70 concentration are summarized in Table 8. The optimal nanoparticle geometry of a 50nmx5nm gold nanotriangle with a sensitivity of 489.8nm/RIU and decay length of 6.952nm was used to determine the LSPR peak shifts (R) for each HSP70 bulk concentration, which are summarized in Table 8.

Table 8. Summary of the simulated LSPR peak shifts for the optimal HSP70 sensor. The HSP70 binding density is shown for each concentration, along with the calculated LSPR peak shift.

c_0 (ng/ml)	$c_{s,a}$ (mol/m^2)	R (nm)
0.10	3.21×10^{-12}	9.724×10^{-4}
1.0	3.21×10^{-11}	9.724×10^{-3}
10	3.18×10^{-10}	9.633×10^{-2}
50	1.55×10^{-9}	4.696×10^{-1}
100	2.96×10^{-9}	8.967×10^{-1}
500	9.76×10^{-8}	2.957
1000	1.23×10^{-8}	3.726
2000	1.30×10^{-8}	3.938
4000	1.32×10^{-8}	3.999
44800	1.33×10^{-8}	4.029

The simulated response of the HSP70 sensor is plotted in Figure 15. Fitting the Langmuir isotherm to the results give a K_d of 3.78nM, K_a of 2.64×10^8 M^{-1}, and an R_{max} of 4.32nm. This gives the following transfer function for the HSP70 sensor:

$$R = \frac{R_{max} * [HSP70]}{K_D + [HSP70]} = \frac{4.32nm * [HSP70]}{3.78nM + [HSP70]} \quad (20)$$

Using this response data and assuming noise of 5pm, the sensor has a LOD of 0.92ng/ml. It can operate over the range 0.92ng/ml to 4000ng/ml. The sensitivity over the range 1-50ng/ml is an average of 0.014nm/ng/ml, which given the noise of 5pm, gives a resolution of 1.1ng/ml. Comparing these values to the specifications required, the proposed LSPR HSP70 sensor satisfies all of the major design requirements.

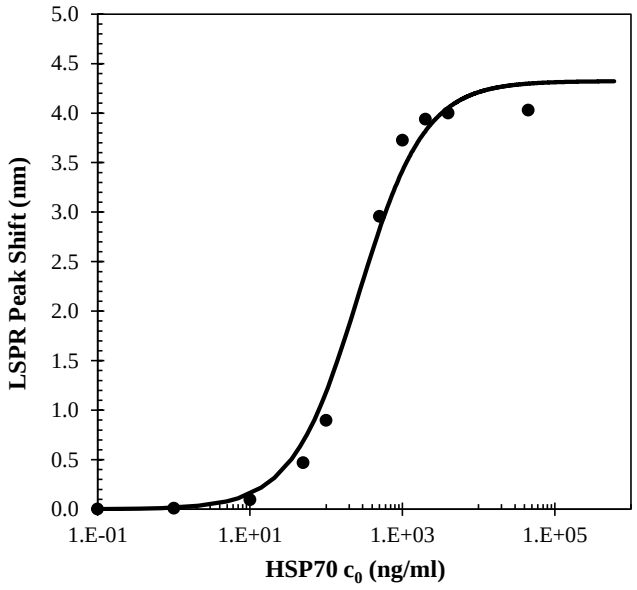

Figure 15. Simulated response of the optimal HSP70 LSPR sensor design to various inlet concentrations of HSP70. The solid line is the calculated value of R using equation (1).

Chapter 4
Experimental Implementation: Proof of Concept

The modeling and simulation results from Chapter 3 showed that the optimal LSPR design will meet the design requirements for the HSP70 sensor. Here, a proof of concept device was built to experimentally demonstrate and test the sensing principle. This was done concurrently with the simulation work, so the sensor design used here is not the optimal one. A benchtop LSPR sensor was built using gold nanoparticles fabricated by EBL and a custom made PDMS flow cell. The nanoparticles were characterized for size and shape using scanning electron microscopy (SEM) and atomic force microscopy (AFM), and the optical properties, bulk sensitivity, and decay length determined. A surface functionalization procedure was developed using alkanethiol SAMs for testing the LSPR sensor. The proof of concept was characterized using the well-known biotin-streptavidin system. It was also tested using purified salmon HSP70 and its antibody to demonstrate operation with the target protein. A sensor cleaning procedure using UV-ozone and a regeneration protocol using an acidic glycine buffer were also developed.

4.1 Materials and Methods

In this section, the materials and methods used to build and test a proof of concept LSPR sensor are outlined. The nanoparticle fabrication process and the morphological and optical characterization methods are detailed. The experiment test setup and procedures used to evaluate the LSPR sensor's performance for two different protein systems is described. The surface functionalization method used to implement a specific capture layer for each protein system is also detailed.

4.1.1 Nanoparticle Fabrication and Characterization

The size and shape of the nanoparticles used in the proof of concept device were chosen prior to completion of the simulations in order to allow for parallel development of the model and experimental setup. Therefore, the nanoparticles used do not represent the optimal design, and were instead chosen for ease of fabrication, but optimal geometries will be tested in the future. Square gold nanoparticles were fabricated using a lift-off process with patterns generated by EBL. The fabrication process was performed by the University of Western Ontario (UWO) Nanofabrication Facility using a LEO 1530 field emission scanning electron microscopy (FESEM). Particles were designed as 100nmx100nmx50nm and laid out as an array with a periodicity of 300nm (edge to edge spacing of 200nm). A thin layer of chrome (1-2nm) was used as an adhesion layer, followed by 50nm of gold. The nanoparticle array covered an area of

1mmx1mm, centered on a 10mmx10mm glass chip diced from 500µm thick Pyrex wafers, which is shown in Figure 16.

SEM images were taken using a 1540XB from LEO (UWO) and processed using ImageJ software (publicly available from rsbweb.nih.gov/ij). AFM images were obtained using a Veeco Dimension 3100 in tapping mode with silicon tips from NanoDevices. The tips had a radius of approximately 10nm, a resonance frequency of 300 kHz, a spring constant of 40N/m, and a Q factor of 300. Images were processed using Gwyddion software (publicly available from gwyddion.net).

The bulk refractive index sensitivity (RIS) of the Au NPs was determined by using various water-glycerol solutions (0, 10, 20, 30, 40, 50, and 60%) inside the flow cell and measuring the peak position for each solution. The refractive index of each solution was estimated by using the relationship between weight percentage of glycerol in water and refractive index reported in [**132**]. The decay length was determined using a process similar to that reported in [**81**], in which alternating polyelectrolyte layers of nanometer thickness were formed on the surface of the nanoparticles, a procedure known as layer-by-layer assembly. The polyelectrolytes, purchased from Sigma Aldrich, were poly(allylamine hydrochloride (PAH), which is positively charged, and poly(sodium 4-styrenesulfonate) (PSS), which is negatively charged. The peak position was measured after each layer was formed, up to a thickness of about 50nm, which was 25 bilayers of PSS/PAH. The thickness of each layer was determined through ellipsometry (M-44, J.A. Woollam Co) in separate experiments. Equation (8) was fit to the peak shift data using a least squares regression to determine the decay length. The sensitivity could also be determined from this data and was used as a secondary measurement. The detailed procedure and the results from ellipsometry characterization can be found in Appendix A.

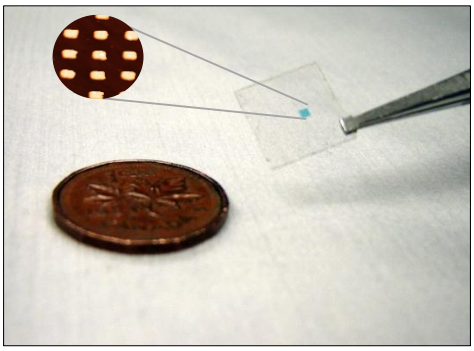

Figure 16. Photograph of the glass chip containing a 1mmx1mm gold NP array. Circular inset shows an AFM image of the array.

4.1.2 Experimental Test Setup

The experimental test setup consisted of four main components: the optical setup, a laptop, the flow injection analysis system, and the flow cell. The entire setup is shown in Figure 17.

The optical setup was used to measure the absorbance spectrum of the nanoparticles and track the LSPR peak position in real time. It consisted of an ultraviolet-visible (UV-Vis) spectroscopy system, made up of an LS-1 white light source and a USB4000 spectrometer, both from Ocean Optics. Measurements were taken in transmission mode using two fiber optic cable patch cord assemblies (P600-1-SR) and collimating lenses (74-UV) mounted on an adjustable collimating lens holder (74-ACH), all from Ocean Optics. Light was unpolarized and the beam spot size was approximately 4mm in diameter. Reference spectra were taken in air. All measurements were taken at room temperature in air.

A laptop with SpectraSuite software (Ocean Optics) was used to acquire the data from the spectrometer via USB. The LSPR peak position was tracked in real time using a custom MATLAB program (see Appendix B), which analyzed the incoming spectra to determine the peak position using the "findpeaks" code (publicly available from terpconnect.umd.edu/~toh/spectrum/PeakFindingandMeasurement.htm). A moving average of 50 was employed to reduce the noise in the acquired signal.

A flow injection analysis (FIA) system was designed and built to allow a continuous flow of carrier fluid over the sensor and bubble free injection of samples to the sensor. A Pump 11 Pico Plus syringe pump (Harvard Apparatus) was used to pump carrier fluid at a constant rate from a 5mL syringe into a six port, two position selector valve (C22Z, CSI) via PEEK tubing (1/16'' OD 0.03''ID). Carrier fluid was a 13mM phosphate buffered saline (PBS) at pH 7.4. The outlet of the valve was connected to the inlet of the PDMS flow cell that contained the sensor chip. The outlet of the flow cell led to a waste container. On the injection valve, a PEEK sample loop was attached (1/16'' OD, 0.55'' ID), with a length corresponding to the desired volume of sample. The sample was loaded into the sample loop via a syringe through a fill port (VCVISF1, CSI), and injected into the flowing stream of carrier fluid by manually switching the valve position.

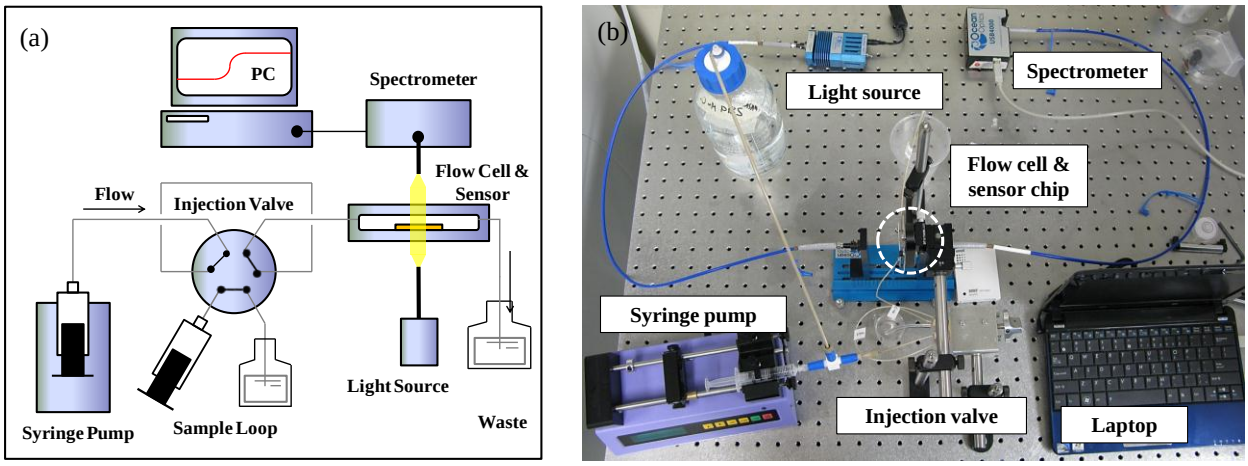

Figure 17. (a) Schematic diagram showing the various parts of the benchtop prototype, including the FIA system, the flow cell and sensor chip, the UV-Vis spectroscopy system and the laptop. (b) Photograph of the actual benchtop LSPR sensor prototype. The white dashed circle indicates the sensor and flow cell location.

The nanoparticle chip was housed inside of a flow cell chip assembly, shown in Figure 18, made of a PDMS chamber (Sylgard 184, Dow Corning). An aluminum mold made by CNC machining (Figure 18a) was used to cast the PDMS and create the flow cell chamber (Figure 18b) using an in-house procedure (see Appendix C). The chamber was designed with a horizontal inlet and outlet for 1/16'' PEEK™ tubing. The volume of the chamber was approximately 0.1ml. The height of the chamber was 2.5mm and the width 4mm, giving a cross sectional area of 10mm^2. Although these are not the optimal dimensions as determined from the fluidic simulations, they were chosen for ease of fabrication and testing, and in the future optimal flow cells will be fabricated and used. The whole flow cell assembly, shown in Figure 18c, consisted of three layers: the bottom layer, which was the nanoparticle chip, the middle layer, which was the PDMS chamber, and the top layer, which was a glass microscope slide. The entire device was held in place using two aluminum plates as a clamp. The plates had viewports to allow for light to pass through. The flow cell assembly was mounted to a D12 xyz stage (Thor Labs) so that the center of the nanoparticle chip could be aligned with the center of the light beam passing through it, as shown in Figure 18d. The flow cell was always mounted vertically with the inlet at the bottom in order to prevent bubble formation/trapping inside the flow cell.

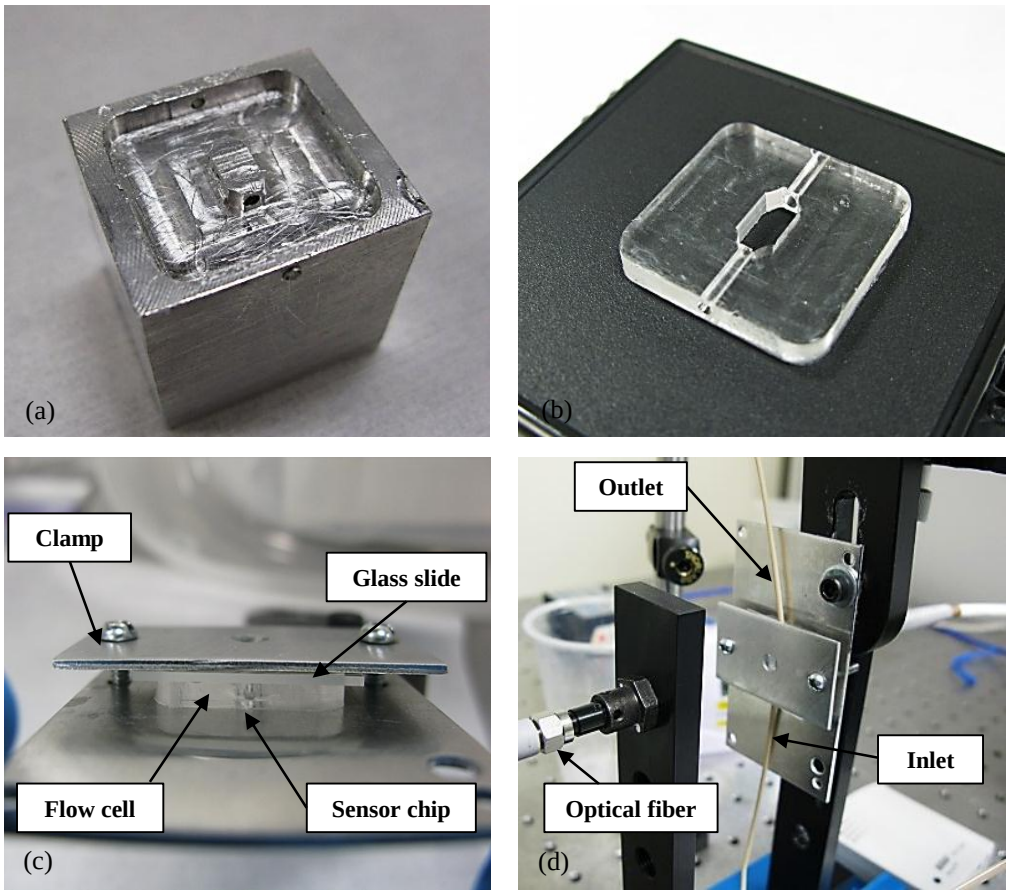

Figure 18. (a) Aluminum mold used to cast PDMS to fabricate the flow cell. (b) PDMS flow cell made using the molding process. (c) Flow cell assembly showing the top glass slide layer, the middle PDMS layer, and the bottom sensor chip layer. The aluminum clamp holds all three layers together. (d) The flow cell assembly mounted in the experimental setup, showing the fluid inlet and outlet and the optical fiber through which light is brought to the chip.

4.1.3 Surface Functionalization and LSPR Sensing Procedure

As mentioned, two different proteins were detected using the proof of concept LSPR sensor. Streptavidin was detected via biotin and HSP70 via anti-HSP70. The functionalization steps for each procedure are detailed in Figure 19 for SA and Figure 20 for HSP70. The initial steps (i-iii) of the functionalization procedure are the same for each system, yet some differences are present in the test procedures in steps (iv) and (v). The functionalization procedure is based on an optimization study done with a quartz crystal microbalance (QCM), the details of which can be found in [**133**]. The study was done using HSP70 and it antibody on gold coated quartz chips.

The first step in the functionalization process was to clean the nanoparticle chips. This was done using a combination of UV-Ozone cleaning (PSD PRO UV-4T, Novascan) and washing with solvents. The full

cleaning procedure can be found in Appendix D. The cleaning protocol was developed and analyzed with x-ray photoelectron spectroscopy (XPS) (data available in Appendix D), which showed it was successful at completely regenerating the gold surface after it had been coated with the functionalization layers. This allowed reuse of the chip for over 50 times without significant degradation.

After the chip had been cleaned, it was placed in a beaker of ethanol containing a 3:1 ratio of 11-mercaptoundecanoic acid (11-MUA):1-octantiol (1-OT) (Sigma Aldrich) at a concentration of 10mM. After 20 minutes of incubation, a mixed layer of alkanethiol molecules was formed on the gold nanoparticle surface. The chip was then removed and rinsed thoroughly with ethanol, followed by deionized (DI) water. Next, the carboxyl head groups of the 11-MUA were modified using carbodiimide hydrochloride (EDC) and N-hydroxysuccinimide (NHS) (Fisher Scientific). This was done by placing the chip into a beaker of 5mM EDC/NHS and leaving it to incubate for 60 minutes. Afterwards, the chip was rinsed in DI water and dried with nitrogen gas and was loaded into the flow cell assembly. The light beam was aligned and data acquisition of the peak position in real time was started. Up to this point, the functionalization procedure is the same for both streptavidin and HSP70 detection. The following sections outline the individual protocols for each biomolecule.

4.1.3.1 Biotin-Streptavidin

The syringe pump was loaded with 13mM PBS buffer and started at a flow rate of 0.200ml/min to fill the flow cell and later set to 0.010ml/min to obtain a stable baseline signal. Biotin functionalized with a polyethylene glycol (PEG) spacer arm and a terminal primary amine (EZ-Link Amine-PEG3-Biotin, Thermo Scientific) was diluted to 1mM in PBS buffer at a pH of 6.5, the optimal pH for the binding of biotin to the 11-MUA. Using a 500µL sample loop, 500µL of biotin was injected into the flowing stream of carrier solution and allowed to bind to the head groups of the 11-MUA. The binding process was monitored in real time and occurred for 50 minutes with the given flow rate and volume. The pump speed was then set to 0.1ml/min to flush out the system for 30 minutes, and then set back to 0.010ml/min to get a stable baseline. Streptavidin was purchased from Invitrogen and diluted to various concentrations in PBS buffer at a pH of 7.4. The 500µL sample loop was rinsed thoroughly, and 500µL of the streptavidin solution was loaded into it and injected into the carrier solution. The binding was monitored in real time and occurred for 50 minutes. The LSPR response was measured over a SA concentration range of 10-500,000 ng/mL (0.1- 8333 nM). Three trials were carried out for each of six of the concentrations tested. Only one trial was completed for the highest SA concentration (500,000 ng/ml), as it required a very large amount of sample. Afterwards, the system was flushed again and eventually disassembled to prepare for

the next test. The test can only be performed once before the chip is cleaned via the UV-ozone procedure, as the biotin-streptavidin interaction is not reversible.

Specificity testing was also performed using the biotin-streptavidin system. Bovine serum albumin (BSA) from Fisher Scientific was diluted in 13mM PBS (pH=7.4) to a concentration of 1% (1.5mM or 10mg/ml). BSA was injected (500µL, 0.010ml/min) at various stages of the functionalization process to examine the effect of a non-specific protein. This will be discussed further in Section 4.3.2.

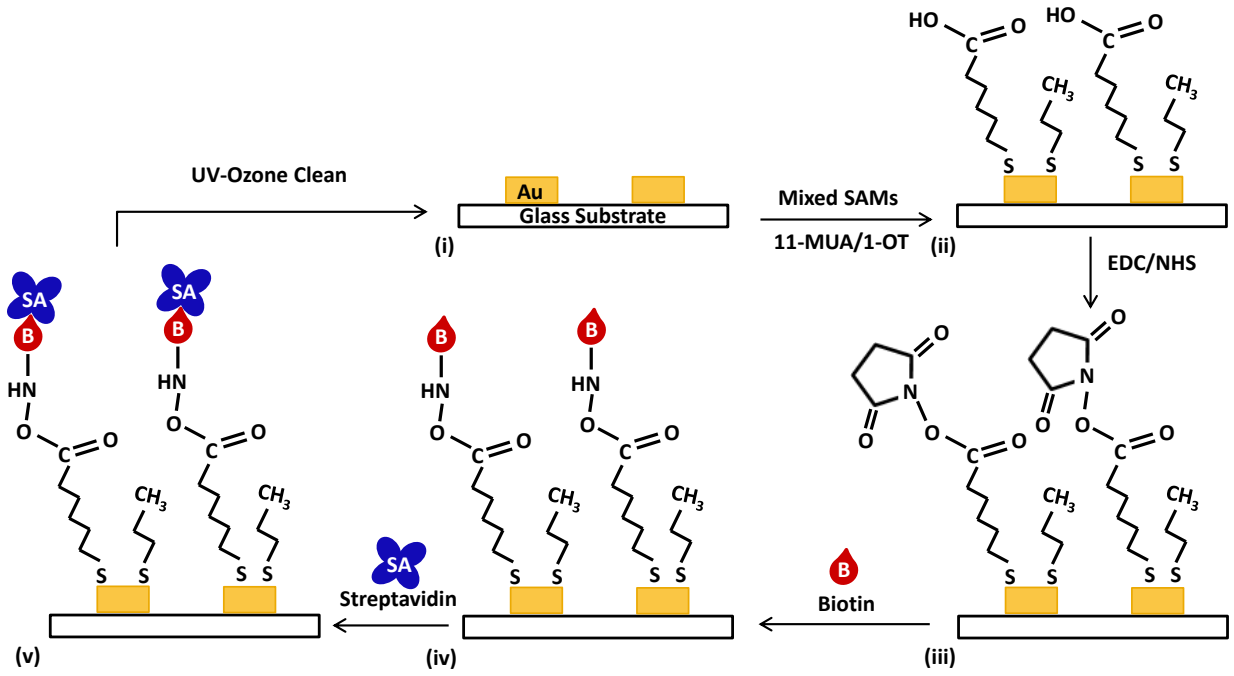

Figure 19. Schematic of the surface functionalization process for specific capture of streptavidin using biotin. (i) The NP chip is cleaned using a UV-ozone procedure. (ii) The chip is incubated in a solution of 11-MUA/1-OT to form a SAM on the gold NP surface. (iii) The 11-MUA head groups are modified using an incubation in EDC/NHS. (iv) The chip is loaded into the flow cell assembly, and amine-modified biotin is injected, which reacts with the modified 11-MUA and binds to the surface. (v) SA is injected and binds to the NP surface through the biotin molecule.

4.1.3.2 HSP70 and Anti-HSP70

The syringe pump was loaded with 13mM PBS buffer and started at a flow rate of 0.200ml/min to fill the flow cell and later set to 0.005ml/min to obtain a stable baseline signal. Synthetic salmon HSP70 antibody was purchased from StressMarq Biosciences and diluted ~1:1000 to a concentration of 1µg/ml in 13mM PBS buffer at pH=7.4. Using a 1000µL sample loop, 1000µL of anti-HSP70 was injected into the flowing stream of carrier solution and allowed to bind to the head groups of the 11-MUA. The binding

process was monitored in real time and occurred for 200 minutes with the given flow rate and volume. Note that a longer incubation time was used here as recommended by those experienced in HSP70 functionalization procedures. The system was then left overnight and was flushed with PBS buffer. The following day, salmon HSP70 (Assay Designs/Enzo Life Sciences) was diluted in 13mM PBS buffer (pH=7.4) to a concentration of 4.6µg/ml (69nM). Using the 1000µL sample loop, 1000µL of protein was injected into the system at 0.005ml/min and allowed to bind to the anti-HSP70 capture layer. The binding was monitored in real time and occurred for 200 minutes. Afterwards, the system was flushed with PBS, and either disassembled for the next test or regenerated. The nature of the HSP70 antibody-antigen interaction allows the protein to be unbound from the antibody using an appropriate regeneration buffer. The buffer used here was a 100mM glycine-hydrochloric acid buffer with pH=2.0. 1000µL was injected at a flow rate of 0.020ml/min, allowing for 50 minutes of reaction time. The system was flushed with PBS and a second HSP70 binding test could be performed. After the testing was complete, the surface was completely cleaned and regenerated via the UV-ozone cleaning procedure.

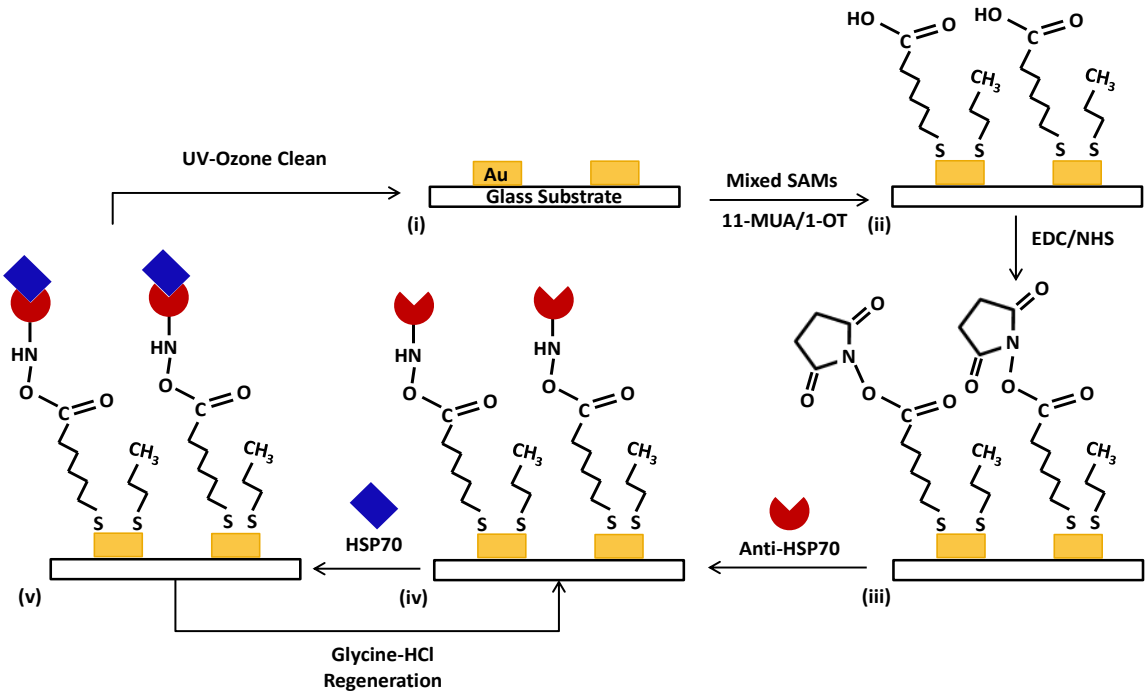

Figure 20. Schematic of the surface functionalization process for specific capture of HSP70 using anti-HSP70. (i) The NP chip is cleaned using a UV-ozone procedure. (ii) The chip is incubated in a solution of 11-MUA/1-OT to form a SAM on the gold NP surface. (iii) The 11-MUA head groups are modified using an incubation in EDC/NHS. (iv) The chip is loaded into the flow cell assembly, and anti-HSP70 is injected, reacting with the modified 11-MUA and binding to the surface. (v) HSP70 is injected and binds to the NP surface through the anti-HSP70 molecule.

4.2 Fabrication and Characterization Results and Discussion

In this section, the results of the morphological and optical characterization of the fabricated nanoparticles are described. The size and shape of the nanoparticles are determined, along with the LSPR peak properties. The LSPR bulk sensitivity and decay length of the nanoparticles are also determined and discussed.

4.2.1 Morphological Characterization

Gold nanoparticles of 50nmx100nmx100nm were fabricated on glass substrates using electron beam lithography (EBL). Optical images of the nanoparticle array show large scale uniformity with few defects over the entire 1mmx1mm pattern (Figure 21a). Nanoparticles were characterized for their size, shape, and quality using scanning electron microscopy (SEM) and atomic force microscopy (AFM). SEM images (Figure 21b) confirm that the lateral dimensions of the NPs are very close to their designed values, with average lateral dimensions of 101.4nmx102.5nm (+/-4.8nm) and periodicity of 302.0nm (+/-6.7nm). From these images it is also clear that the corners are slightly rounded, due to the resolution limits of EBL, but overall the nanoparticles are highly uniform and square in shape. Characterization of the NP height by AFM (Figure 21c, d) reveals an average height of 57.1nm (+/-1.80nm), which is slightly larger than the expected 52nm height (2nm of chromium was used for adhesion).

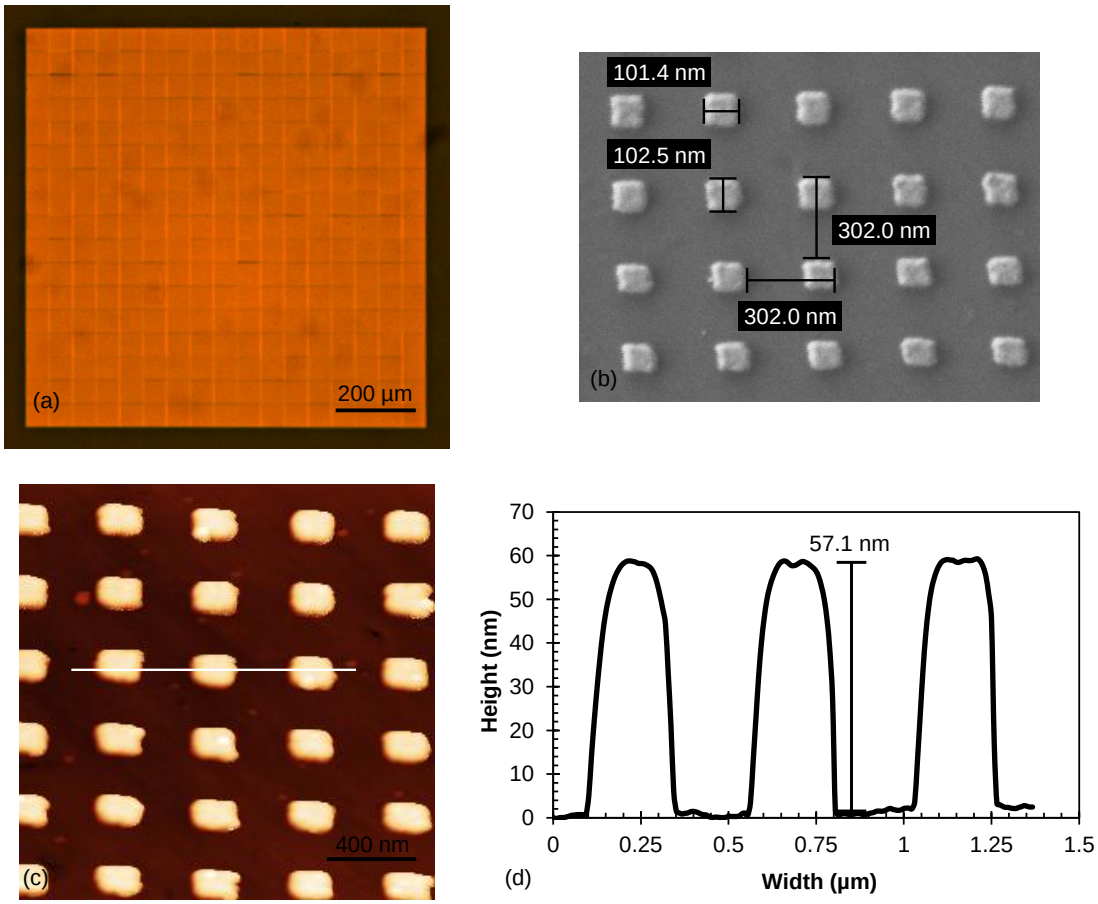

Figure 21. (a) Optical microscope image of the 1mmx1mm array of Au nanoparticles on glass, fabricated by EBL, showing high uniformity. (b) SEM image of Au nanoparticle array. The lateral dimensions and periodicity of the nanoparticles agree well with the designed dimensions. (c) Raw AFM image (no post-processing) and (d) AFM line profile of the Au nanoparticle array. The height of the nanoparticles is slightly larger than expected, at an average of 57.1nm. Please note that lateral dimensions are inaccurate and do not correspond to those found from SEM images due to AFM tip broadening and instrument drift.

4.2.2 Optical Characterization: Sensitivity and Decay Length

The optical properties of the Au NPs were determined using the UV-Vis spectroscopy system in transmission mode. The LSPR peak is located at 591.3nm (+/-0.1nm) in air, with a height of 0.048 OD, and full width half maximum (FWHM) of 85.0nm (Figure 22a). In water, the peak red shifts to 635.0nm (+/-0.1nm), as is evident in Figure 22a. The bulk refractive index sensitivity (RIS) of the Au NPs is 159.26nm/RIU +/- 2.78nm/RIU (Figure 22b, c). This was determined by using various water-glycerol solutions (0, 10, 20, 30, 40, 50, and 60%) inside the flow cell and measuring the peak position for each solution. When compared to similar structures reported by other researchers, this RIS value is close to the

typical value of 200nm/RIU [**46**], [**134**], [**89**]. This gives an overall LSPR figure of merit (FOM = RIS/FWHM) of 1.87 for these gold NPs, which is similar to many other NPs that are often around 2.0 [**46**]. The decay length was determined to be 19.8nm +/-0.29nm (Figure 22d) through the use of polyelectrolyte multilayer coatings. This is similar to other gold nanoparticles of comparable dimensions [**81**], which were found to have decay lengths from 19-24nm. From the analysis in Chapter 3, this decay length is far from the optimal decay length for HSP70 detection, which is 6.731nm. The sensitivity determined using this technique was 157.5nm/RIU, which is very similar to the sensitivity found using the glycerol-water solutions.

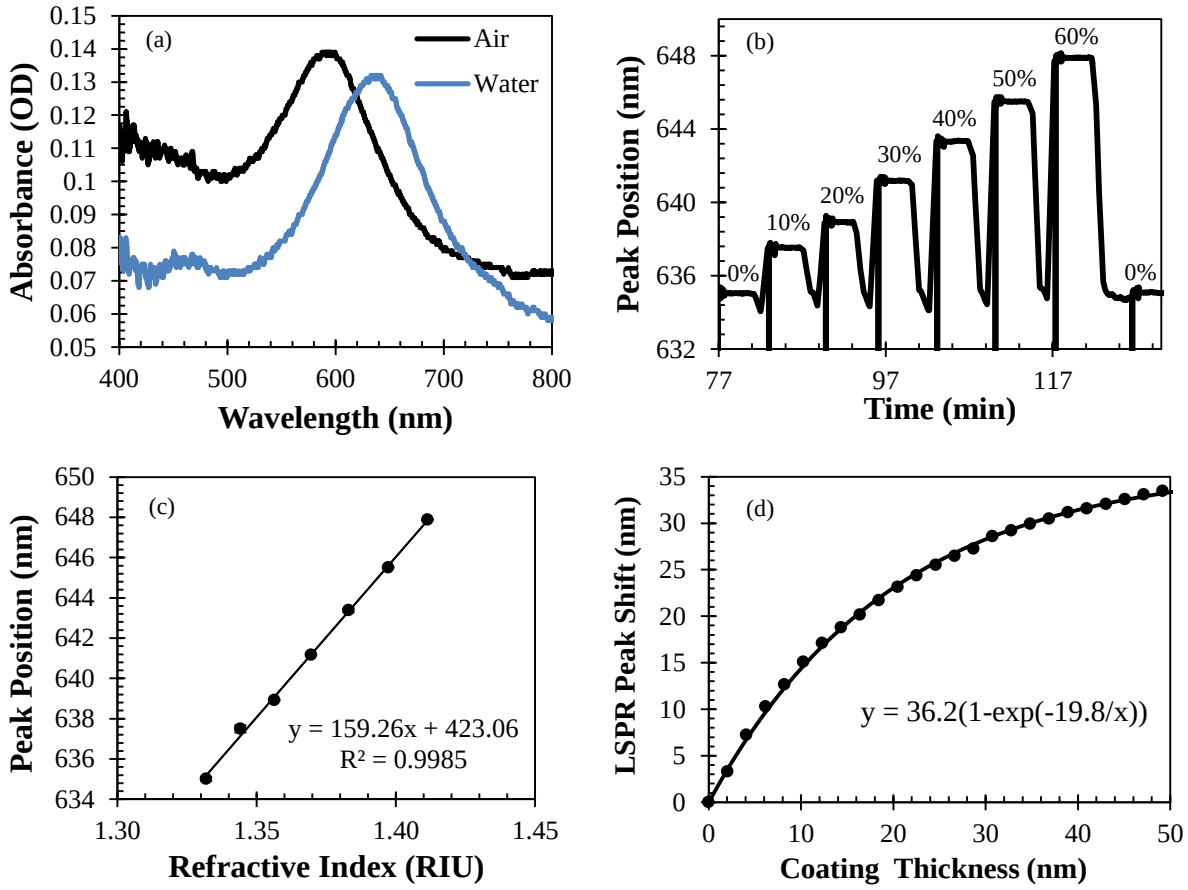

Figure 22. (a) Typical spectra obtained with UV-Vis spectroscopy system in transmission mode of square Au nanoparticle arrays in air and in water. The LSPR peak is visible at 591.3nm (+/-0.1nm) in air and 635.0 (+/-0.1nm) in water. (b) Real time LSPR peak shift induced by solutions of different RI made of water and glycerol. (c) Sensitivity of the LSPR peak position to changes in the bulk refractive index. The RIS was found to be 159.26 nm/RIU by using linear regression. Error bars indicate one standard deviation above and below the average, taken from four independent measurements. (d) Shift in LSPR peak position due to formation of polyelectrolyte multilayers for determination of decay length. The decay length was found to be 19.8nm +/-0.29nm.

4.3 Biotin-Streptavidin Results and Discussion

In this section, the results of testing the LSPR sensor using the biotin–streptavidin system are outlined. The dynamic range, LOD and repeatability are described, and a detailed analysis of the non-specific binding and specificity of the sensor is given.

4.3.1 Dynamic Range, LOD, and Repeatability

The LSPR peak position was monitored in real time during the binding of biotin to the surface of the nanoparticles via the 11-MUA SAM. The formation of this capture layer allowed subsequent detection of the streptavidin protein. An example result of the sensor response for biotin binding and streptavidin detection for a concentration of 4.15µg/ml (69nM) is shown below in Figure 23. In this case, the binding of biotin results in a peak shift of 0.70nm, with a very small drop in peak position after the biotin has exited the flow cell. This is likely due to the removal of some non-specifically bound biotin as well as a small refractive index different between the carrier solution and biotin sample. After flushing the system, the binding of streptavidin to the sensor surface results in a large peak shift of 2.9nm. Minimal reverse binding is seen, which is expected due to the very strong bond between biotin and streptavidin.

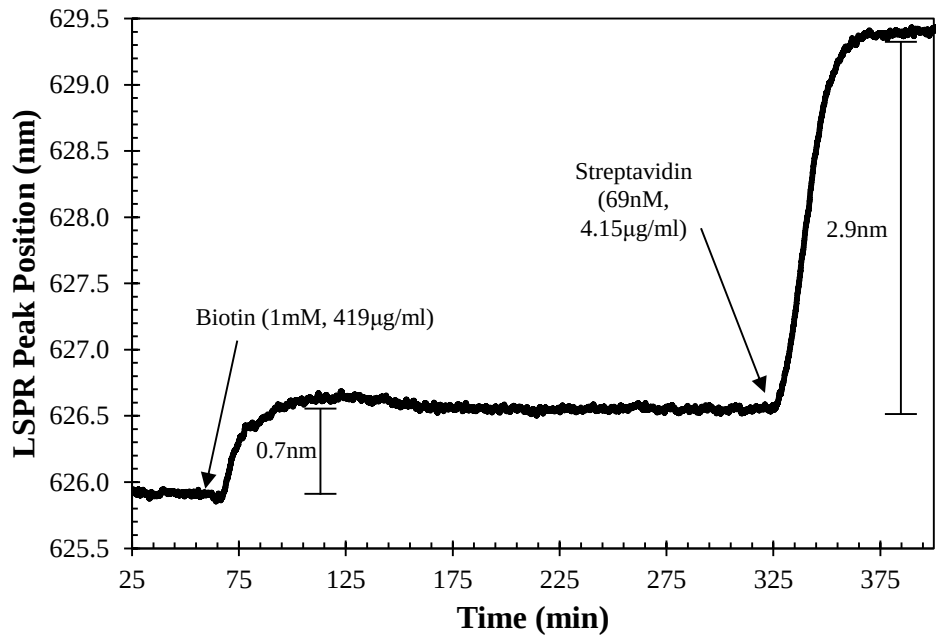

Figure 23. Real time LSPR sensor response for SA detection. (i) First, the surface is functionalized for selective capture of SA by binding of biotin (1mM) to the surface of the Au NPs. (ii) After thorough washing, SA (69nM) is injected, resulting in a large peak shift due to selective binding to the biotin.

The LSPR sensor was tested for seven different SA concentrations, from 10ng/ml to 500,000 ng/ml. Each concentration was tested three times using the same procedure, except the highest concentration, which was only performed once due to the large amount of sample needed. The LSPR peak shifts from each experiment are summarized below, with the average and standard deviation for each calculated. For the smallest concentration (10ng/ml), the peak shifts an average of 0.05nm, and for the highest concentration (500,000ng/ml), the peak shifts an average of 5.53nm. These results demonstrate successful operation of the real-time LSPR immunosensor and validate its ability to detect and quantify SA. The percentage error typically lies within 10-40%, which is likely due to the variance in experimental conditions between trials. To further support this, it was found that the LSPR peak shift due to biotin binding had a variation of 27%, with an average of 0.59nm, over all the trials. This variation in biotin binding is likely due to small changes in EDC/NHS concentration and incubation times, as well as small differences in biotin concentration between trials. It is expected with more rigorously controlled procedures, this error would be greatly reduced, thus reducing the error on the SA measurements.

Table 9. Experimental results from LSPR sensor for detection of SA at various concentrations. Each concentration was repeated three times except for the highest concentration, which was only performed once.

[SA] (ng/ml)	[SA] (nM)	SA LSPR Peak Shifts (nm)				St. Dev.	% St. Dev.
		Trial 1	Trial 2	Trial 3	Average		
9.96	0.17	0.08	0.04	0.04	0.05	0.02	43.30%
99.59	1.66	0.08	0.08	0.04	0.07	0.02	34.64%
995.85	16.60	0.16	0.25	0.28	0.23	0.06	27.15%
4149.38	69.16	2.86	1.94	2.02	2.27	0.51	22.42%
9876.54	164.61	3.37	3.18	3.55	3.37	0.19	5.50%
100000.00	1666.67	5.37	4.82	4.05	4.75	0.66	13.97%
500000.00	8333.33	5.53	n/a	n/a	5.53	n/a	n/a

Using this data, a dose-response curve can be generated and fit with the Langmuir isotherm to determine the maximum peak shift, R_{max}, and the association/dissociation constant, K_a and K_d. Using MATLAB and the least squares curve fitting function, this curve is generated and shown in Figure 24, along with the experimental peak shifts and their standard error. From the fitting analysis, K_a was estimated as 9.22×10^6 M^{-1}, K_d was found to be 108.5nM, and R_{max} was found to be 5.39nm. This gives the following transfer function for the SA sensor:

$$R = \frac{R_{max} * [SA]}{K_D + [SA]} = \frac{5.39nm * [SA]}{108.5nM + [SA]} \quad (21)$$

The peak to peak wavelength shift noise of the baseline in repetitive experiments was found to be +/- 0.01nm over 1 hour, and from this the LOD for the system was determined to be 0.80nM or approximately 55ng/ml. This results in a wide dynamic detection range, from 55ng/ml to 500,000ng/ml, which is almost four orders of magnitude.

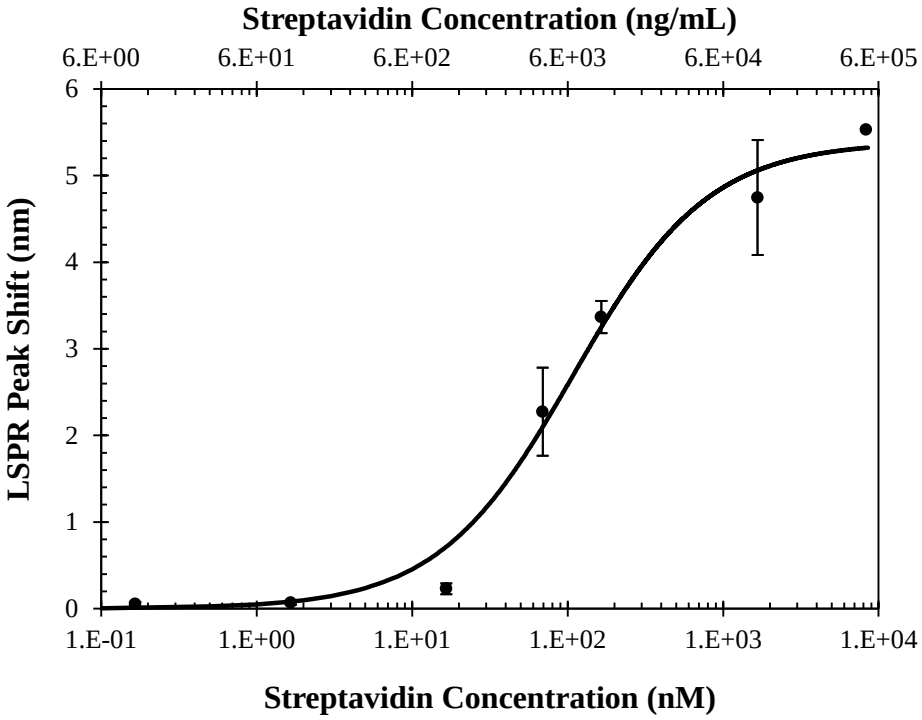

Figure 24. LSPR sensor response curve for various concentrations of SA binding to a biotinylated Au nanoparticle surface. Error bars indicate one standard deviation above and below the average, taken from three independent measurements. The solid line is the calculated value of R using equation (1).

The use of the biotin-streptavidin system for sensor characterization is useful as it allows straight forward comparison with many other studies reported in the literature. Investigating the kinetic constants, in one study using Ag nanostructured films, the K_a for the interaction of immobilized biotin and streptavidin on an LSPR sensor was estimated to be 3.0×10^6 M^{-1} [**107**], which is on the same order of magnitude as the K_a found for the LSPR sensor response curve shown above. Compared to other studies, however, these K_a values are in general low. Using Au nanocylinder sensors functionalized with a 100% 11-MUA SAM, the surface binding affinity was 6.1×10^9 M^{-1} for the binding between biotin and SA, and the LOD was

determined to be 7pM [**56**]. Better yet, using triangular Ag nanoparticles (100nm wide and 50nm high), and similar functionalization methods, a sensor was developed with a LOD less than 1pM, and a K_a found to be 10^{11} M^{-1} [**100**]. These K_a values are higher but still correspond to much smaller surface binding constants than those found for biotin-SA in solution, which are 10^{13}-10^{15} M^{-1} [**56**], [**100**], [**107**].

There have been many reports of the biotin-SA interaction by LSPR assays and detection limits range from picomolar to micromolar concentrations [**46**]. The broadly varying performance arises largely due to the variations seen in the equilibrium constants of the dose-response curves [**46**]. It is unexpected that these constants have been found to vary by that many orders of magnitude [**46**], because although experimental conditions and the noise of a system do have an impact, LOD is critically dependent on the K_a of the protein pair [**100**]. The LOD will improve for higher binding affinities and worsen for lower binding affinities [**100**]. K_a is responsible for shifting the response curve left (to lower concentrations) and right (to higher concentrations). A higher K_a will result in the response curve shifting to the left. This means that the system will reach its saturation point at lower concentrations, and in turn that the LOD will be lowered and therefore improved.

The binding constant of biotin-SA in solution would lead in principle to LODs in the femtomolar range [**46**]. It is clear however not only in this study, but in multiple other developments of LSPR biosensors, that a greatly reduced affinity is observed, and this can be attributed to the effects of the conjugation of biotin to the nanoparticle surface via a molecular tether. These effects include steric hindrance and limited mobility [**46**]. There are varying degrees of freedom for the movement of biotin molecules once immobilized onto the sensor surface and it is suggested that this restricted movement reduces the affinity for binding to SA [**107**]. If the length of the biotin arm or tether is increased, then the binding space between the biotin and SA can be enlarged and the binding constant increased [**135**]. Therefore, lengthening the biotin tether can strengthen the binding between the biotin-SA pair [**135**], and it is anticipated that the surface binding constant will approach that for the solution phase [**100**].

Overall, the LSPR biosensor was characterized to have a LOD less than 1nM, and a surface binding affinity constant in the 10^6-10^7 M^{-1} range. This value is low, but has been displayed by other studies in literature. Literature values for LOD and K_a have a large variance due to differences in biotin tether lengths, which restricts movement of immobilized biotin to varying degrees and reduces binding affinity to SA. The current LSPR sensor can detect a wide range of SA concentrations in real-time with high sensitivity. However, numerous improvements could be made to the design, through optimizing the NP

shape/size for SA detection, lengthening the biotin tether to improve binding affinity and minimizing noise in the system.

4.3.2 Selectivity and Specificity

The ability of the label-free sensor to discriminate between the target analyte and other interfering components is essential to ensuring correct results. The LSPR sensor was characterized for its specificity to streptavidin through a variety of different tests. These tests are outlined in Figure 25, the results of which will now be discussed. The first test, shown in (i), was used to determine if SA would bind to the sensor surface without the presence of biotin. A SAM was formed on the NPs with 11-MUA/1-OT in the usual manner, but no further functionalization was performed. Instead, the chip was loaded into the flow cell and SA injected at 69nM. An example of the results are shown below in Figure 26, and resulted in an LSPR shift of 0.95nm +/-0.31nm upon exposure to the SA (over 3 trials). This indicates non-specific adsorption of SA to the surface of the sensor. This indicates non-specific binding because if SA was only binding to biotin, than this test should have resulted in no change in peak position. This may not be a surprising result, as other LSPR sensors have been demonstrated to exhibit a non-specific response [**50**], [**90**], [**100**], [**136**], [**137**]. One mechanism for the non-specific binding is electrostatic binding to the surface of the SAM layer, which has been shown in literature for proteins such as IgG on CH_3 surfaces [**138**], and which likely applies to SA as well. Another mechanism is binding to exposed gold or the chrome adhesion layer, which has also been shown in literature for Ag LSPR sensors with a chrome adhesion layers [**50**]. This result indicates that even when the surface is functionalized with biotin, there is likely some level of non-specific binding of the protein to the CH_3 groups or the metal surfaces, which is the process shown in (iii). This is undesirable since complex solutions with large concentrations of background proteins will cause false positive signals due to non-specific adsorption.

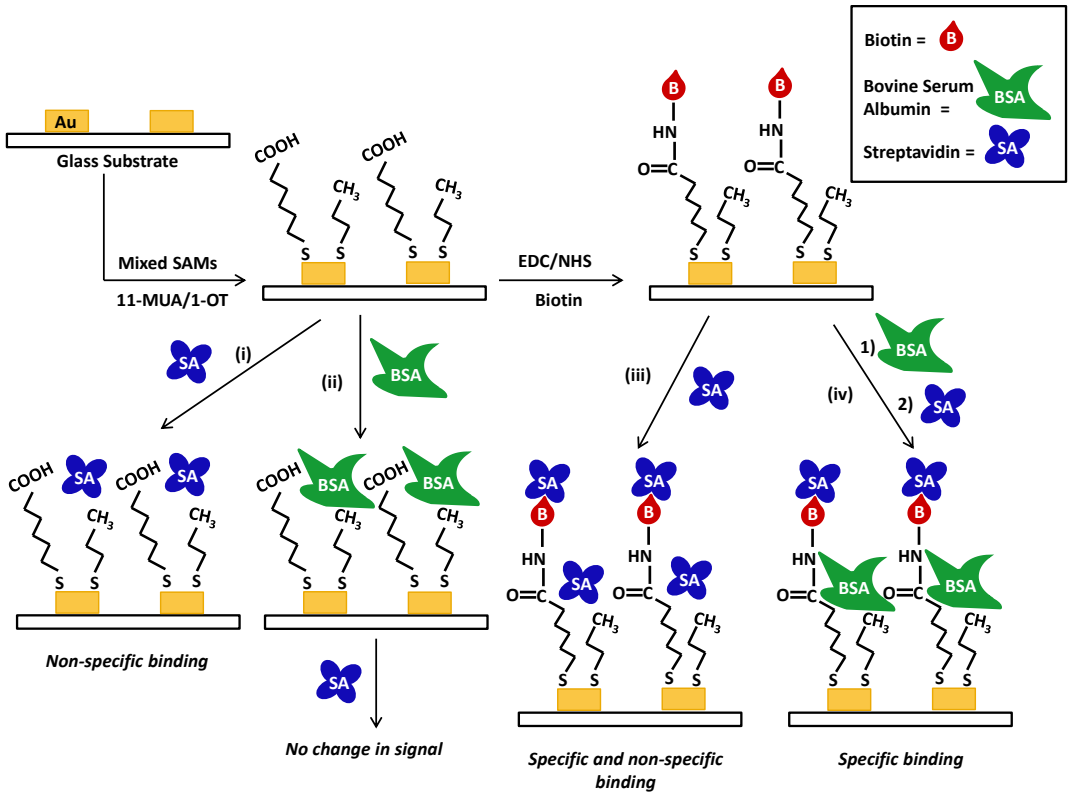

Figure 25. Illustration showing the various tests performed to examine the selectivity and specificity of the LSPR sensor.

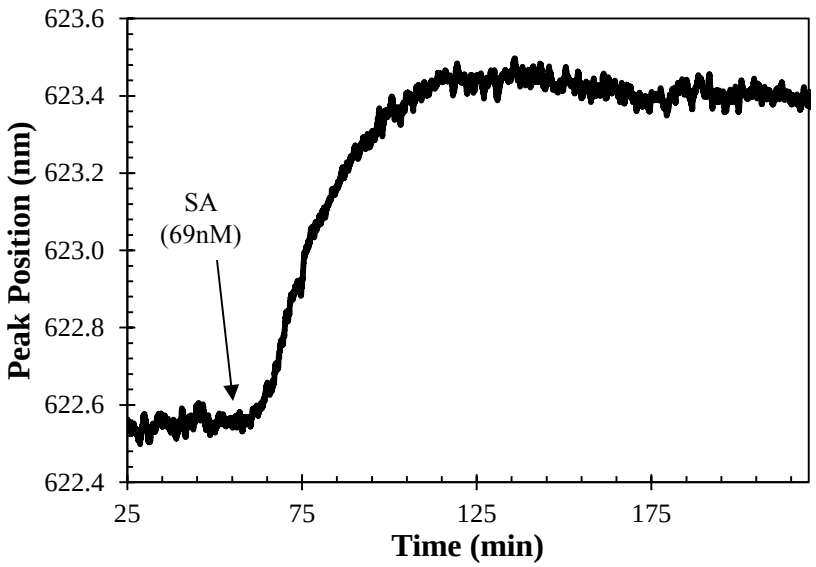

Figure 26. Real time binding results of SA binding to an 11-MUA/1-OT SAM functionalized gold NP surface. As no biotin was present, this is evidence of non-specific binding.

In order to examine methods to block non-specific binding to the sensor surface, a 1% BSA solution was used to block the CH_3 sites, as well as any other potential sites for non-specific binding, such as exposed metal. The first test that was performed is shown in (ii), and aimed to determine if BSA could successfully block the non-specific sites in which SA was adsorbing, as was seen in test (i). For this test, the NP surface was coated in 11-MUA/1-OT SAMs and exposed to 1% BSA for 50 minutes. A large signal change of 4.82nm +/-1.15nm was seen, indicating that the BSA was coating the SAM surface (result shown in Figure 27a). A large signal change from BSA is not surprising due to the large size of BSA. Next, SA was introduced, and no significant signal change was observed. This demonstrates that the BSA successfully blocked non-specific SA adsorption to the surface of the sensor.

The next test, shown in (iv) aimed to determine if BSA blocking inhibited binding of the SA to a biotin functionalized surface. The NP chip was coated in a SAM, followed by functionalization with EDC/NHS and biotin. Then, the non-specific sites were blocked using 1% BSA for 50 minutes. A large signal change of 2.94nm +/-0.45nm was again seen, indicating the BSA was blocking sites on the sensor chip. Next, SA was injected, and a peak shift of 0.80nm was observed. This indicates that while BSA blocks the non-specific sites, it does not block the biotin sites. This allows SA to bind specifically to the biotin without any non-specific binding effects. The result is shown in Figure 27b.

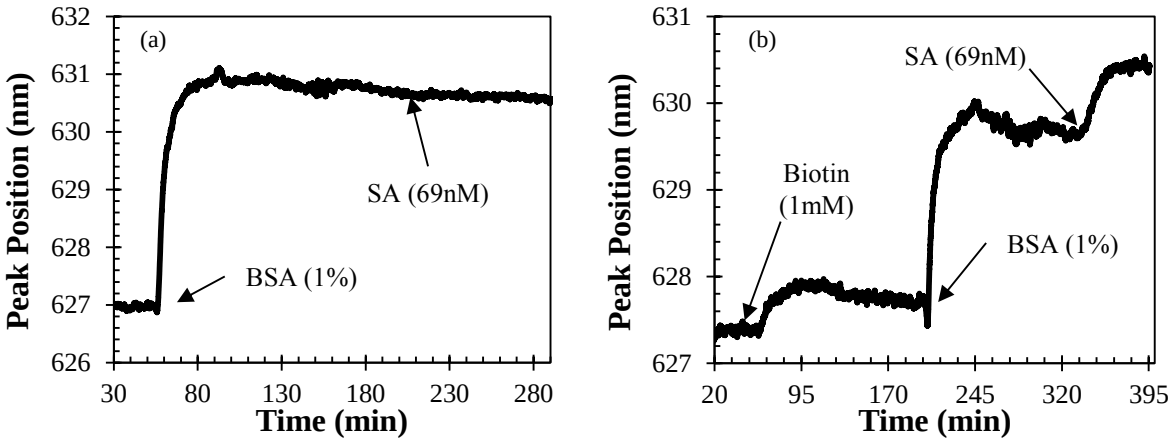

Figure 27. (a) Sensor response to binding of BSA to the SAM coated surface of the gold NPs. Subsequently, SA is injected, and no peak shift is seen, indicating BSA blocks all non-specific sites on the surface. (b) Blocking of a biotin-functionalized surface using BSA. Following BSA blocking, SA is injected, and a peak shift is observed, indicating BSA is not blocking the biotin sites.

A final test was run to determine the ability of the BSA to block other potential proteins that might be present in the solution. This test is essentially the same as that shown in (iv), except there is an

intermediate injection of biotinylated-SA between the BSA and SA injections. First, the NP chip was coated in SAMS, followed by functionalization with EDC/NHS and biotin. Then, the non-specific sites were blocked using 1% BSA for 50 minutes. A large signal change of 2.94nm +/-0.45nm was seen, indicating the BSA was blocking sites on the sensor chip. Next, a mixture of prebiotinylated streptavidin was prepared using a 1:10 concentration ratio of SA to biotin (where [SA] = 69nM and [biotin] = 690nM), to ensure that all of SA's four available binding sites were blocked by biotin molecules. Then, this solution was injected into the sensor system for 50 minutes. No significant peak shift was observed, which indicates that the BSA adequately blocks the sensor against non-specific protein adsorption. Finally, a 69nM SA solution was injected, and a peak shift of 0.93nm +/-0.54nm was observed, indicating the SA was binding only to the biotin capture sites. This test was repeated three times, and the average peak shift due to non-specific binding of prebiotinylated-SA was 0.05nm+/-0.02nm. This is termed the non-specific response. The average peak shift for specific SA binding was found to be 0.93nm +/-0.54nm from the three trials. This is termed the specific response. The results are shown in Figure 28.

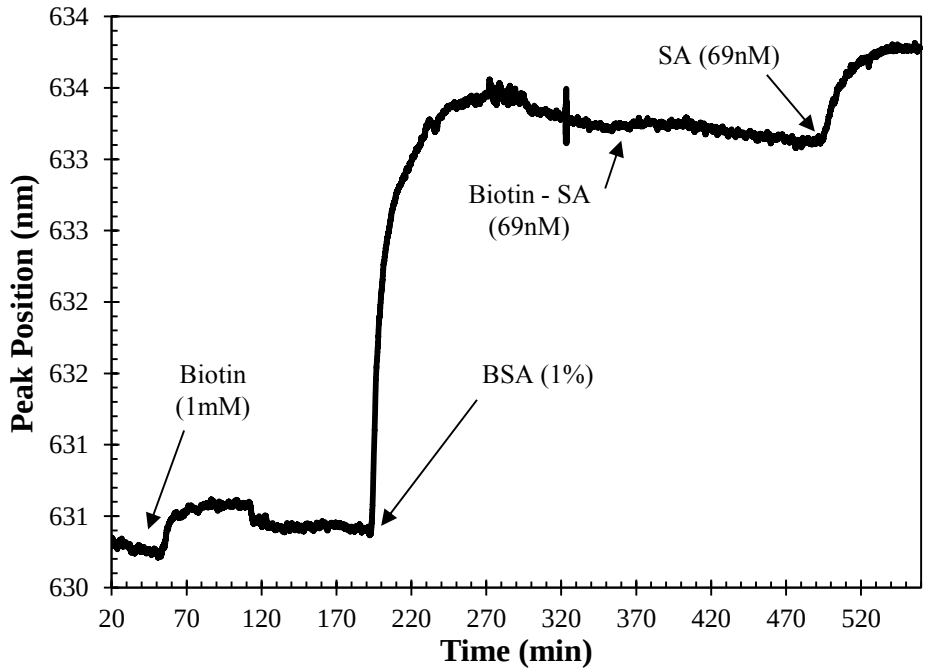

Figure 28. Real time binding results showing the use of BSA to block non-specific binding sites. After blocking the surface minimal response is seen when a biotin-saturated SA sample is injected, indicating minimal non-specific binding. Injection of a pure SA sample results in significant binding, indicating that BSA is able to block non-specific binding without interfering with the specific binding.

The results above demonstrate that in order to ensure the LSPR sensor is responding only to the target analyte, non-specific binding sites must be blocked. In this case, the use of BSA blocked essentially all of the non-specific binding sites that were present on the chip. To examine the significance of blocking the non-specific sites, we compare to the previous results in which no blocking was used, from Section 4.3.1. For the same SA concentration (69nM), an average peak shift of 2.27nm +/-0.51nm was observed without BSA blocking. From the results of the non-specific tests, this peak shift is due to both specific and non-specific binding of SA. The specific response to SA was found to be 0.93nm, which indicates through subtraction that 1.34nm of the peak shift was due to non-specific binding, or approximately 60%. With the use of BSA blocking, we find that that non-specific response is reduced to 0.05nm or 5% of the response, a reduction of over 96%. These results are summarized in Table 10, and indicate that the use of BSA is essential for ensuring that the response of the LSPR sensor is only due to the target analyte. However, it should also be noted that non-specific binding may not be as significant for other types of capture layers. Biotin is a very small molecule, leaving a large amount of open space on the SAM surface which facilitates non-specific binding. Larger antibodies will likely block more of the surface and reduce non-specific binding.

Table 10. Summary of specificity test results with and without BSA blocking for 69nM SA binding to biotin.

Type of Binding	Average Peak Shift (nm), [SA]=69nM
Non-Specific + Specific	2.27
Specific only	0.93
Non-specific (w/out BSA block)	1.34
Non-specific (w/BSA block)	0.05

4.4 HSP70 Results and Discussion

Validation that the LSPR sensor could detect HSP70 was performed using purified salmon HSP70 and its antibody as the capture layer. Experiments to determine whether or not the capture layer could be regenerated using a regeneration buffer were also conducted. The results of these experiments are detailed below.

4.4.1 Initial HSP70 Results

The LSPR peak position was monitored during the formation of the capture layer made of salmon HSP70 antibody and during the subsequent binding of HSP70 to the capture layer. The results are shown below in Figure 29 for the detection of 4.6μg/ml of HSP70 in PBS. The binding of anti-HSP70 results in an LSPR peak shift of 3.4nm. As the sensor is rinsed, the peak drops slightly, which is likely due to the removal of physically bound or non-specifically adsorbed antibody on the surface of the sensor. The binding of 4.6μg/ml of HSP70 to the capture layer results in a peak shift of 0.44nm, which also begins to drop after the rinsing step begins. This is likely due to a combination of non-specifically adsorbed HSP70 being removed as well as a slow unbinding of the HSP70 from its antibody.

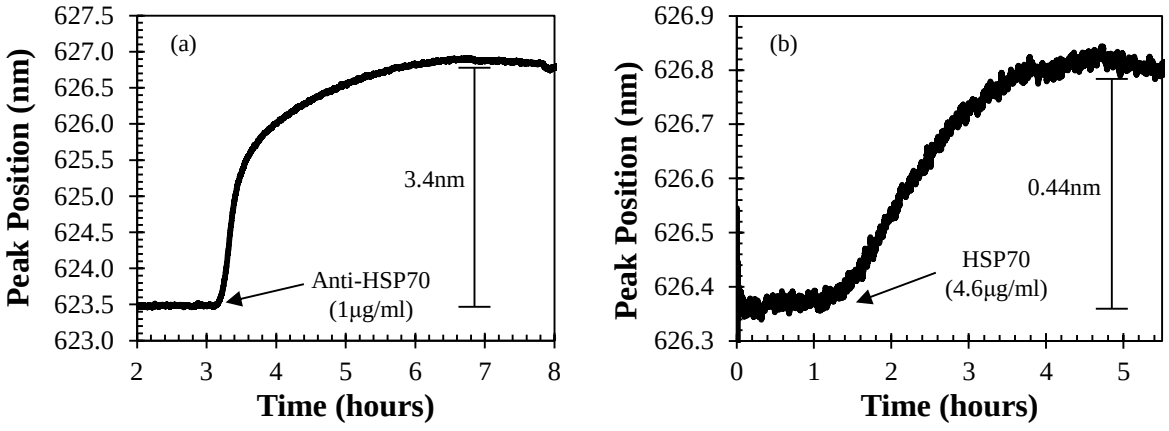

Figure 29. Real time LSPR sensor response showing (a) binding of anti-HSP70 to the SAM functionalized gold NP surface, and (b) binding of HSP70 to the NP surface via the anti-HSP70 capture probe.

This experiment was repeated multiple times using the same conditions, and the LSPR peak shifts for the antibody and protein binding steps have been summarized below in Figure 30. Over the four trials, the antibody shift ranged from 2.54nm to 3.40nm, giving an average of 3.08nm +/-0.28nm. The protein shift ranged from 0.24nm to 0.52nm, with an average of 0.39nm +/-0.12nm. This results in a variation of ~30% over the four trials, which is similar to the error seen with the SA detection and the error reported by the QCM HSP70 sensor [**39**]. This peak shift is much smaller than the typical peak shift seen with streptavidin binding at a similar concentration (2.27nm at 4.2μg/ml), and is most likely due to the very large size of the HSP70 antibody compared to biotin. This is evident in the very large peak shift due to anti-HSP70 binding compared to biotin binding. The large size of the anti-HSP70 causes the HSP70 to bind at a large distance from the NP surface, where it is less sensitive, causing a smaller peak shift. This highlights the importance of optimal nanoparticle design for each biomolecule of interest. The decay

length of these nanoparticles (19.8nm) is significantly longer than the optimal decay length of 6.731nm, so large improvements can be expected when using the optimal nanoparticle geometry for HSP70.

A linear relationship is seen between antibody and protein shift, indicating that the amount of protein binding is closely related to the number of available capture sites. This also explains much of the error seen in the protein binding step, as it is likely caused by variance in the number of binding sites available. The variance in the number of binding sites likely comes from the EDC/NHS modification step. This reaction is known to have a short half-life, so any changes in processing times or concentration will lead to changes in the number of binding sites produced. Therefore, the functionalization process should be optimized and made more consistent in order to reduce this error and facilitate more in-depth testing in the future. However, the results here show that LSPR can be used to successfully detect HSP70. With more development in the functionalization process and the use of the optimized sensor design, this technique has the potential to detect HSP70 at clinically relevant levels with high sensitivity and specificity.

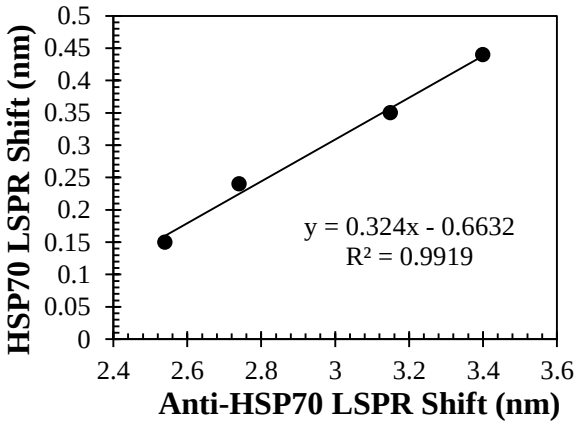

Figure 30. Summary of the LSPR peak shifts from four identical experiments done with anti-HSP70 and HSP70. A linear relationship is seen, indicating that the number of available capture sites determines the amount of HSP70 binding.

4.4.2 Surface regeneration

A protocol using glycine-HCl buffer was also developed to allow in-situ regeneration of the capture layer, so that the protein could be removed without compromising the activity of the antibody. The results of using this buffer to regenerate the surface are shown in Figure 31. Following antibody binding (results not shown), HSP70 was injected at 4.6μg/ml, causing the peak to shift up by 0.52nm to a final position of 629.92nm. After the binding was complete, the glycine-HCl buffer was injected at a concentration of

100mM and a pH of 2.0 for 50 minutes. The peak position dropped almost immediately, from 629.92nm to 629.04nm (0.88nm). Once the glycine buffer exits the flow cell and buffer enters, the peak shifts back up by 0.28nm, resulting in a net drop of 0.60nm. This is very close to the peak shift due to protein binding (0.52nm), indicating that all of the bound protein was removed from the surface without removing the antibody. The additional 0.28nm drop that is seen prior to the glycine buffer exiting the flow cell is likely caused by a small refractive index difference between the glycine buffer and PBS carrier solution. To ensure the antibodies were still active, the flow cell was flushed with PBS and another HSP70 sample injected at the same conditions as the first injection. The binding of HSP70 to the regenerated surface resulted in a peak shift of 0.43nm, which is similar to the peak shift seen in the first injection. This confirms that the glycine-HCl buffer is capable of regenerating the surface without a significant loss of antibody activity. The use of surface regeneration allows more efficient testing and characterizing of the device, since multiple tests can be run without needing to do the entire functionalization process again. It would also allow for a lower final cost per chip, as the same chip could be used multiple times by a simple regeneration step.

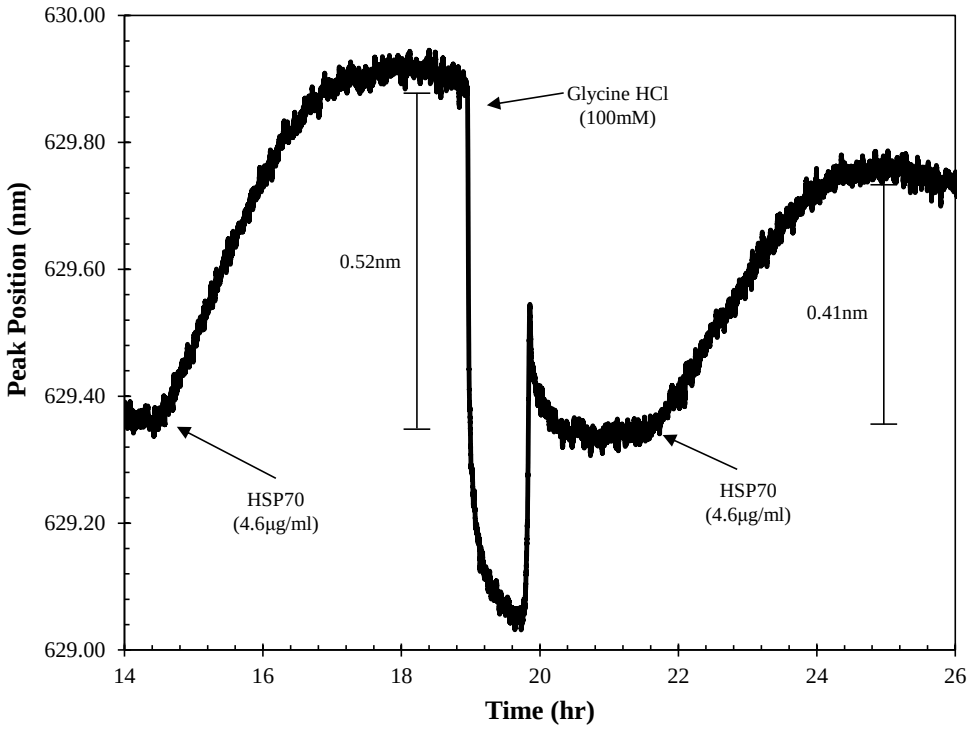

Figure 31. Regeneration of the HSP70 LSPR sensor using a glycine-HCl buffer. After protein binding to the anti-HSP70 capture layer, an injection of glycine-HCl results in the removal of the protein from the capture probe. Subsequent injection of HSP70 results in similar binding, indicating the capture layer is still active after the regeneration treatment.

Chapter 5
Conclusions and Future Work

In this work, a label-free HSP70 sensor based on the LSPR of gold nanoparticle was designed and tested. Optical simulations using CST MWS were used to determine optimal nanoparticle size/shape. From these simulations, the optimal NP geometry for detection of HSP70 was found to be 50nmx5nm gold nanotriangles, which exhibited a sensitivity of 489.8nm/RIU and a decay length of 6.952nm. COMSOL simulations were developed to model the binding of protein to the sensor surface in a microchannel filled with flowing fluid. After investigating the effect of different sensor array sizes and microchannel sizes, the optimal sensor size was found to be 100μmx100μm in a microchannel 100μm in width and 100μm in height. Using the optimized design, the response of the HSP70 sensor was simulated over a wide range of concentrations for a 100μL sample and a sensing time of 30 minutes. The performance of the optimized sensor met or exceeded the design requirements, with a dynamic range from 0.92ng/ml-4000ng/ml, a low end sensitivity of 0.014nm/ng/ml and resolution of 1.1ng/ml. The results of these simulations show that with the optimal design, an LSPR sensor can meet or exceed the necessary performance specifications for label-free detection of HSP70 in a low cost, portable, and rapid format.

The LSPR biosensor was experimentally tested using both the model protein system of biotin-streptavidin and salmon HSP70 and its synthetic antibody. For this purpose, gold nanoparticles of 100nmx100nmx50nm were fabricated on glass using electron beam lithography. A UV-Vis spectroscopy system was built and MATLAB code developed to enable real time tracking of the LSPR peak. A PDMS flow cell was designed and fabricated and interfaced to a flow injection analysis system powered by a syringe pump. The bulk sensitivity was characterized using glycerol-water solutions and found to be 159nm/RIU, with an LSPR peak position at 591nm in air with a FWHM of 85nm, giving a FOM of 1.87. The decay length was found to be 19.8nm +/-0.29nm through the use of layer-by-layer assembly of PSS/PAH polyelectrolytes on the surface of the nanoparticles.

A surface functionalization protocol was developed using alkanethiols of 11-MUA/1-OT with EDC/NHS coupling chemistry for antibody attachment. The response of the sensor to streptavidin was investigated by attaching biotin to the surface of the NPs. Detection of purified streptavidin in real time over the range 55-500,000ng/ml was demonstrated for 50 minutes of sensing time from 500μL samples, which resulted in peaks shifts from 0.07-5.53nm. Using these results an equilibrium binding constant of 9.22×10^{6} M^{-1} was determined. This binding constant is comparable to some studies but is also much lower than other

reported values, which may be due to steric hindrance caused by closely packed biotin molecules. These results demonstrate the ability of the LSPR sensor to detect and quantify streptavidin over a wide range (over 4 orders of magnitude) with a low detection limit of 55ng/ml. The specificity of the sensor was investigated with BSA, and it was found that without the use of BSA to block non-specific binding, the sensor would suffer from approximately 60% non-specific binding in its response. However, BSA blocking was shown to reduce non-specific binding by 96%, to around 5% of the response. These results demonstrate that highly specific protein detection is possible when BSA blocking is employed.

Detection of purified salmon HSP70 was shown through attaching its synthetic antibody to the NP surface. Real time detection of HSP70 was shown for a concentration of 4.6µg/ml, which resulted in a LSPR peak shift of 0.39nm +/- 0.12nm. Numerous trials demonstrated that variability in the density of antibody binding sites caused a proportional variation in the LSPR sensor response. It is hypothesized that slight differences in the reaction time and concentration of the EDC/NHS coupling step is the cause of these variations, and it is recommended that this process be refined to reduce the variation observed. The HSP70 sensor could be regenerated by a pH 2.0 100mM glycine-HCl buffer. The protein could be removed without adversely affecting the antibody capture layer, so that the sensor could be easily reused. A UV-Ozone cleaning process was also developed to completely remove the capture layer from the nanoparticles, and through analysis with XPS it showed to be highly successful at returning the gold substrates to their original state. This allowed the sensor chips to be reused for over 50 tests.

In summary, an optimized LSPR sensor was designed to meet the performance specifications needed for label-free detection of HSP70 in point-of-care and remote applications. A proof of concept LSPR sensor was experimentally shown to detect streptavidin over a wide concentration range with high sensitivity and specificity when using BSA blocking. The LSPR sensor was also shown to detect salmon HSP70 in real time. The many benefits of LSPR sensors, including high sensitivity, ease of use, simple and low cost hardware, and low noise make it an excellent technique for the development of point-of-care HSP70 biosensors.

Future work requires further testing and characterization with HSP70 samples. This includes testing over a range of concentrations to determine the operating range and LOD, and testing non-purified samples (i.e. serum) to evaluate non-specific binding further. Future work also needs to refine the functionalization procedure, specifically the EDC/NHS step, to make it more repeatable to reduce the variation in LSPR peak shifts. To reach the required detection limits experimentally, the optimized nanoparticles should be fabricated, characterized, and tested. Prior to this, AFM should be used to

experimentally determine the thickness of the capture layer and the protein. This will allow more accurate optimization of the decay length compared to relying on thickness values for similar biomolecules reported in literature. Also, new PDMS flow cell molds should be made according to the optimized microchannel dimensions to improve the performance of the sensor further.

Permissions

Permission for reprinting Figure 5, Figure 8, Figure 10 and Figure 11 from [**82**] were obtained from SPIE on May 30, 2012.

Permission for reprinting Figure 6, adapted from [**109**], was obtained from John Wiley and Sons (license number 2917671401262) on May 28, 2012 and from co-author Ronald Stenkamp on July 3, 2012 via email communication.

Permission for reprinting Figure 7 from [**110**] was obtained from Springer (license number 2917680143737) on May 28, 2012.

References

[1] Daniel R. Ciocca and Stuart K. Calderwood, "Heat shock proteins in cancer: diagnostic, prognostic, predictive, and treatment implications," *Cell Stress Chaperones*, vol. 10, no. 2, pp. 86-103, 2005.

[2] M. Abe et al., "Plasma levels of heat shock protein 70 in patients with prostate cancer: a potential biomarker for prostate cancer," *Clinical Prostate Cancer*, vol. 3, no. 1, pp. 49-53, 2004.

[3] A. Brondani Da Rocha et al., "Radioresistance is associated to increased Hsp70 content in human glioblastoma cell lines," *International Journal of Oncology*, vol. 25, no. 3, pp. 777-85, 2004.

[4] Laura M. Vargas-Roig, Francisco E. Gago, Olga Tello, Juan C. Aznar, and Daniel R. Ciocca, "Heat Shock Protein Expression and Drug Resistance in Breast Cancer Patients Treated with Induction Chemotherapy," *Int. J. Cancer (Pred. Oncol.)*, vol. 79, pp. 468-475, 1998.

[5] Guro Valen, Goran K Hansson, Alexandra Dumitrescu, and Jarle Vaage, "Unstable angina activates myocardial heat shock protein 72, endothelial nitric oxide synthase, and transcription factors NFkB and AP-1," *Cardiovascular Research*, vol. 47, no. 1, pp. 49-56, 2000.

[6] Simon G. Thompson, Joachim Kienast, Stephen D.M. Pyke, Frits Haverkate, and Jurgen C.W. Van De Loo, "Hemostatic Factors and the Risk of Myocardial Infarction or Sudden Death in Patients With Angina Pectoris," *The New England Journal of Medicine*, vol. 332, no. 10, pp. 635-641, 1995.

[7] Anne A. Knowlton et al., "Differential Expression of Heat Shock Proteins in Normal and Failing Human Hearts," *Journal of Molecular and Cellular Cardiology*, vol. 30, no. 4, pp. 811-818, 1998.

[8] Alice Banh, Mathilakath M. Vijayan, and Jacob G. Sivak, "Hsp70 in bovine lenses during temperature stress," *Molecular Vision*, vol. 9, pp. 323-328, 2003.

[9] F. Schramm et al., "A cascade of transcription factor DREB2A and heat stress transcription factor HsfA3 regulates the heat stress response of Arabidopsis," *Plant Journal*, vol. 53, no. 2, pp. 264-274, 2008.

[10] J.B. Cara, N. Aluru, F.J. Moyano, and M.M. Vijayan, "Food-Deprivation induces HSP70 and HSP90 protein expression in larval gilthead sea bream and rainbow trout," *Comparative Biochemistry and Physiology, Part B*, vol. 142, pp. 426-431, 2005.

[11] E.S. Chang, "Stressed-out lobsters: Crustacean hyperglycemic hormone and stress proteins," *Integrative and Comparative Biology*, vol. 45, no. 1, pp. 43-50, 2005.

[12] Caroline Methling, Neelakanteswar Aluru, Mathilakath M. Vijayan, and John F. Steffensen, "Effect of moderate hypoxia at three acclimation temperatures on stress responses in Atlantic cod with different haemoglobin types," *Comparative Biochemistry and Physiology, Part A*, vol. 156, pp.

485-490, 2010.

[13] Steve Wiseman, Even H. Jorgensen, Alec G. Maule, and Mathilakath M. Vijayan, "Contaminant loading in remote Arctice lakes affects cellular stress-related proteins expression in feral charr," *Polar Biology*, vol. 34, pp. 933-937, 2011.

[14] C. Corporeau and M. Auffret, "In situ hybridisation for flow cytometry: A molecular method for monitoring stress-gene expression in hemolymph cells of oysters," *Aquatic Toxicology*, vol. 64, no. 4, pp. 427-435, 2003.

[15] Qiang Feng, Adrienne N. Boone, and Mathilakath M. Vijayan, "Copper impact on heat shock protein 70 expression and apoptosis in rainbow trout hepatocytes," *Comparative Biochemistry and Physiology Part C*, vol. 135, pp. 345-355, 2003.

[16] Paul K. S. Lam and John S. Gray, "The use of biomarkers in environmental monitoring programmes," *Marine Pollution Bulletin*, vol. 46, pp. 182-186, 2003.

[17] Melody S. Clark and Lloyd S. Peck, "HSP70 heat shock proteins and environmental stress in Antarctic marine organisms: A mini-review," *Marine Genomics*, pp. 11-18, 2009.

[18] Jason W. Hamilton, "Evaluation of indicators of stress in populations of polar bears (Ursus maritimus) and grizzly bears (Ursus arctos)," University of Waterloo, Waterloo, MSc Thesis 2007.

[19] Liviu Nicu and Thierry Leichle, "Biosensors and tools for surface functionalization from the macro- to the nanoscale: the way forward," *Journal of Applied Physics*, vol. 104, no. 111101, pp. 1-16, 2008.

[20] Guenter Gauglitz, "Direct optical sensors: principles and selected applications," *Anal Bioanal Chem*, vol. 381, pp. 141-155, November 2005.

[21] Jonathan S. Daniels and Nader Pourmand, "Label-free impedance biosensors: opportunities and challenges," *Electroanalysis*, vol. 19, no. 12, pp. 1239-1257, May 2007.

[22] Matthew A. Cooper,. Cambridge, USA: Cambridge University Press, 2009, pp. 2-3.

[23] Rashid Bashir, "BioMEMS: state-of-the-art in detection, opportunities and prospects," *Advanced Drug Delivery Reviews*, vol. 56, pp. 1565-1586, 2004.

[24] Niroshan Ramachandran, Dale N. Larson, Peter R. H. Stark, Eugenie Hainsworth, and Joshua LaBaer, "Emerging tools for real-time label-free detection of interactions on functional protein microarrays," *FEBES*, vol. 272, pp. 5412-5425, 2005.

[25] Alphonsus H. C. Ng, Uvaraj Uddayasankar, and Aaron R. Wheeler, "Immunoassays in microfluidic systems," *Anal Bioanal Chem*, vol. 397, pp. 991-1007, 2010.

[26] Seokheun Choi, Michael Goryll, Lai Yi Mandy Sin, Pak Kin Wong, and Junseok Chae, "Microfluidic-based biosensors toward point-of-care detection of nucleic acids and proteins," *Microfluid Nanofluid*, vol. 10, pp. 231-247, 2011.

[27] Maria A. Schwarz and Peter C. Hauser, "Recent developments in detection methods for microfabricated analytical devices," *Lab on a Chip*, vol. 1, pp. 1-6, 2001.

[28] Torna E. Esterhouse and Lado B. Petrinos, "Protein Biosynthesis," in *Recent advances in label-free biosensors: applications in protein biosynthesis and HTS screening*. United Kingdom: Nova Science Publishers, 2009, ch. 7, pp. 163-194.

[29] Adam Bange, Brian H. Halsall, and William R. Heineman, "Microfluidic immunosensor systems," *Biosensors and Bioelectronics*, vol. 20, pp. 2488-2503, 2005.

[30] Robert S. Marks et al., Eds., *Handbook of Biosensors and Biochips*.: Wiley-Interscience , 2007.

[31] Anna J. Tudos, Geert A. J. Besselink, and Richard B. M. Schasfoort, "Trends in miniaturized total analysis systems for point-of-care testing in clinical chemistry," *Lab on a Chip*, vol. 1, pp. 83-95, 2001.

[32] Xudong Fan et al., "Sensitive optical biosensors for unlabeled targets: A review," *Anal. Chim. Acta*, vol. 620, pp. 8-26, 2008.

[33] Frank B. Myers and Luke P. Lee, "Innovations in optical microfluidic technologies for point-of-care diagnostics," *Lab on a Chip*, vol. 8, pp. 2015-2031, 2008.

[34] A. Ahluwalia, D. De Rossi, A. Schirone, and G. Serra, "A comparative study of protein immobilization techniques for optical immunosensors," *Biosensors and Bioelectronics*, vol. 7, pp. 207-214, 1991.

[35] Electra Gizeli and Christopher R. Lowe, *Biomolecular Sensors*. London, UK: Taylor and Francis, 2002.

[36] Greg T. Hermanson, *Bioconjugate Techniques*, 2nd ed. London, UK: Elsevier, 2008.

[37] Paul Yager, Gonzalo J. Domingo, and John Gerdes, "Point-of-Care Diagnostics for Global Health," *Annu. Re. Biomed. Eng.*, vol. 10, pp. 107-144, March 2008.

[38] Robert H Christenson and Hassan Azzazy, "Cardiac point of care testing: A focused review of current National Academy of Clinical Biochemistry guidelines and measurement platforms," *Clinical Biochemistry*, vol. 42, pp. 150-157, 2009.

[39] M. Mascini et al., "Piezoelectric sensors based on biomimetic peptides for the detection of heat shock proteins (HSPs) in mussels," *Analytical Letters*, vol. 39, no. 8, pp. 1627-2642, 2006.

[40] Ying Sun et al., "Sensitivity enhancement of wavelength modulation surface plasmon resonance biosensor by improving the baseline solution," *Analytica Chemica Acta*, vol. 569, pp. 21-26, 2006.

[41] Hideki Maeda et al., "Biological heterogeneity of the peptide-binding motif of the 70-kDa heat shock protein by surface plasmon resonance analysis," *J. Biol. Chem.*, vol. 282, pp. 26956-26962, 2007.

[42] Curtis D. Chin, Vincent Linder, and Samuel K. Sia, "Lab-on-a-chip devices for global health: Past studies and future opportunities," *Lab on a Chip*, vol. 7, pp. 41-57, October 2006.

[43] Xiaodi Su and Jian Zhang, "Comparison of surface plasmon resonance spectroscopy and quartz crystal microbalance for human IgE quantification," *Sensors and Actuators B*, vol. 100, pp. 309-314, 2004.

[44] R. B. M. Schasfoort and Anna J. Tudos, Eds., *Handbook of surface plasmon resonance*. Cambridge, UK: The Royal Society of Chemistry, 2008.

[45] Eleonora Petryayeva and Ulrich J. Krull, "Localized surface plasmon resonance: Nanostructures, bioassays, and biosensing - A review," *Anal. Chim. Acta*, vol. 706, pp. 8-24, 2011.

[46] Kathryn M. Mayer and Jason H. Hafner, "Localized surface plasmon resonance sensors," *Chem. Rev.*, vol. 111, pp. 3823-3857, 2011.

[47] Jeffrey N. Anker et al., "Biosensing with plasmonic nanosensors," *Nature Materials*, vol. 7, pp. 442-453, June 2008.

[48] Katherine A. Willets and Richard P. Van Duyne, "Localized Surface Plasmon Resonance Spectroscopy and Sensing," *Annu. Rev. Phys. Chem.*, vol. 58, pp. 267-297, 2007.

[49] Amanda J. Haes and Richard P. Van Duyne, "A highly sensitive and selective suface-enhanced nanobiosensor," *Mat. Res. Soc. Symp. Proc.*, vol. 723, pp. O3.1.1-O3.1.6, 2002.

[50] Amanda J. Haes, W. Paige Hall, Lei Chang, William L. Klein, and Richard P. Van Duyne, "A Localized Surface Plasmon Resonance Biosensor: First Steps toward an Assay for Alzheimer's Disease," *Nano Letters*, vol. 4, no. 6, pp. 1029-1034, 2004.

[51] Amanda J. Haes, Lei Chang, William L. Klein, and Richard P. Van Duyne, "Detection of a biomarker for alzheimer's disease from synthetic and clinical samples using a nanoscale optical biosensor," *J. Am. Chem. Soc.*, vol. 127, no. 7, pp. 2264-2271, 2005.

[52] Shaoli Zhu, ChunLei Du, and Yongqi Fu, "Fabrication and characterization of rhombic silver nanoparticles for biosensing," *Opt. Mater.*, vol. 31, pp. 769-774, 2009.

[53] Kathryn M. Mayer et al., "A label-free immunoassay based upon localized surface plasmon resonance of gold nanorods," *ACS Nano*, vol. 2, no. 4, pp. 687-692, 2008.

[54] Tatsuro Endo et al., "Multiple label-free detection of antigen-antibody reaction using localized surface plasmon resonance-based core-shell structured nanoparticle layer nanochip," *Anal. Chem.*, vol. 78, pp. 6465-6475, 2006.

[55] Ha Minh Hiep et al., "A microfluidic chip based on localized surface plasmon resonance for real-time monitoring of antigen-antibody reaction," *Jpn. J. Appl. Phys.*, vol. 47, no. 2, pp. 1337-1341, 2008.

[56] Gregory Barbillon et al., "Biological and chemical gold nanosensors based on localized surface plasmon resonance," *Gold Bull.*, vol. 40, no. 3, pp. 240-244, 2007.

[57] Seunghyun Lee, Kathryn M. Mayer, and Jason H. Hafner, "Improved localized surface plasmon resonance immunoassay with gold bipyramid substrates," *Anal. Chem.*, vol. 81, no. 11, pp. 4450-4455, 2009.

[58] Tatsuro Endo, Kagan Kerman, Naoki Nagatani, Yuzuru Takamura, and Eiichi Tamiya, "Label-free detection of peptide nucleic acid - DNA hybridization using localized surface plasmon based optical sensors," *Anal. Chem.*, vol. 77, no. 21, pp. 6976-6984, November 2005.

[59] Do-Kyun Kim et al., "Label-free DNA biosensor based on localized surface plasmon resonance coupled with interferometry," *Anal. Chem.*, vol. 79, no. 5, pp. 1855-1864, March 2007.

[60] So Young Yoo et al., "Detection of the most common corneal dystrophies caused by BIGH3 gene point mutations using a multispot gold-capped nanoparticle array chip," *Anal. Chem.*, vol. 82, no. 4, pp. 1349-1357, February 2010.

[61] Linda Olofsson, Tomas Rindzevicius, Indriati Pfeiffer, Mikael Kall, and Fredrick Hook, "Surface-based gold-nanoparticle sensor for specific and quantitative DNA hybridization detection," *Langmuir*, vol. 19, no. 24, pp. 10414-10419, October 2003.

[62] Chia-Sheng Cheng, Yu-Quan Chen, and Chia-Jung Lu, "Organic vapour sensing using localized surface plasmon resonance spectrum of metallic nanoparticles self assemble monolayer," *Talanta*, vol. 73, no. 2, pp. 358-365, September 2007.

[63] Kuan-Jen Chen and Chia-Jung Lu, "A vapor sensor array using multiple localized surface plasmon resonance bands in a single UV-vis spectrum," *Talanta*, vol. 81, no. 4-5, pp. 1670-1675, June 2010.

[64] Yu-Quan Chen and Chia-Jung Lu, "Surface modification on silver nanoparticles for enhancing vapor selectivity of localized surface plasmon resonance sensors," *Sens. Actuators, B*, vol. 135, no. 2, pp. 492-498, 2009.

[65] Stephan T. Dubas and Vimolvan Pimpan, "Green synthesis of silver nanoparticles for ammonia sensing," *Talanta*, vol. 76, no. 1, pp. 29-33, 2008.

[66] Tsao-Jen Lin and Mon-Fu Chung, "Detection of cadmium by a fiber-optic biosensor based on

localized surface plasmon resonance," *Biosens. Bioelectron.*, vol. 24, no. 5, pp. 1213-1218, 2009.

[67] Zhi-Mei Qi, Itaru Honma, and Haoshen Zhou, "Humidity sensor based on localized surface plasmon resonance of multilayer thin films of gold nanoparticles linked with myoglobin," *Opt. Lett.*, vol. 31, no. 12, pp. 1854-1856, June 2006.

[68] Anuj Dhawan and John F. Muth, "Plasmon resonances of gold nanoparticles incorporated inside an optical fibre matrix," *Nanotechnology*, vol. 17, no. 10, pp. 2504-2511, 2006.

[69] Markus Nuopponen and Heikki Tenhu, "Gold nanoparticles protected with pH and temperature-sensitive diblock copolymers," *Langmuir*, vol. 23, no. 10, pp. 5352-5357, 2007.

[70] Amanda J. Haes and Richard P. Van Duyne , "A unified view of propagating and localized surface plasmon resonance biosensors," *Anal. Bioanal. Chem.*, vol. 379, pp. 920-930, 2004.

[71] Gustav Mie, "Beiträge zur Optik trüber Medien, speziell kolloidaler Metallösungen," *Ann. Phys.*, vol. 330, pp. 377-445, 1908.

[72] A. Grimault, A. Vial, and M. Lamy De la Chapelle, "Modeling of regular gold nanostructures arrays for SERS application using a 3D FDTD method," *Appl. Phys. B.*, vol. 84, pp. 111-115, 2006.

[73] Leif Sherry, Rongchao Jin, Chad Mirkin, Schatz George, and Richard Van Duyne, "Localized surface plasmon resonance spectroscopy of single silver triangular nanoprisms," *Nano Letters*, vol. 6, no. 9, pp. 2060-2065, 2006.

[74] Linfang Qiao et al., "Localized surface plasmon resonance enhanced organic solar cell with gold nanospheres," *Applied Energy*, vol. 88, pp. 848-852, 2010.

[75] Bjoern Niesen et al., "Excitation of multiple dipole surface plasmon resonances in spherical silver nanoparticles," *Optics Express*, vol. 18, no. 18, August 2010.

[76] Jing Zhao et al., "Methods for describing the electromagnetic properties of silver and gold nanoparticles," *Acc. Chem. Res*, vol. 41, no. 12, pp. 1710-1720, 2008.

[77] Tatsuro Endo, Ryuzoh Ikeda, Yasuko Yanagida, and Takeshi Hatsuzawa, "Stimuli-responsive hydrogel-silver nanoparticles composite for development of localized surface plasmon resonance-based optical biosensor," *Analytica Chimca Acta*, vol. 611, pp. 205-211, February 2008.

[78] Andrew Taton, Gang Lu, and Chad Mirkin, "Two-color labeling of oligonucleotide arrays via size-selective scattering of nanoparticle probes," *J. Am. Chem. Soc.*, vol. 123, pp. 5164-5165, 2001.

[79] Tatyana A. Bendikov, Aharon Rabinkov, Tanya Karakouz, Alexander Vaskevich, and Israel Rubinstein, "Biological sensing and interface design in gold island film based localized surface plasmon transducers," *Anal. Chem.*, vol. 80, pp. 7487-7498, 2008.

[80] Linda S. Jung, Charles T. Campbell, Timothy M. Chinowsky, Mimi N. Mar, and Sinclair S. Yee, "Quantitative interpretation of the response of surface plasmon resonance sensors to adsorbed films," *Langmuir*, vol. 14, pp. 5636-5648, 1998.

[81] Ofer Kedem, Alexander B. Tesler, Alexander Vaskevich, and Israel Rubinstein, "Sensitivity and optimization of localized surface plasmon resonance transducers," *ACS Nano*, vol. 5, no. 2, pp. 748-760, 2011.

[82] Ryan C. Denomme, Zachary Young, Lindsay Brock, and Patricia M. Nieva, "Optimization of a localized surface plasmon resonance biosensor for heat shock protein 70," in *SPIE Photonics West*, San Francisco, 2012, pp. 8269G-1:13.

[83] Andreas B. Dahlin, Jonas O. Tegenfeldt, and Fredrik Hook, "Improving the instrumental resolution of sensors based on localized surface plasmon resonance," *Anal. Chem.*, vol. 78, pp. 4416-4423, 2006.

[84] Greg J. Nusz, Adam C. Curry, Stella M. Marinakos, Adam Wax, and Ashutosh Chilkoti, "Rational selection of gold nanorod geometry for label-free plasmonic biosensors," *ACS Nano*, vol. 3, no. 4, pp. 795-806, 2009.

[85] Leyla Soleymani et al., "Hierarchical nanotextured microelectrodes overcome the molecular transport barrier to achieve rapid, direct bacterial detection," *ACS Nano*, vol. 5, no. 4, pp. 3360-3366, 2011.

[86] Chanda Ranjit Yonzon et al., "A comparative analysis of localized and propagating surface plasmon resonance sensors: the binding of concanavalin A to a monosaccharide functionalized self-assembled monolayer," *J. Am. Chem. Soc.*, vol. 126, pp. 12669-12676, 2004.

[87] Pei-Yu Chung, Tzung-Hua Lin, Gregory Schultz, Christopher Batich, and Peng Jiang, "Nanopyramid surface plasmon resonance sensors," *Appl Phys Lett.*, vol. 96, no. 26, pp. 261108-1:-3, 2010.

[88] Chengjun Huang et al., "An on-chip localized surface plasmon resonance-based biosensor for label-free monitoring of antigen-antibody reaction," *Microelectronic Engineering*, vol. 86, pp. 2437-2441, 2009.

[89] G. Barbillon, F. Hamouda, S. Held, P. Gogol, and B. Bartenlian, "Gold nanoparticles by soft UV nanoimprint lithography coupled to a lift-off process for plasmonic sensing of antibodies," *Microelectron. Eng.*, vol. 87, no. 5-8, pp. 1001-1004, 2010.

[90] Yi Wang, Weiping Qian, Yong Tan, and Shaohua Ding, "A label-free biosensor based on gold nanoshell monolayers for monitoring biomolecular interactions in diluted whole blood," *Biosensors and Bioelectronics*, vol. 23, pp. 1166-1170, 2008.

[91] Ha Minh Hiep, Hiroyuki Yoshikawa, and Eiichi Tamiya, "Interference localized surface plasmon resonance nanosensor tailored for the detection of specific biomolecular interactions," *Anal. Chem.*

, vol. 82, no. 4, pp. 1221-1227, 2010.

[92] Takumi Sannomiya, Tobias E. Balmer, Christian Hafner, Manfred Heuberger, and Janos Voros, "Optical sensing and determination of complex reflection coefficients of plasmonic structures using transmission interferometric plasmonic sensor," *Rev. Sci. Instrum.*, vol. 81, pp. 053102-1:-9, 2010.

[93] Amanda J. Haes and Richard P. Van Duyne, "Preliminary studies and potential applications of localized surface plasmon resonance spectroscopy in medical diagnostics," *Expert Rev. Mol. Diagn.*, vol. 4, no. 4, pp. 527-537, 2004.

[94] Ryan C. Denomme, Zachary W. Young, and Patricia M. Nieva, "Temperature dependence of a localized surface plasmon resonance immunosensor based on gold nanoparticles," *In Preparation*, 2012.

[95] Chengjun Huang et al., "Localized surface plasmon resonance biosensor integrated with microfluidic chip," *Biomed Microdevices*, vol. 11, pp. 893-901, 2009.

[96] Philip J. R. Roche, Sandrine Filion-Cote, Maurice C.-K. Cheung, Vamsy P. Chodavarapu, and Andrew G. Kirk, "A camera phone localised surface plasmon biosensing platform towards low-cost label-free diagnostic testing," *Journal of Sensors*, vol. 2011, pp. 1-7, 2011.

[97] Shaoli Zhu, ChunLei Du, and Yongqi Fu, "Localized surface plasmon resonance-based hybrid Au-Ag nanoparticles for detection of Staphylococcus aureus enterotoxin B," *Optical Materials*, vol. 31, pp. 1608-1613, 2009.

[98] Pavel Neuzil and Julien Reboud, "Palm-sized biodetection system based on localized surface plasmon resonance," *Anal. Chem.*, vol. 80, pp. 6100-6103, 2008.

[99] Daniele Gerion and Gwo-Jen Day, "Localized surface plasmon resonance for bioprocess development, monitoring, and validation," *BioProcess International*, vol. 9, no. 8, pp. 70-75, September 2011.

[100] Amanda J. Haes and Richard P. Van Duyne, "A Nanoscale Optical Biosensor: Sensitivity and Selectivity of an Approach Based on the Localized Surface Plasmon Resonance Spectroscopy of Triangular Nanoparticles," *J. Am. Chem. Soc.*, vol. 124, no. 1, pp. 10596-10604, 2002.

[101] Christopher J. Love, Lara A. Estroff, Jennah K. Kriebel, Ralph G. Nuzzo, and George M. Whitesides, "Self-Assembled Monolayers of Thiolates on Metals as a Form of Nanotechnology," *Chemical Reviews*, vol. 105, pp. 1103-1169, 2005.

[102] S. Ferretti, S. Paynter, D. Russell, K. Sapsford, and D. Richardson, "Self-assembled monolayers: a versatile tool for the formation of bio-surfaces," *Trends in Analytical Chemistry*, vol. 19, no. 9, pp. 530-540, 2000.

[103] R.G. Nuzzo and D.L. Allara, "Adsorption of bifunctional organic disulfides on gold surfaces," *Journal of American Chemical Society*, vol. 105, pp. 4481-4483, 1983.

[104] James V. Staros, Rick W. Wright, and Deborah M. Swingle, "Enhancement by N_Hydroxysulfosuccinimide of Water-Soluble Carbodiimide-Mediated Coupling Reactions," *Analytical Biochemistry*, vol. 156, pp. 220-222, 1986.

[105] F. Luderer and U. Walschus, "Immobilization of Oligonucleotides for Biochemical Sensing by Self-Assembled Monolayers: Thiol-Organic Bonding on Gold and Silanization on Silica Surfaces," *Top Current Chemistry*, vol. 260, pp. 37-56, 2005.

[106] Xin Li, Li Jiang, Qiuqiang Zhan, Jun Qian, and Sailing He, "Localized surface plamson resonance (LSPR) of polyelectrolyte-functionalized gold-nanoparticles for bio-sensing," *Colloids and Surfaces A: Physiochem. Eng. Aspects*, vol. 332, no. 1, pp. 172-179, 2009.

[107] T. Arai, P. K. R. Kumar, C. Rockstuhl, K. Awazu, and J. Tominaga, "An optical biosensor based on localized surface plasmon resonance of silver nanostructered films," *Journal of Optics A: Pure and Applied Optics*, vol. 9, no. 1, pp. 699-703, 2007.

[108] Anders Holmberg et al., "The biotin-streptavidin interaction can be reversibly broken using water at elevated temperatures," *Electrophoresis*, vol. 26, no. 1, pp. 501-510, 2005.

[109] Stefanie Freitag, Isolde Le Trong, Lisa Klumb, Patrick Stayton, and Ronald E. Stenkamp, "Structural studies of the streptavidin binding loop," *Protein Science*, vol. 6, pp. 1157-1166, 1997.

[110] U. Feige and B. S. Polla, "Heat shock proteins: the hsp70 family," *Experientia*, vol. 50, pp. 979-86, 1994.

[111] C. Georgopoulos and W. J. Welch, "Role of the Major Heat Shock Proteins as Molecular Chaperones," *Annual Review of Cell Biology*, vol. 9, pp. 601-34, 1993.

[112] S. Lindquist and E.A. Craig, "The Heat-Shock Proteins," *Annual Review of Genetics*, vol. 22, pp. 631-677, 1988.

[113] U. Feige, R.I. Morimoto, I. Yahara, and B.S. Polla, *Stress-Inducible Cellular Responses*. Basel: Birkhauser Verlag, 1996.

[114] Amie J. McClellan and Judith Frydman, "Molecular chaperones and the art of recognizing a lost cause," *Nature Cell Biology*, vol. 3, pp. 51-53, 2001.

[115] Hideki Sakahira, Peter Breuer, Manajit K. Hayer-Hartl, and F. Ulrich Hartl, "Molecular chaperones as modulators of polyglutamine protein aggregation and toxicity," *Proceedings of the National Academy of Sciences of the United States of America*, vol. 99, pp. 16412-16418, 2002.

[116] Dawn A. Parsell, Anthony S. Kowal, Mike A. Singer, and Susan Lindquist, "Protein disaggregation mediated by heat-shock protein Hsp104," *Nature*, vol. 372, pp. 475-478, 1994.

[117] A. L. Fink, "Chaperone-mediated protein folding," *Physiol Rev.*, vol. 425-49, p. 79, 1999.

[118] Susan Lindquist, "The Heat-Shock Response," *Annual Review of Biochemistry*, vol. 55, pp. 1151-1191, 1986.

[119] Nathan C. Dyck, Ryan C. Denomme, and Patricia M. Nieva, "Effective medium properties of arbitrary nanoparticle shapes in a localized surface plasmon resonance sensing layer," *J. Phys. Chem. C*, vol. 115, pp. 15225-15233, 2011.

[120] H. Angus Macleod, *Thin-Film Optical Filters*, 4th ed. Boca Raton, FL, United States: CRC Press, 2010.

[121] W. Andrew Murray, Baptiste Auguie, and William L. Barnes, "Sensitivity of localized surface plasmon resonances to bulk and local changes in the optical environment," *J. Phys. Chem. C*, vol. 113, pp. 5120-5125, 2009.

[122] Amanda J. Haes, Shengli Zou, George C. Schatz, and Richard P. Van Duyne, "A nanoscale optical biosensor: the long range distance dependence of the localized surface plasmon resonance of noble metal nanoparticles," *J. Phys. Chem. B*, vol. 108, pp. 109-116, 2004.

[123] Marek Piliarik, Pavel Kvasnicka, Nicolle Galler, Joachim R. Krenn, and Jiri Homola, "Local refractive index sensitivity of plasmonic nanoparticles," *Optics Express*, vol. 19, no. 10, pp. 9213-9220, 2011.

[124] P. B. Johnson and R. W. Christy, "Optical constants of the noble metals," *Phys. Rev. B*, vol. 6, pp. 4370-4379, 1972.

[125] Cheng Zhou et al., "Human immunoglobulin adsorption investigated by means of quartz crystal microbalance dissipation, atomic force microscopy, surface acoustic wave, and surface plasmon resonance techniques," *Langmuir*, vol. 20, pp. 5870-5878, 2004.

[126] Charles J. Choi, Alysia R. Belobraydich, Leo L. Chan, Patrick C. Mathias, and Brian T. Cunningham, "Comparison of label-free biosensing in microplate, microfluidic, and spot-based affinity capture assays," *Analytical Biochemistry*, vol. 405, pp. 1-10, 2010.

[127] Ajit Sadana and David Sii, "Binding kinetics of antigen by immobilized antibody: Influence of reaction order and external diffusional limitations," *Biosensors and Bioelectronics*, vol. 7, pp. 559-568, 1992.

[128] Jennifer O. Foley, Afshin Mashadi-Hossein, Elain Fu, Bruce A. Finlayson, and Paul Yager, "Experimental and model investigation of the time-dependent 2-dimensional distribution of binding in a herringbone microchannel," *Lab Chip*, vol. 8, pp. 557-564, 2008.

[129] Guoqing Hu, Yali Gao, and Dongqing Li, "Modeling micropatterned antigen-antibody binding kinetics in a microfluidic chip ," *Biosensors and Bioelectronics*, vol. 22, pp. 1403-1409, 207.

[130] A. Brask, G. Goranovic, and H. Bruus, "Theoretical analysis of the low-voltage cascade

electroosmotic pump," *Sens. Actuators B Chem*, vol. 92, pp. 127-132, 2003.

[131] J. A. De Feijter, J. Benjamins, and F. A. Veer, "Ellipsometry as a tool to study the adsorption of synthetic and biopolymers at the air-water interface," *Biopolymers*, vol. 17, pp. 1759-1772, 1978.

[132] TH. G. Scholte, "Relation between the refractive index increment and the density increment of binary mixtures: application to the determination of partial specific volumes of polymers in solution," *J. Polym. Sci., Part A-2*, vol. 10, no. 3, pp. 519-526, 1972.

[133] Brendan D. Smith et al., "Development and optimization of a label-free heat shock protein 70 immobilization protocol using a quartz crystal microbalance," *In preparation*, 2012.

[134] G Barbillon et al., "Electron beam lithography designed chemical nanosensors based on localized surface plasmon resonance," *Surf. Sci.*, vol. 601, no. 21, pp. 5057-5061, 2007.

[135] Shaoli Zhu and Yongqi Fu, "Optical Biochip with Mutlichannels for Detecting Biotin-Streptavidin Based on Localized Surface Plasmon Resonance," *Plasmonics*, vol. 4, no. 1, pp. 209-216, 2009.

[136] Michal Lahav, Alexander Vaskevich, and Israel Rubinstein, "Biological Sensing Using Transmission Surface Plasmon Resonance Spectroscopy," *Langmuir*, vol. 20, no. 1, pp. 7365-7367, 2004.

[137] Xiaohui Wang et al., "Gold nanorod-based localized surface plasmon resonance biosensor for sensitive detection of hepatitis B virus in buffer, blood serum and plasma," *Biosensors and Bioelectronics*, vol. 26, no. 1, pp. 404-410, 2010.

[138] Vitalii Silin, Howard Weetall, and David J. Vanderah, "SPR studies of the nonspecific adsorption kinetics of human IgG and BSA on gold surfaces modified by self-assembled monolayers (SAMs)," *Journal of Colloid and Interface Science*, vol. 185, pp. 94-103, 1997.

Appendix A
Decay Length Determination

In order to characterize the decay length using polyelectrolyte multilayers, the thickness of the PAH and PSS layers needed to be determined. This was accomplished using ellipsometry. PAH/PSS multilayers were assembled on planar gold substrates. The substrates were cleaned via Piranha solution. Two polyelectrolyte solutions were prepared at concentrations of 1mM in a 0.1M sodium chloride solution in water. A salt solution was prepared for rinsing, consisting of 0.1M sodium chloride in water. Gold substrates were placed into the PAH solution for 15 minutes, followed by 30 seconds of rinsing with the salt solution and 30 seconds of incubation in a beaker of the salt solution. The substrates were then placed into the PSS solution for 15 minutes, followed by the same rinsing procedure. This process was repeated to obtain substrates with various numbers of bilayers (4, 8, 12, 16, and 20 bilayers). Two sets of substrates with each bilayer number were made (trial 1 and trial 2), and the thickness measured using ellipsometry. The results are shown in Figure 32. Plotting the layer thickness vs. bilayer number and performing linear regression allows for determination of the thickness of any number of layers. This is then be used to determine the decay length when performing the same experiment on the nanoparticle substrate and tracking the peak position. A similar procedure was used to assemble the polyelectrolyte layers on the gold nanoparticles, except the PAH /PSS solutions were injected into the PDMS flow cell using syringes and the peak shift tracked in real time. Rinsing was done via purging the flow cell with the salt solution.

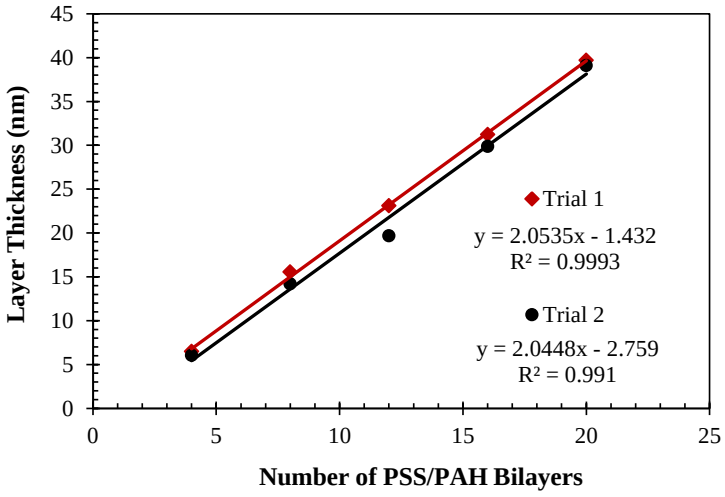

Figure 32. Characterization of thickness of PSS/PAH multilayers on planar gold substrates using ellipsometry. Linear regression was used to fit the data.

Appendix B

MATLAB Code for LSPR Sensor DAQ

```
%Program to calculate spectral data:
clc; clear; fclose('all');

foldername = 'June 24 2011';
PeakDensity = 3;
OutputFileName = 'June 24 HSP70_2.csv';
interval = 1;
infiniteIndex = 1;
counter = 1;
lastpoint = 2;
iLSPR_point = 665;
low = 350;
high = 800;
average_window = 50; %the number of data points over which to average
outputFile = fopen(OutputFileName, 'a');
statistics{1,1} = 'Signal';
statistics{1,2} = 'Sample';
statistics{1,3} = 'Sample ID';
statistics{1,4} = 'Setup';
statistics{1,5} = 'Description';
statistics{1,6} = 'Interval';
statistics{1,7} = 'Position';
statistics{1,8} = 'Height';
statistics{1,9} = 'Width';
statistics{1,10} = 'Quality Factor';
statistics{1,11} = ['Height at ' num2str(iLSPR_point)];
statistics{1,12} = 'Averaged Position';
fprintf(outputFile, '%s,%s,%s,%s,%s,%s,%s,%s,%s,%s,%s,%s\n',statistics{1,:});
%{
for row = 2:counter
    fprintf(outputFile,
'%s,%s,%s,%s,%s,%s,%d,%d,%d,%d,%d\n',statistics{row,:});
end
%}
while infiniteIndex == 1
    pause(interval);
    %Prepare folder info and extract file names
    filestruct = dir(foldername);
    numFiles = size(filestruct);
    for ii = 3:numFiles(1)
        [one numChar] = size(filestruct(ii).name);
        file(ii-2)    =    textscan(filestruct(ii).name,    '%s',    numChar,
'delimiter', sprintf('-'));
    end
    for index = 2:numFiles(1)-2
        counter = counter + 1;
        filename = file{index-1};
        %Get Trial info from filename:
```

```
        temp = textscan(filename{1}, '%s %s %s %s %s %s', 'delimiter',
sprintf('_'));
        for ii = 1:6
            statistics(counter,ii) = temp{ii};
        end

        %Get useable matrix file from data:
        data = fopen([foldername '/' filename{1}]);
        holder = textscan(data, '%f %f');
        [y x] = size(holder{1});
        matrix = zeros(y,2);
        matrix(:,1) = holder{1};
        matrix(:,2) = holder{2};
        %cleanup (delete used files)
        fclose(data);
        if index<numFiles(1)-4
            delete([foldername '/' filename{1}]);
        end
        %crop the function to include only 350 - 800 nm wavelengths:
        ii = 1;
        while matrix (ii,1)<low
            ii = ii+1;
        end
        begin = ii;
        ii = y;
        while matrix (ii,1)>high
            ii = ii-1;
        end
        fin = ii;
        while matrix (ii,1)>iLSPR_point
            ii = ii-1;
        end
        iLSPR = matrix(ii,2);

        %Determine appropriate parameters for the findpeaks function;
        % The 4 adjustable parameters are:
        % SlopeThreshold - Slope of the smoothed third-derivative that is
taken
        %    to indicate a peak. Larger values will neglect small features.
        % AmpThreshold - Any peaks with height less than AmpThreshold are
ignored.
        % SmoothWidth - Width of smooth functions applied to data before
slope is
        %       measured. Larger values will neglect small features. A
reasonable value is
        %    about equal to 1/2 the width of the peaks.
        % FitWidth - The number of points around the "top part" of the
(unsmoothed)
        %    peak that are taken to determine the peak height, positions, and
width.
        %    A reasonable value is about equal to 1/2 the width of the peaks.

        %based on ipeak.m function - determine parameters based on peak
density:
```

```
        % Calculate values of peak detection parameters
        % arguments based on the peak density, PeakD
        % Estimate approximate number of points in a peak half-width
        if strcmp( statistics(counter,1) , 'T')
            X = matrix(begin:fin,1);
            Y = -matrix(begin:fin,2)+max( matrix(begin:fin,2) );
            Y = Y-min(Y);
        else
            X = matrix(begin:fin,1);
            Y = matrix(begin:fin,2);
            Y = Y-min(Y);
        end
        WidthPoints=length(Y)/PeakDensity;
        SlopeThreshold=WidthPoints^-2;
        AmpThreshold=abs(min(Y)+0.02*(max(Y)-min(Y)));
        SmoothWidth=round(WidthPoints/3);
        FitWidth=round(WidthPoints/3);
        % Find the peaks
        P=findpeaks(X,Y,SlopeThreshold,AmpThreshold,SmoothWidth,FitWidth);
        Q = P(:,2)./P(:,4);
        DataTable(counter, 1:7) = [P(end,:) Q(end,:) iLSPR P(end, 2)];
        % average the peak position:
        if counter>average_window+2
            DataTable(counter,       7)       =       mean(DataTable(counter-
average_window:counter, 2));
        end
    end
    time = 1:counter-1;
    time = time*interval;
    plot(time, DataTable(2:end,7));
    %Combine data and statistics into one structure:
    %Write the data to file
    if lastpoint ~= counter
        outputFile = fopen(OutputFileName, 'a');
    for row = lastpoint:counter
        for col = 7:12
            statistics{row,col} = DataTable(row,col-5);
        end
    end

    for row = lastpoint+1:counter
        fprintf(outputFile,
'%s,%s,%s,%s,%s,%s,%d,%d,%d,%d,%d,%d\n',statistics{row,:});
    end
    fclose(outputFile);
    end
    lastpoint = counter;
    counter = counter-3;
end
```

Appendix C

PDMS Flow Cell Fabrication Procedure

PDMS flow cells were molded from CNC machined aluminum templates. To prepare the PDMS, 10ml of Sylgard 184 silicon elastomer base (Dow Corning) was combined with 1ml of Sylgard 184 silicon elastomer (Dow Corning) curing agent in a plastic cup. The solution was mixed until it was full of bubbles and uniform, then placed in a vacuum degasser for approximately 30 minutes or until all of the bubbles had been removed. A hot plate was set to 90°C, and 1/16'' PEEK tubing was inserted horizontally into the holes drilled in the aluminum mold as place holders. Using a syringe, the PDMS solution was carefully injected into the aluminum mold until it was filled completely. The mold was then placed on the hot plate to cure for 5 minutes. After curing, the mold was placed into a cup of water to cool. Tweezers were used to slowly and carefully remove the PEEK tubing from the mold. A scalpel was used to trace around the outer edge of the mold to release the flow cell from the mold. The flow cell was cleaned with acetone and isopropanol (IPA) and inspected under a microscope for any damage.

Appendix D
UV-Ozone Cleaning Protocol and Analysis

Sensor Chip Cleaning Procedure

A procedure using UV-ozone cleaning and rigorous solvent washing was developed in order to regenerate the nanoparticle samples in a non-destructive manner. Gloves were worn throughout the process to prevent contamination. The NP sensor chip was first rinsed with ultrapure H_2O, acetone, and isopropanol (IPA), each for 1 minute, and then dried with an N_2 gun. Note – wet samples should never be put into the UV-ozone cleaner. Next, the chip was placed in the center of the UV-ozone cleaner. The stage height was set so that the chip was ~1cm from the lamp. The UV-ozone cleaner was run for 10 minutes, followed by 5 minutes of ozone elimination with the lamp off and the elimination pump on. The chip was then removed and rinsed with ultrapure H_2O for 2 minutes, followed by 30 seconds of acetone rinsing. Then, the chip was placed into a clean 100ml beaker filled with 20ml of acetone, and allowed to incubate for 10 minutes. Afterwards, the chip was rinsed with acetone for 1 minute, ethanol for 2 minutes, and IPA for 30 seconds. Then, the chip was placed into 20ml of IPA in a 100ml beaker and allowed to incubate for 10 minutes. After, the chip was rinsed in IPA for 1 minute and dried with an N_2 gun. The chip was then placed back into the UV-ozone cleaner. The cleaner was run for 10 minutes, followed by 5 minutes of ozone elimination. The chip was removed and rinsed in ultrapure H_2O for 2 minutes followed by acetone for 1 minute, ethanol for 2 minutes, and IPA for 1 minute. The chip was dried with an N_2 gun and placed in a chip container. The container was back filled with N_2 and placed into a plastic bag, which was also filled with N_2, sealed, and placed in an N_2 desiccator until ready for use.

XPS Analysis of Cleaning Protocol

In order to evaluate whether the UV-ozone cleaning protocol was successful at removing the biofunctional layers, x-ray photoelectron spectroscopy (XPS) was used. Glass substrates coated with 5nm of gold and 2nm of Ti for adhesion (Platypus Technologies) were used as the substrates. Note that nanoparticle chips could not be used since the substrates need to be conductive for XPS analysis. The standard functionalization protocol was used to attach anti-HSP70 to the surface of the gold through the use of a mixed SAM of 11-MUA/1-OT and EDC/NHS. Two identical samples were produced with a layer of bound anti-HSP70. After functionalizing the samples, one sample was cleaned using the UV-ozone cleaning procedure ("AB coated and cleaned") while the other was stored in nitrogen ("AB coated"). A third substrate was prepared fresh by cleaning with the UV-Ozone procedure – this sample

served as the reference as it was never coated with antibody ("Pristine"). All three samples were analyzed in an XPS instrument, located in WatLabs (University of Waterloo), for oxygen (1s), carbon (1s), and nitrogen (1s). The resulting peaks are shown below in Figure 33. The peaks were analyzed using CasaXPS software to determine the area under each peak. This data is summarized in Figure 34. For the AB coated sample, large peaks were seen for oxygen, nitrogen, and carbon, indicating that a large concentration of anti-HSP70 was present on the surface. The AB coated sample that was subsequently cleaned with the UV-ozone procedure showed similar peak areas to the pristine sample, both of which had significantly lower amounts of carbon, nitrogen, and oxygen present on the surface compared to the AB coated sample. This indicates that the UV-ozone cleaning process is able to regenerate the gold surface by removing all of the organic layers of 11-MUA/1-OT and anti-HSP70. The presence of some oxygen and carbon on the cleaned surfaces is expected, since these impurities will quickly adsorb from the air to a clean surface. The lack of any nitrogen peak in the clean samples is strongly indicative that the capture layer was completely removed, as nitrogen is not a typical surface contaminant and would only be present if there was anti-HSP70 remaining on the surface.

The use of this cleaning protocol on the NP samples also proved to be excellent at removing all components of the capture layer from the surface. This was evident as the peak position regularly returned to its nominal position after the cleaning process. The sensors could be regenerated and reused over 50 times without significant damage.

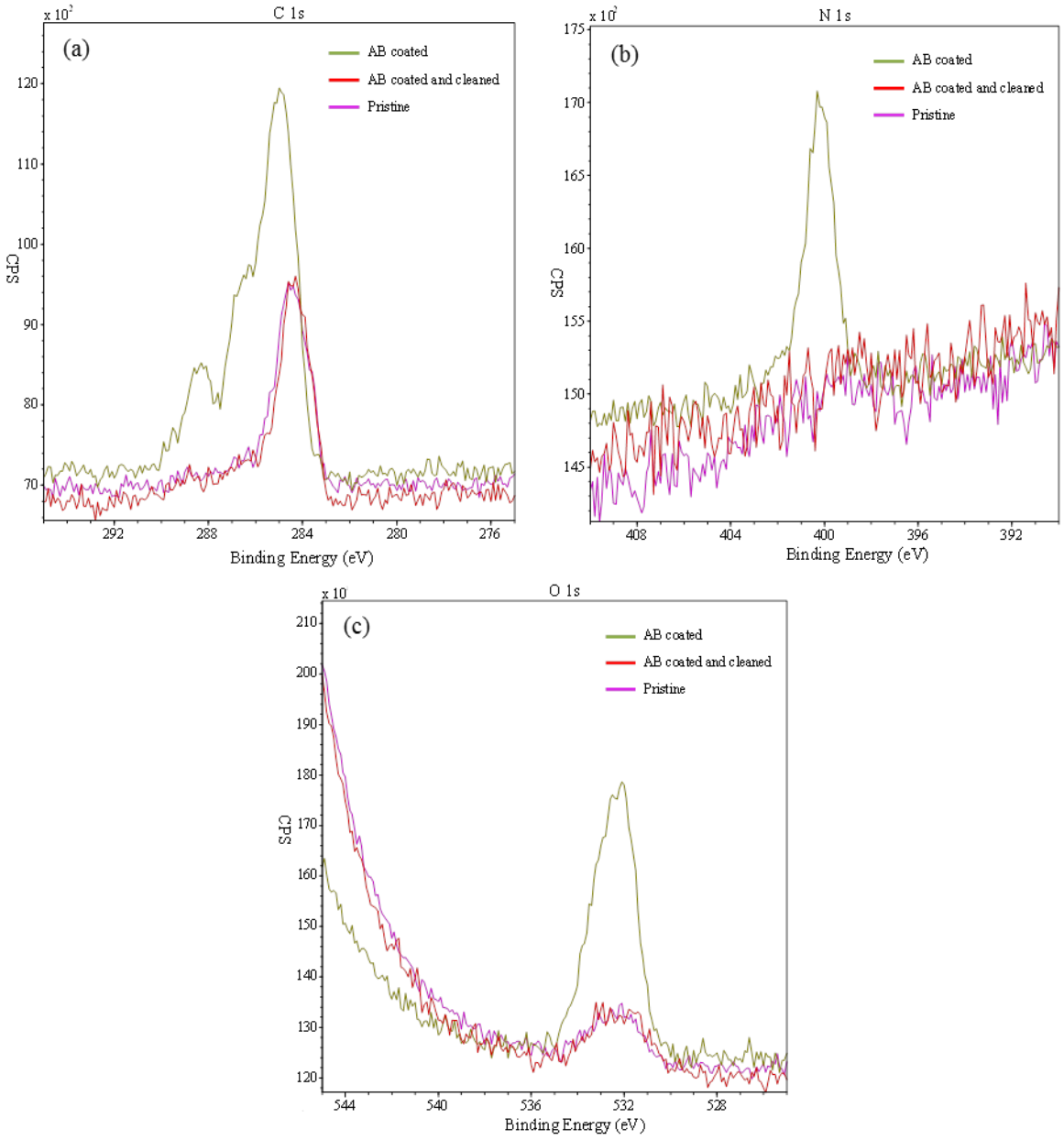

Figure 33. Results from XPS analysis showing the (a) C 1s, (b) N 1s, and (c) O 1s peaks for the three gold substrate samples. The large peak seen in the C, N, and O for the AB coated sample indicates the presence of antibodies on the gold surface. The AB coated sample that was subsequently cleaned with the UV-ozone process shows similar peak intensities as the pristine sample, indicating all of the AB and the SAMs were removed in the cleaning process.

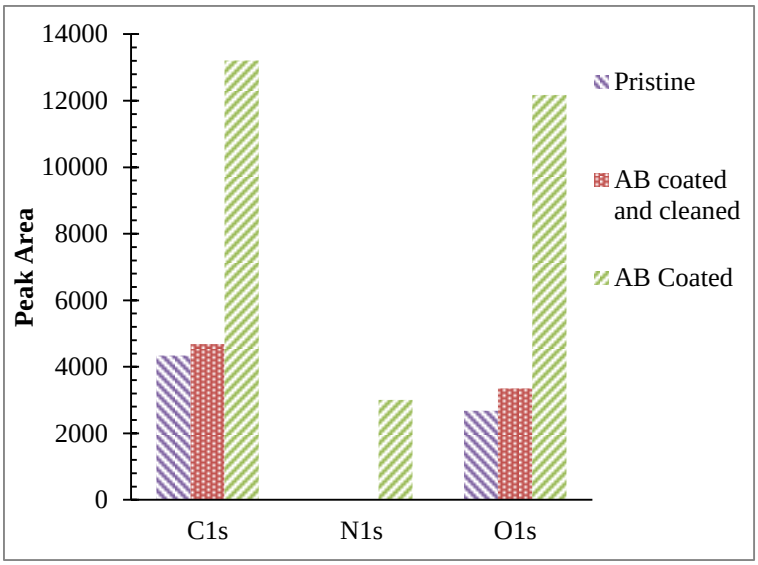

Figure 34. Summary of the area under each XPS peak for C, N, and O for each of the three samples investigated.